NATIONAL & INTERNATIONAL SCIENTIFIC EVENTS

8th International Conference on Engineering Mathematics and Physics Venue: Ningbo University Hotel Location: Ningbo, China Begins: July 1, 2019 Ends: July 3, 2019	8th International Symposium on Delivery of Functionality in Complex Food Systems Venue: Sheraton Porto Hotel Conference Centre Location: Porto, Portugal Begins: July 7, 2019 Ends: July 10, 2019
22nd International Conference on General Relativity and Gravitation Venue: Valencia Conference Centre Location: Valencia, Spain Begins: July 7, 2019 Ends: July 12, 2019	47th IUPAC World Chemistry Congress Venue: Palais des Congrès Paris Location: Paris, France Begins: July 7, 2019 Ends: July 12, 2019
10th Triennial Congress of the International Society for Theoretical Chemical Physics Venue: Clarion Hotel The Edge Location: Tromsø, Norway Begins: July 11, 2019 Ends: July 17, 2019	10th International Conference on Nanotechnology: Fundamentals and Applications (ICNFA'19) Venue: Will be announced. Location: Lisbon, Portugal Begins: August 18, 2019 Ends: August 20, 2019
10th International Conference on Mechanical and Aerospace Engineering Venue: Novotel Brussels City Centre Location: Brussels, Belgium Begins: July 22, 2019 Ends: July 25, 2019	6th Drug Discovery & Therapy World Congress 2019 Venue: Sheraton Boston Hotel, Boston, MA Location: Boston, USA Begins: September 3, 2019 Ends: September 5 2019
3rd World Congress on Electroporation and Pulsed Electric Fields Venue: Pierre Baudin Congress Centre (Centre de Congrès) Location: Toulouse, France Begins: September 3, 2019 Ends: September 6, 2019	30th IEEE International Symposium on Personal, Indoor and Mobile Radio Communication Venue: Istanbul Congress Center (ICC) Location: Istanbul, Turkey Begins: September 8, 2019 Ends: September 11, 2019
11th International Conference on Chemical, Biological and Environmental Engineering Venue: Computer Science School, Campus de Montegancedo, University of Madrid (UPM) Location: Madrid, Spain Begins: September 10, 2019 Ends: September 12, 2019	11th International Conference on Environmental Science and Development Venue: K+K Hotel Location: Barcelona, Spain Begins: February 10, 2020 Ends: February 12, 2020

Abstracted & Indexed in:

TR Dizin Mühendislik ve Temel Bilimler Veri Tabanı | CrossRef | Google Scholar | MIP Database | StuartxChange | ResearchBib | Scientific Indexing Services (SIS)

HITTITE

HJSE Official Journal of Hitit University Volume 6, Issue 2, 2019 www.hjse.hitit.edu.tr

ISSN 2148-4171

HİTİT UNIVERSITY

JOURNAL OF SCIENCE & ENGINEERING

HITTITE

HJSE Official Journal of Hitit University Volume 6, Issue 2, 2019 www.hjse.hitit.edu.tr

Volume 6, Issue 2, 2019

www.hjse.hitit.edu.tr

CONTENT

JOURNAL OF SCIENCE & ENGINEERING
HITTITE

Sample	$T_{f,on}$ (°C)	$T_{f,e}$ (°C)
Olive oil	-35.67±1.12	-40.14±0.15
0%	-35.09±0.09	-38.14±0.03
1% MD	-34.72±0.29	-38.40±0.01
1% WPI	-34.94±0.14	-38.20±0.01
1% MD+WPI	-34.73±0.36	-38.33±0.03
16% MD	-34.96±0.16	-38.78±0.05
16% WPI	-33.34±0.16	-38.77±0.02
16% MD+WPI	-34.30±0.06	-38.67±0.02

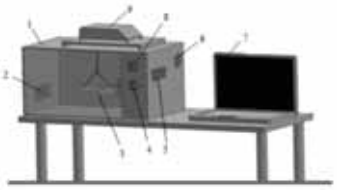

JOURNAL OF SCIENCE & ENGINEERING
HITTITE

CONTENT

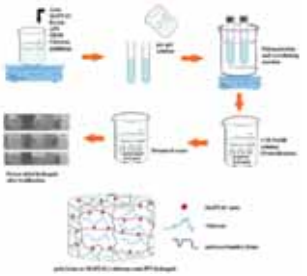

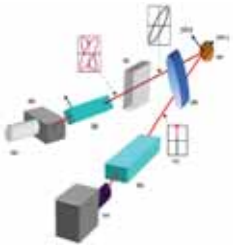

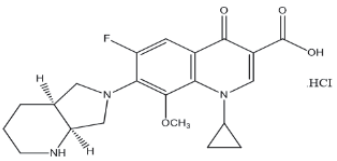

Editor's Office
Tel: +90 364 227 45 33 / 12 36
Fax: +90 364 227 45 35
Email: alikilicarslan@hitit.edu.tr

Subscription Service:
Tel: +90 364 227 45 33 / 12 82
Fax: +90 364 227 45 35
Email: hjse@hitit.edu.tr

EDITORIAL BOARD

Journal Name	: HITTITE JOURNAL OF SCIENCE AND ENGINEERING
Year	: 2019
Managing Editor	: Prof. Dr. Ali KILIÇARSLAN
Managing Office	: Hitit University Faculty of Engineering
Managing Office Tel	: +90 364 227 45 33 / 12 36
Publication Language	: English
Publication Type	: Peer Reviewed, Open Access, International Journal
Delivery Format	: 4 times a year (quarterly)
Print ISSN	: 2149-2123
Online ISSN	: 2148-4171
Publisher Address	: Hitit Üniversitesi Kuzey Kampüsü Çevre Yolu Bulvarı 19030 Çorum / TÜRKİYE
Publisher Tel	: +90 364 227 45 33/1236

This new issue of Hittite Journal of Science and Engineering contains ten manuscripts from the disciplines of biology, chemistry, physics, biomedical engineering, food engineering, materials science and engineering, mechanical engineering, mining engineering. These manuscripts was first screened by Section Editors using plagiarism prevention software and then reviewed and corrected according to the reviewer's comments. I would like to express my gratitude to all our authors and contributing reviewers of this issue.

I would like to thank to the new President of Hitit University, Prof. Dr. Ali Osman Öztürk, for his support and interest in HJSE and also to the Associate Editors of HJSE, namely Prof. Dr. Dursun Ali Kose and Asst. Prof. Dr. Oncu Akyildiz, as well as our Production Editors Assoc. Prof. Dr. Kazim Kose, Mustafa Reşit Haboğlu, Erhan Çetin, Harun Emre Kıran and Ömer Faruk Tozlu for their invaluable efforts in making of the journal.

It's my pleasure to invite the researchers and scientists from all branches of science and engineering to join us by sending their best papers for publication in Hittite Journal of Science and Engineering.

Prof. Dr. Ali Kilicarslan

Editor-in-Chief

Hittite Journal of Science and Engineering, 2019, 6 (2) 83-90
83-90 ISSN NUMBER: 2148-4171
DOI: 10.17350/HJSE19030000132

Production and Mechanical Properties of Bronz/ Steel Chips Composite Materials Produced by Direct Recycling

Hakan Burak Karadag[1], Ahmet Akdemir[2]
[1]Necmettin Erbakan University, Department of Metallurgy and Materials Engineering, Konya,Turkey
[2]Necmettin Erbakan University, Faculty of Aeronautical and Space Sciences, Konya,Turkey

ABSTRACT

In this study, a novel method for the direct conversion of bronze (CuSn10) and steel (S355JR) chips into finished products without melting is introduced. CuSn10 bronze and S355JR steel chips were used as the constituents for the composite materials. The chips were first pressed at room temperature and were subsequently subjected to liquid phase sintering. The composite materials were produced in three different constituent fractions. After production, the composite materials were subjected to compression, three point bending and surface hardness tests in accordance with ASTM standards to compare the results with those for bulk CuSn10 bronze. The produced composite materials have reasonable mechanical properties compared to bulk CuSn10 bronze. Additionally, the results indicate that the proposed method may be considered as an alternative to conventional production methods, such as melting and extrusion.

Article History:
Received: 2018/01/11
Accepted: 2018/10/30
Online: 2019/06/30

Correspondence to: Hakan Burak KARADAĞ,
Konya N. E. University, Faculty of Engineering and Architecture, Department of Metallurgy and Materials Engineering
Phone: +90 5334398535
E-mail: hbkaradag@konya.edu.tr
Address: Ahmet Keleşoğlu kampüsü A2 blok no:232 Meram/Konya/TURKEY

Keywords:
Metal chip recycling; Sintering; Metal matrix composites; Mechanical properties

INTRODUCTION

Metallic chips formed during machining are generally recycled by melting and casting. This procedure results in oxidation of the materials and degradation of the material properties. Additionally, the aforementioned procedure requires high energy consumption and the emission of harmful gases. Additionally, these processes are inefficient and expensive (Gronostajski et al, 1997). It has been reported (Lazzaro and Vittori, 1992) that the process of melting aluminum alloy chips results in 10% burning and 10% slag formation. Additionally, the direct conversion of aluminum chips into compact metal results in 40% material savings, 26–31% energy savings and 16–60% labor savings (Chmura and Gronostajski, 2006).

Solid state recycling is an effective and energy efficient process due to the prevention of oxidation compared with melting processes. Solid state recycling was first proposed by Nakanishi et al. (1995) for recycling magnesium alloy chips and scrap. Lee et al. (1995) and Liu et al. (2002) also conducted research on AZ91D and AZ80 magnesium alloys using solid state recycling. In another study, Nakanishi et al. (1998) investigated solid state recycling for a ZK60 magnesium alloy.

It has been reported that steel, copper, aluminum alloy chips and cast iron can be recycled and converted into composite materials by cold pressing and sintering (Gronostajski, et al., 2000).

Gronostajski et al. (1997) presented a new method for chip recycling. Their method consisted of the conversion of the chips directly (without any intervening metallurgical processes) into a finished product and has been applied to the production of conventional and composite materials. They described and discussed the sintering criteria required for chip recycling. Finally, the application of this recycling method for the production of bearing materials was precisely described. Gronostajski ve Matuszak (1999) investigated a new method for recycling aluminium and aluminium-alloy chips resulting from the machining of semi-finished products, which are very difficult to recycle using conventional methods. This method consists of converting the chips

directly (without any melting processes) into a finished product. By using a powder metallurgy technique followed by an extrusion process, this method was used for the production of composite materials, which are characterized by their superior properties. This new method is environmentally friendly and saves material, labor and energy.

Upadhyaya and Sethi (2007) investigated the effect of different heating and homogenization processes on mechanical behavior of sintered CuSn10 alloy. Fogagnolo et al. (2003) studied the recycling of aluminum chips by cold pressing at room temperature followed by hot extrusion. They reported that the mechanical propertes of hot pressed material are better than that of cold pressed and sintered materials.

Gronostajski et al. (2000) described a method for the direct convertion of aluminum alloy chips into final products. The chips were comminuted in a cutting device, and the granulated chips were used for future processing. The prepared chips were pre-pressed and hot extruded into the final products. The produced material was observed to have the high density and superior properties normally obtained at high extrusion temperatures, which allows the plastic flow of the matrix into pores and voids at relatively low extrusion rates, which permits enough time for diffusional matter transport. Gronostajski et al. (2001) investigated aluminum chip composites and used FeCr powder as a reinforcing phase. The FeCr reinforced material exhibited very good mechanical properties at both room and elevated temperatures. Gronostajski J. and Gronostajski Z. (2003) studied direct recycling, which utilizes cold press molding and hot extrusion. For aluminum alloys, they used Cu, Mg and W materials. As a result of their experiments, they determined that aluminum and its alloys can be recycled through a direct conversion method, which is characterized by low energy-consumption and large material savings. Chmura et al. (2006) studied recycling aluminum and aluminum–bronze chips generated in the fabrication of bearings. Bearing composites were produced by cold compaction and hot extrusion. Mechanical and tribological properties were determined for the end product composite bearing samples. It was found that an aluminum base with an aluminum-bronze reinforcing phase exhibited better frictional properties. Hu et al. (2008) studied the direct recycling of an AZ91D magnesium alloy without melting. This included investigating the effect of chip size upon the microstructure and mechanical properties, which showed that as the surface area of the chip increased, the oxidation increased linearly. Chmura and Gronostajski (2006) studied manufacturing and the properties of bearing materials produced by the recycling of aluminum and aluminum-bronze chips. In this study, bearing composites were produced by cold compaction and hot extrusion of comminuted and mixed aluminum and aluminum-bronze chips. The wear and the coefficients of friction for the composites were determined as a function of the percentage of the reinforcing phase (for the aluminium-bronze granulated chips).

The literature survey revealed that the production of metal matrix composites from steel/bronze chips has not yet been examined. In this study, steel and bronze chips were converted into metal matrix composites by cold pressing and sintering. The proposed method enabled the authors to alter the mass fractions of the constituents and the desired porosity at a very low cost compared to the classical melting/casting procedure. The produced metal matrix composites (MMC) can be used for self-lubricating journal bearings due to their satisfactory mechanical properties and porosity, which results in a high oil storage capacity. This type of material can also be used as a filter or bumper. Currently, the aforementioned parts are produced by powder metallurgy (PM). However, the proposed procedure can be considered as an economic alternative to PM.

In this study, steel and bronze chips were used to produce MMC by direct recycling. Three diffrenet mass fractions were used for the constituents. The mechanical properties of the produced MMC were determined by compression, three point bending and surface hardness tests, and the results were compared with those obtained for bulk bronze.

MATERIALS AND METHODS

In this study, S355JR steel chips and CuSn10 bronze chips were cold pressed at ambient temperature and subjected to liquid phase sintering. The chemical compositions of the materials are presented in Table 1.

Both materials are initially in the form of circular saw chips. The reason these chips were selected is that the cutting process results in the formation of similarly shaped chips.

The saw chips are suitable for plastic deformation during pressing due to material's ductile nature. This situation enables us to obtain the desired prosity at relatively low pressures. The plastic deformation also results in mechanical interlocking between the chips (German, 2007).

The metal chips were first sieved using an 800 μm mesh. Afterwards, the chips were cleaned with acetone (C_3H_6O) to remove any remaining cutting fluid debris.

Table 2 shows the relative compositions of the produced MMC materials. Three different compositions were selected and weighed with a precision scale. Afterwards, the constituents were cold pressed at the environmental tempe-

Table 1. Chemical composition of the MMC constituents (wt. %)

Material										
S355JR	C	Si	Mn	$P_{(max)}$	$S_{(max)}$	N		Fe		
	0.24	0.55	1.6	0.04	0.04	0.009		Balance		
CuSn10	Cu	Sn	Pb	Ni	Fe	Zn	Si	P	Mn	
	87.95	10.45	0.36	0.67	0.025	0.45	0.053	0.012	0.026	

rature. Generally PM products have porosity as high as 35 vol.% (German, 2007). In this study, an open porosity value of as 17 vol.% was chosen. The pressing pressure was determined by preliminary testing to obtain the desired porosity. The selected porosity was maintained for all MMC's.

Table 2. The relative compositions of the MMCs and types

Name	CuSn10 chips (w. %)	S355JR chips (w. %)
b70s30	70	30
b60s40	60	40
b50s50	50	50

To reduce the friction between the die and constituents, 1.5 wt. % graphite particles were added. Afterwards, the constituents were blended in conical blender for 15 mins to obtain a homogenous mixture.

Two different dies were used: a prismatic die with dimensions of 19x19x75 mm and a cylindrical die with a 15 mm diameter and a 45 mm height. The preliminary tests revealed that the prismatic shaped specimens required a pressure of 490 MPa and the cylinderical specimens required a pressure of 1070 MPa. Fig. 1 shows the prismatic and cylindrical test specimens.

Figure 1. Cold pressed specimens: (a) prismatic and (b) cylinderical

After cold pressing, the specimens possess a degree of structural integrity due to the mechanical interlocking processes (German, 2007). The specimens were then sintered in an atmospheric-controlled oven to a temperature of 925°C over 45 min in an Argon environment. The specimens were held at this temperature for one hour. After the sintering, the specimens were slowly cooled down to ambient temperature inside the oven.

At this temperature, the type of sintering that occurs is liquid phase sintering. Therefore, the bronze chips partially melt and envelop the steel chips, which have a higher melting temperature, to create a strong matrix to bind the constituents together.

After production, the specimens were machined by milling or turning to achieve the specified dimensions required for testing.

The specimens were subjected to compression testing at room temperature in accordance with the ASTM (E9-89a) standard, which stipulate a 2 mm/min crosshead speed and specimens with a 13 mm diameter and 39 mm height. The compression tests were repeated three times for consistency and force-displacement curves were obtained for all the tested specimens. These data were utilized to obtain true stress and strain values from formulas 1 and 2:

$$\sigma_{true} = \frac{4Fh'}{\pi d_0^2 h_0} \quad (1)$$

$$\varepsilon_{true} = \ln \frac{h_0}{h'} \quad (2)$$

where h_0, d_0, F and h represent the initial height, initial diameter, applied force and instantaneous height, respectively.

The three point bending tests were done in accordance with the ASTM (E290-97a) standard, which stipulates a 55 mm span width, a diameter of support of 8 mm and a 3 mm/min crosshead speed. The tests were repeated three times for consistency.

One result was that the compressive force can cause the chips to change their orientation (see Fig. 2). The presence of these chips can result in material anisotropy. Therefore, the bending force was applied on both the surface where the compressive force was applied during production and on the side surface. The three point bending tests were continued until fracture and the strength was calculated using the maximum force.

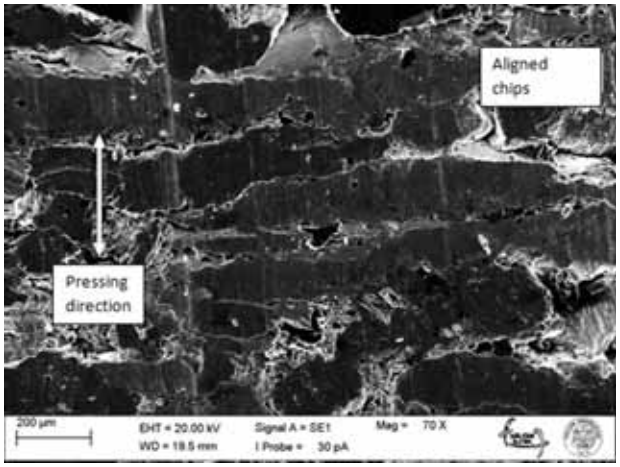

Figure 2. Chip orientation resulting from the effect of the pressing force

After production, the hardness of the composite materials was measured using a Brinell steel sphere with diameter of 5 mm and an indention force of 250 kgf. This diameter was selected because it permits a homogeneous determination of the hardness that examines the constituents and the pores.

RESULTS AND DISCUSSION

Determination of the density and open porosity

The density and open porosity of the produced MMC specimens were determined by gas pycnometer named "Micromeritics AccuPyc II 1340". The densities of the specimens are shown in Table 3. The volume, and thus the densities were measured both before and after sintering. The density of powder metal parts is known to increase after sintering (German, 2007). However, in this study, the density of the MMC was found to have decreased after sintering.

The metallic chips lose the most of their ductility due to the plastic deformation that occurs during machining operations. This situation makes plastic deformation during pressing more difficult. However, the geometry of the chips leads them to behave more elastically. The aforementioned explanations lead us to conclude that the chips behave as an elastic spring and the chips deform elastically during cold pressing. Therefore, when the material heats up during sintering, the elastically deformed chips relax and spring back. This situation results in a volume increase, which results in a decrease in the density. Another reason for the volume increase are the chemical interactions between the constituents, which contain copper and iron (German, 2007). The deformation during sintering supports this idea. The change in volume results in a change in the porosity of the MMC. The open porosity values after pressing and after sintering are shown in Table 4 and increased by approximately 47% after sintering. Generally, densification takes place after sintering. However, due to the shapes and residual stress states of the metallic chips, a spring back effect leads to an increase in the open porosity. Therefore, we can conclude that the oil storage capacity of the specimens has increased.

Table 3. Densities of MMC's before and after sintering

Specimen	*After Pressing (g/cm3)*	*After Sintering (g/cm3)*
b70s30	*6.51*	*6.09*
b60s40	*6.50*	*6.05*
b50s50	*6.50*	*6.05*
Bulk CuSn10	*8.7*	

Table 4. Open porosity percentages of the prismatic and cylinderical specimens

Type		*After Pressing (%)*	*After Sintering (%)*
Prismatic	*b70s30*	*16.9*	*24.9*
	b60s40	*16.9*	*25.0*
	b50s50	*17.0*	*25.1*
Cylindrical	*b70s30*	*16.8*	*24.8*
	b60s40	*16.8*	*24.8*
	b50s50	*17.0*	*24.9*

Compression Testing

The true stress-true strain responses obtained from the compression testing for the MMC and the bulk CuSn10 are seen in Fig. 3. The initial stages of the stress-strain response for all the materials are linear. However, all the material exhibit ductile characteristics. The overall response of the CuSn10 can be assumed to be bi-linear. However, the other materials exhibit non-linearity after the start of plastic deformation.

The numerical results are summarized in Table 5. Both the yield and ultimate strengths of the MMC are lower than the bulk CuSn10 material. However, the higher strength values obtained for the b70s30 material are comparable to the bulk CuSn10. During production, the bronze constituent partially melts and envelops the steel chips, creating a bronze network which results in load transfer between the

chips (German, 2007). As the bronze content decreases, the load transfer between the chips decreases. However, there are stress concentrations around the partially covered steel chips. Therefore, as the bronze content decreases, the strength values decrease. The partially covered chips are examined in detail in later chapters. Table 5 shows that the moduli of elasticity for the MMC exhibit similar behavior. It can be concluded that the decrease in bronze content increases the effect of the pores on the elastic behavior of the MMC between the chips and results in a decrease in the elastic moduli. It can also be concluded that the elastic behavior of the MMC are generally controlled by the bronze content and the steel chips do not affect the elastic moduli.

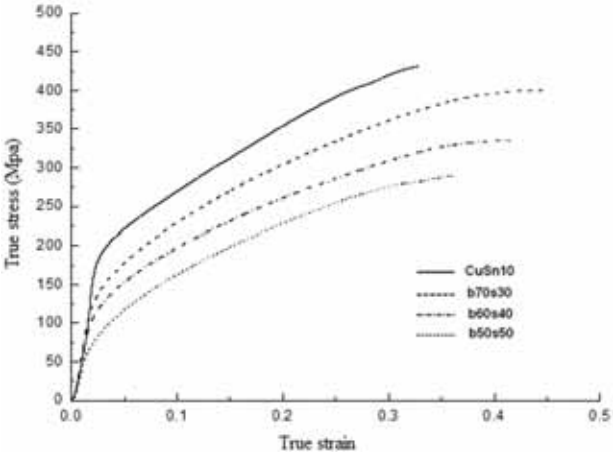

Figure 3. True stress-true strain behavior for the MMC and the bulk CuSn10 under compressive loading

Table 5. Mechanical properties of the MMC materials under compressive loading

	Elasticity Modulus (GPa)	*Yield point (‰,2 offset) (MPa)*	*Ultimate strength (MPa)*
b70s30	*70,78*	*152,0*	*397,90*
b60s40	*53,64*	*132,3*	*335,10*
b50s50	*39,33*	*90,0*	*289,02*
CuSn10	*90,74*	*178,66*	*431,32*

Fig. 4 shows the strain percentage after fracture for the composite materials and bulk CuSn10 during compression testing. The composite materials exhibit significantly more plastic deformation and exhibit more ductility than the bulk CuSn10. This behavior can be associated with the porous nature of the MMC because the pores within the materials can close and see large plastic deformation when subjected to compressive loading. The most ductile behavior is exhibited by the b70s30. As the bronze content decreases, the MMC materials become less ductile. However, the bulk CuSn10 material exhibited the least ductility. Therefore, we can conclude that the MMC material exhibit two different plastic deformation mechanisms: plastic deformation within the bronze constituents and that associated with the closure of the pores.

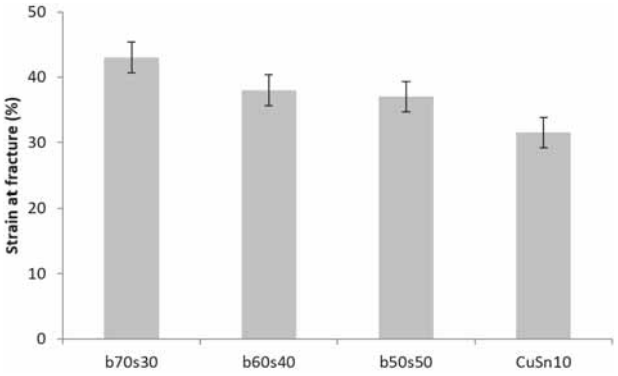

Figure 4. Strain percentage after fracture for the composite materials and the bulk CuSn10 under compressive loading

In order for a material to have a high toughness, it should have both high strength and ductility. The toughnesses of the MMC material are shown in Fig. 5. As stated, the b70s30 material and the bulk CuSn10 exhibit similar strengths. However, the MMC material exhibited more ductility due to its porous nature. The highest toughness is obtained for the b70s30 materials. As the bronze content decreases, the toughness decreases. However, all MMC materials exhibited higher toughnesses than the bulk CuSn10. Therefore, we can conclude that bronze constituent is very important to ensure the material's structural integrity.

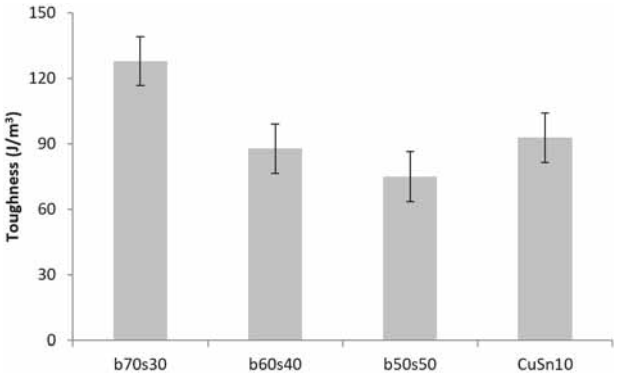

Figure 5. Toughness of the MMC materials

Fig. 6 shows the fracture morphologies of the MMC materials and the bulk CuSn10. The compression tests revealed that the materials experienced ductile deformation. As seen in Fig. 6, the compressive load resulted in shear stress on the plane oriented 45° from the loading direction. No notable barreling is observed. This situation shows that the damage is localized over the 45° plane and that the pores have not completely closed. Additionally, this type of fracture shows that the pores distribute approximately homogenously over the specimens. However, the distribution of the pores is not perfect and a small amount of bending takes place after the compression test.

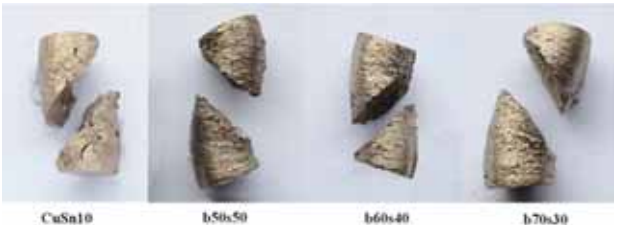

Figure 6. Fracture morphologies of the MMC materials

Three Points Bending Test

The tests were performed in accordance with the ASTM-E290-97a standard, which stipules dimensions of 13x13x70 mm. During the manufacturing process, the metallic chips change their orientation, which can lead to anisotropy in the mechanical properties. To obtain the mechanical properties, the 3PB testing was been repeated for the lateral direction (Fig. 7). The 3PB test results are shown in Table 6. The bending strength of the MMC materials was observed to be lower than that of the bulk CuSn10. As stated, the pores within the structure can result in decreases in the overall strength.

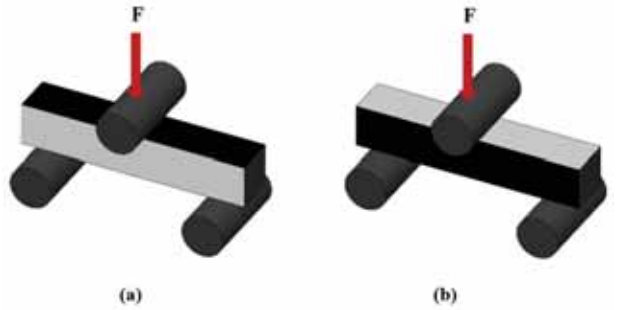

Figure 7. 3PB test application surfaces (a) dark colored area-the upper surface which subjected to force during the pressing process (b) grey colored area-lateral surface

As seen in Table 6, the bending strengths are lower than the compression strengths. We can therefore conclude that the pores in MMC material are more effective under bending. As in the compression test, the highest bending strength was obtained for the b70s30 material. However, bending strength of the b70s30 is lower than the bulk CuSn10.

We can conclude that the pores increase the deformation under compressive loads and restrict the deformation under bending loads, which causes the material to behave in a less ductile fashion. This is mainly due to the creation of tensile stress over the pores and steel chips, which have been partially enveloped by the bronze matrix.

Based on the bending strengths measured in different directions, we observe that the MMC material has anisotropic properties. The strength values obtained from the tests applied on the pressed surface (Fig. 7-a) are higher than the values obtained from the lateral surfaces. During production, compressive loading is applied over the metallic chips placed in the die. As a result, the metallic chips mechanically interlock and are partially cold welded. However, in the transverse direction, interlocking and cold welding occurs as a result of the transverse force that arises between the metallic chips and the die walls.

Table 6. Three point bending test results

Test applied surface	*Configuration*	*Bending Strength (MPa)*	*Max.Disp. at Fracture (mm)*	*Max.force (kN)*
Pressing surface	*b70s30*	*276.8*	*0.99*	*8.13*
	b60s40	*243*	*0.76*	*7.12*
	b50s50	*215.5*	*0.63*	*6.34*
Lateral surface	*b70s30*	*271*	*0.76*	*7.90*
	b60s40	*227*	*0.70*	*6.71*
	b50s50	*171.5*	*0.61*	*5.23*
	CuSn10	*310.7*	*1.92*	*9.11*

Micro Structure and Fracture Morphologies

The microstructure and orientation of the constituents and the integrity between the chips were investigated microscopically. Figs. 8-9 shows the microstructure of the b50s50 and the b70s30 materials after three points bending testing, respectively. We can see from this figure that the constituents were satisfactorily unified. Additionally, the bronze chips have partially melted during sintering, covered the steel chips and partially filled the voids between the chips. However, some larger voids were not completely filled by the bronze. As the bronze content decreased, the steel chips were not fully covered by the bronze.

Figs. 8-9 show that crack initiation takes place at pores and the crack propagates along steel/bronze interface and/or pores. There is no interphase formation between the metallic chips.

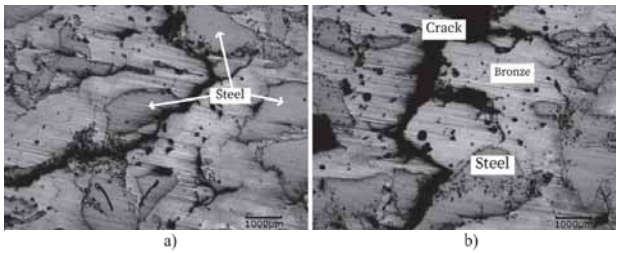

Figure 8. Microstructure of the b50s50 material (50X)

Fig. 10 shows the crack formation and propagation in the bending specimens. The crack started at the mid-point of the specimen where the maximum tensile stress occurs and then propagated towards the upper side. The crack initiated from the stress concentration present around a pore. The cracks propagated in a zig-zag manner in the bulk CuSn10 and MMC materials. From a fracture mechanics

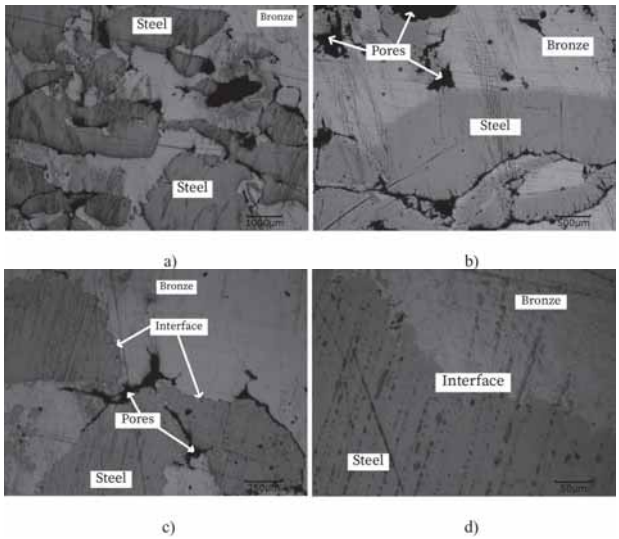

Figure 9. Microstructure of the b70s30: a) 50X, b) 100X, c) 200X and d) 1000X

perspective, the global load equilibrium requires this type of propagation. However, the crack propagation in the MMC materials followed steel/bronze interface and/or pores.

Fig. 10 shows that the bulk CuSn10 exhibited significantly more deformation than the MMC materials when subjected three point bend loading. As the steel content of the MMC materials increased, the material exhibited a more brittle nature. The bending load is a superposition of tensile and compressive loading. The pores result in stress concentrations and the three dimensional stress state masks the ductility. As a result, crack formation takes place.

The CuSn10 constituent is more ductile than the steel constituent. Therefore, we can conclude that as the amount of the CuSn10 constituent decreases, the MMC material becomes less ductile.

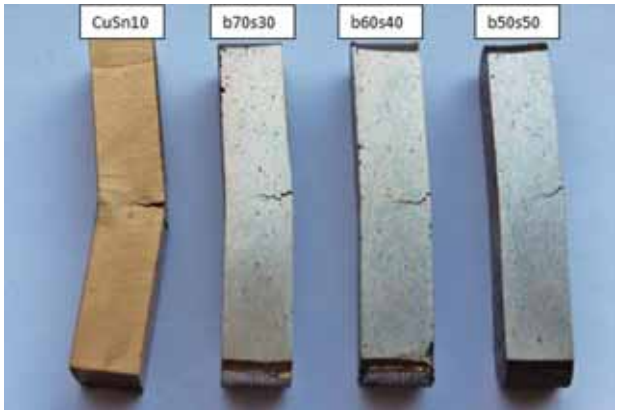

Figure 10. Crack formation in the bending specimens

Surface Hardness Measurement

The metallic chips used for production have an average size of 2 mm. Therefore, to obtain reliable surface hardness measurements, the response of the material must be examined over a relatively large area. For this purpose, a Brinell hardness test was utilized with a 5 mm steel ball indenter. In this manner, the effects of local inhomogeneities on surface hardness measurements are eliminated.

The average Brinell hardness test results are presented in Table 7. The highest hardnesses were obtained for the bulk CuSn10. This is explained by its bulk nature, which contains no pores and perfect structural integrity. As for the MMC materials, the b70s30 material exhibited the highest hardness. This result is consistent with both the compression and 3PB test results. Additionally, it is noted that the hardnesses of the MMC materials are similar. Therefore, we can conclude that the hardness is greatly affected by porosity.

Table 7. Average Brinell hardness test results

	CuSn10	*b70s30*	*b60s40*	*b50s50*
Brinell Hardness	*87*	*48*	*42*	*40*

CONCLUSION

In this study, the production and mechanical properties of MMC materials fabricated from recycling steel and bronze chips without melting was investigated. The major conclusions are as follows:

- The production of MMC materials via the recycling of steel and bronze chips is possible.

- MMC materials can be produced with different amounts of porosity by changing the production parameters. Therefore, this type of material can be used as a filter or bumper. The produced MMC materials can absorb a considerable amount of oil, which makes this type of material suitable for use as a self-lubricating journal bearing.

- The mechanical properties depend on the relative fraction of the constituents. As the bronze content increases, the mechanical behavior of the MMC is similar to that of bulk bronze.

- During the sintering, the bronze chips melt and create a strong matrix which binds the constituents together. Therefore, we can conclude that the mechanical properties are primarily controlled by the bronze constituents and the steel chips act as filler.

- The produced MMC composite material b70s30 is more ductile and tougher than the bulk bronze due to its porous nature. For the MMC to be tougher than the bulk bronze, it must include at least 70% bronze content.

References

1. Chmura, W., Gronostajski, Z., 2006, Bearing composites made from aluminium and aluminium bronze chips, Journal of Materials Processing Technology, 178, 188-193
2. Fogagnolo, J.B. Ruiz-Navas, E.M., Simón, M.A. Martinez M.A., 2003, Recycling of aluminium alloy and aluminium matrix composite chips by pressing and hot extrusion, Journal of Materials Processing Technology 143-144, 792-795.
3. German, R.M., 2007. Powder metallurgy & Particulate Materials Processing, Prentice-Hall.
4. Gronostajski, J.Z., Kaczmar, J.W., Marciniak, H. and Matuszak, A., 1997, Direct recycling of aluminium chips into extruded products, Journal of Materials Processing Technology, 64, 149-156.
5. Gronostajski, J., Matuszak, A., 1999, The recycling of metals by plastic deformation: an example of recycling of aluminium and its alloy chips, Journal of Materials Processing Technology, 92-93, 35-41.
6. Gronostajski, J., Marciniak, H., Matuszak, A., 2000, New methods of aluminium and aluminium-alloy chips recycling, Journal of Materials Processing Technology, 106, 34-39.
7. Gronostajski, J., Marciniak, H., Matuszak, A., Samuel, M., 2001, Aluminium-ferro-chromium composites produced by recycling of chips, Journal of Materials Processing Technology, 119, 251-256.
8. Gronostajski, J., Gronostajski, Z., 2003, Sintering criterion in metal working processes, Journal of Materials Processing Technology, 133, 99-102.
9. Hu, M., Ji, Z., Chen, X., Zhang, Z., 2008, Effect of chip size on mechanical property and microstructure of AZ91D magnesium alloy prepared by solid state recycling, Materials Characterization, 59, 385-389.
10. Lazzaro G., Vittori S., Metal and energy saving by direct and continuous extrusion of aluminium scraps, in: Proceedings of the 121st TMS Annual Meeting, San Diego, California, 1992.
11. Lee, D.-M., Lee, J.-S., Lee, C.-H., 1995. The microstructure and mechanical properties of extruded machined chips for AZ91D magnesium alloy. J. Jpn. Inst. Light Met. 45 (7), 391-396 (in Japanese).
12. Liu, Y., Li, Y.-y., Zhang, D.-t., 2002. Microstructure and properties of AZ80 magnesium alloy prepared by hot extrusion from recycled machined chips. Trans. Nonferrous Met. Soc. China 12 (5), 882-885.
13. Nakanishi, M., Mabuchi, M., Kohei, K., 1995.Relationship between extrusion ratio and mechanical properties of extruded machined-chips of AZ91magnesium alloy. J. Jpn. Soc. Powder Metall. 42, 373-377 (in Japanese).
14. Nakanishi, M., Mabuchi, M., Saito, N., 1998. Tensile properties of the ZK60 magnesium alloy produced by hot extrusion of machined chip. J. Mater. Sci. Lett. 17, 2003-2005.
15. Upadhyaya, A., Sethi, G., 2007, Effect of heating mode on the densification and microstructural homogenization response of premixed bronze, Scripta Materialia volume, 56, 469-472

Hittite Journal of Science and Engineering, 2019, 6 (2) 91-98
ISSN NUMBER: 2148-4171
DOI: 10.17350/HJSE19030000133

Effects of Water Soluble Materials on Water-in-oil Primary Food Emulsion Stability

Hulya Cakmak[1,2] Seher Kumcuoglu[2], Sebnem Tavman[2]
[1]Hitit University, Food Engineering, Corum/Turkey
[2]Ege University, Food Engineering, İzmir/Turkey

Article History:
Received: 2018/05/01
Accepted: 2019/06/17
Online: 2019/06/30

Correspondence to: Hulya Cakmak, Hitit University, Food Engineering,19030, Corum, TURKEY
E-Mail: hulyacakmak@hitit.edu.tr
Phone: +90 364 227 45 33
Fax: +90 364 227 45 35

ABSTRACT

Water-in-oil (w/o) primary food emulsions are often used for encapsulation of bioactive food ingredients or preparing multiple emulsions, however there is a lack of study about evaluation of stability of these emulsions by adding food materials in the dispersed phase. In this study, water-in-olive oil emulsions were prepared with using different dispersed phases; maltodextrin (MD), whey protein isolate (WPI) and maltodextrin+whey protein isolate (MD+WPI) mixture (1:1 w/w) solutions were used at different rates to determine the effects of dissolved material on physical, chemical, rheological and thermal properties of the emulsions. The kinetic stability of emulsions were significantly improved with increasing rates of soluble materials ($p<0.05$), however the improvement was much clearer in emulsions with MD and WPI. The electrical conductivity of emulsions gradually decreased with the increasing amounts of soluble materials and the lowest conductivity was observed for the emulsion with 16% MD+WPI. Newtonian flow behaviour was observed for all of the emulsions, and the viscosity decreased with increasing amounts of dissolved material. The freezing and melting profiles of emulsions were found different than pure olive oil. The average freezing peak temperatures as well as the freezing and melting enthalpies of emulsions were higher than olive oil, but there was no clear difference observed depending on the amount or type of dissolved material. Average d43 values were found changing between 0.855-2.793 µm and the lowest polydispersity was obtained when MD+WPI mixtures were used as the dispersed phase at 16% level.

Keywords:
W/O; Stability; Electrical conductivity; Viscosity; Freezing.

INTRODUCTION

Emulsions are member of disperse systems and they are classified into two main groups as water-in-oil (w/o) or oil-in-water (o/w) depending on disperse or continuous phases. One of two immiscible liquids (oil or water) are dispersed as small spherical droplets in the continuous phase by incorporation of a surfactant (emulsifier) which helps to decrease the interfacial tension between these phases [1, 2]. However, the formed emulsion is thermodynamically unstable, and has a heterogeneous structure; therefore understanding stability mechanisms of emulsion is crucial for determining the shelf life stability of emulsion [1]. Forming of stable emulsion with smaller droplet diameter require high energy mixing or incorporating higher amounts of surfactant [3]. Therefore increasing emulsion stability by using new ingredients is gaining attention nowadays.

Emulsion properties can be characterized by using different experimental procedures; such as storage stability tests (accelerated or regular) and instrumental tests (microscopic analysis, electrical conductivity, droplet size measurement, thermal analysis, droplet charge etc.). There are several studies on evaluation of the stability of double emulsions; however there is a lack of knowledge on w/o primary food emulsion stability depending on the soluble protein and polysaccharide ratio found in dispersed phase of the emulsions.

Proteins and polysaccharides are two main food components used for controlling emulsion stability, microstructure and its texture as well [4]. The amphiphilic and surface-active nature of proteins especially milk proteins may improve the stability of emulsion when it is used as a surfactant [5, 6]. Besides, when two

amphiphilic materials such as proteins and stabilizers are used together, they have synergistic effect against the rupture of formed interfacial film [7]. Proteins can form viscoelastic films at the oil-water interface and maintain the electrostatic and steric stability [8]. Viscosity of the dispersed phase with addition of soluble solids may approach to the continuous phase of emulsion and thus phase separation is reduced [9]. It was stated that, increasing polysaccharide ratio generates a high viscosity droplet network and helps to prevent phase separation [4]. Surfactants can interact with the polysaccharides and proteins which will then change conformation or association, while altering their functional properties such as; rheology, appearance and phase separation [1]. Protein and polysaccharide complexes and conjugates are used as stabilizers for encapsulation purposes [10]. The addition of polysaccharides improves elasticity of the emulsion by forming intermolecular complexes between the proteins and polysaccharides [11]. Utilization of protein and polysaccharide complexes or conjugates for improving o/w emulsion stability is extensively studied, however using of polysaccharide alone and together with the protein addition in w/o emulsion is not yet studied in the literature.

The main goal of this study is to evaluate kinetic stability of water-in-olive oil food emulsion by incorporation of whey protein isolate (WPI), maltodextrin (MD) and their 1:1 mixtures (WPI+MD) into the dispersed phase of emulsion. Physical, chemical, rheological and thermal stability of w/o emulsions were discussed thoroughly based on increasing amounts of soluble materials.

MATERIAL AND METHODS

Refined olive oil (average density: 908 kg/m^3, refractive index: 1.47, viscosity: 53.52 mPa.s, surface tension: 32.9 mN/m, electrical conductivity: 13.5 pS/m at 25°C) and polyglycerol polyricinoleate (PGPR) with of HLB 1.5-2.0 was kindly supplied by TARIS Zeytin ve Zeytinyagi Tarim Satis Kooperatifleri Birligi (Izmir) and Elvan Gida San. ve Tic. A.S. (Istanbul), respectively. Whey protein isolate (Hipro Isowhey, Hardline Nutrition, Istanbul) and maltodextrin with dextrose equivalent 5-7 (Paselli™ MD6, Avebe Nisasta Ltd., Izmir) were purchased from local suppliers.

Emulsion Preparation

The emulsions were prepared depending on the formulations given in Table 1, to wit 80% (w/w) oil phase, 20% (w/w) water phase were homogenized with 5% PGPR (of oil basis) regarding the previous study of the authors [12]. The water phase was composed of pure distilled water for control emulsion, while 1-2-4-8-16% (w/w) maltodextrin (MD), whey protein isolate (WPI) or maltodextrin+ whey protein isolate (1:1) mixture (MD+WPI) were incorporated into water phase as given in Table 1. W/o emulsions were homogenised by using rotor-stator homogenizer (IKA, T25 Ultra-turrax, Germany) equipped with a stainless steel 18G dispersing tool. Water phase of emulsions including either MD, WPI or MD+WPI solutions were prepared with tridistilled water and mixed for 1 h with a magnetic stirrer (Stuart CB162, UK) before using as dispersed phase of the w/o emulsion. Depending on the emulsion formulation, the dispersed phase was added into continuous phase (oil+emulsifier) and homogenized at 8000 rpm for 5 min as it was stated in the study of Cakmak et al. [12].

Table 1. Emulsion formulations

Emulsion type	*Oil (g)*	*Water (g)*	*PGPR (g)*	*MD (g)*	*WPI (g)*	*MD+WPI (1:1) (g)*
0%	*24*	*6.00*	*1.5*	*0*	*0*	*0*
1%	*24*	*5.94*	*1.5*	*0.06*	*0.06*	*0.06*
2%	*24*	*5.88*	*1.5*	*0.12*	*0.12*	*0.12*
4%	*24*	*5.76*	*1.5*	*0.24*	*0.24*	*0.24*
8%	*24*	*5.52*	*1.5*	*0.48*	*0.48*	*0.48*
16%	*24*	*5.04*	*1.5*	*0.96*	*0.96*	*0.96*

Determination of Separated Oil Phase and Viscosity of Emulsions

Emulsions kinetic stability was tested with an accelerated shelf-life test procedure as stated in the study of Wardhono [13] and Cakmak et al. [12]. 15 ml aliquots of emulsion in glass test tubes were stored at 54°C for 14 days in a vacuum oven (WiseVen WOV-30, Daihan Scientific Instruments, Korea). The height of separated oil phase in test tubes was measured daily over 14 days and separated oil phase percent (v/v) was calculated according to the following equation;

$$\text{sep. oil } \% = \frac{V_{oil,\,t}}{V_{oil,t0}} \times 100 \quad (1)$$

here $V_{oil,t}$ represents the volume of separated oil at $t=t_1$, and V_{oil},t_0 represents the volume of oil at initial state ($t=0$). Accelerated shelf-life tests were performed as three parallels and two replicates.

Viscosity of emulsions was measured at 25°C with a stress-controlled rheometer (DHR3, TA Instruments, USA) equipped with concentric cylinder (bob diameter: 27.99 mm, cup diameter: 30 mm). 25 ml of emulsion was placed into cup, and was conditioned at 25°C for 1 min, and steady preshear was applied at a shear rate of 15 rad/s (217.76 1/s) for 2 min in order to eliminate prior stresses. The emulsion was equilibrated for another 1 min at 25°C before application of

flow-ramp test, and test was applied between 0.01 to 200 1/s shear rate. Apparent viscosity values (mPa.s) of these emulsions were obtained from the slope of graph of shear rate (1/s) versus shear stress (mPa), since Newtonian flow behaviour was observed for the emulsions (R^2>0.99).

Electrical Conductivity and Surface Tension of the Emulsions

Electrical conductivity of the olive oil and emulsions were measured with a hand held conductivity meter (Stanhope-Seta, JF 1A-HH, Surrey, UK) at 25°C working within the range of 0-2000 pS/m and in accordance with ASTM D2624 standard test method. In addition, electrical conductivity of the dispersed phases was measured with Mettler-Toledo Seven Excellence S700 analytical meter with INlab 731 ISM probe (Schwerzenbach, Switzerland). This probe allows measurement of electrical conductivity within the range of 0.01-1000 mS/cm.

The surface tension of oil or emulsions against air interface was measured at 25°C according to Wilhelmy plate method by using Krüss K20 Easy dyne (Krüss Gmbh, Germany) tensiometer. The measurement was performed in triplicate and average values were reported.

Droplet Diameter and Thermal Analyses of the Emulsions

Droplet diameter distribution of the emulsions were determined by static light scattering method using Mastersizer 2000 (Malvern Instruments, UK) particle analyser equipped with liquid cell (Hydro 2000S) as stated in the study of Tontul and Topuz [14]. Refractive index of olive oil measured with a digital refractometer (RFM 330, Bellingham+Stanley Ltd., Kent, UK) and found as 1.47 and 1.33 for water. The mean droplet diameter was expressed as volume-weighted mean diameter (d_{43}), and surface-weighted mean diameter (d_{32}) given in the below equations;

$$d_{43} = \frac{\sum_{i=1} n_i d_i^4}{\sum_{i=1} n_i d_i^3} \quad (2)$$

$$d_{32} = \frac{\sum_{i=1} n_i d_i^3}{\sum_{i=1} n_i d_i^2} \quad (3)$$

here n_i is the number of droplet and d_i is the droplet diameter. For polydisperse emulsions, d_{43} diameter is indicated to be more sensitive to the presence of large particles (coalescence and/or flocculation) than d_{32}; therefore the average droplets size was discussed based on the d_{43} values [1, 15]. The width of droplet diameter distribution was determined by calculation of span values from the following equation;

$$span = \frac{d_{0.9} - d_{0.1}}{d_{0.5}} \quad (4)$$

In this equation, $d_{0.1}$, $d_{0.5}$ and $d_{0.9}$ are the diameters of 10, 50 and 90% volume percentiles of the droplets smaller or equal to these values.

Thermal properties of the pure olive oil and the emulsions were performed using Q2000 differential scanning calorimeter (DSC Q2000, V24.11, TA Instruments, USA) by using the method stated in the study of Zafimahova-Ratisbonne et al. [16]. 10 mg of sample were weighed into aluminium pan by an electronic balance (Mettler Toledo, MS205DU, Switzerland) with a resolution of ±0.01 mg, and the cover was hermetically sealed. An empty hermetically sealed aluminium pan was used as a reference pan. Nitrogen gas with 99% purity was used as the purge gas at 50 ml/min steady flow rate. Samples were equilibrated at 20°C for 5 min, and cooled to -60°C at the rate of 2.5°C/min. Then the sample held at -60°C for 5 min before heating from -60°C to 20°C at the same flow rate. The thermograms were analysed with TA Universal Analysis software (Version V4.5A, TA Instruments), and freezing and melting enthalpies (ΔH_{fr} and ΔH_m, J/g), onset (T_{on}, °C) and offset (T_{off}, °C) transition temperatures and peak temperatures (T_p, °C) were recorded.

Statistical Analyses

The differences between the results were analysed using SPSS version 20.0. They were compared using analysis of variance (ANOVA) by Duncan's multiple range test with a significance level of 95%.

RESULTS AND DISCUSSION

Properties of Emulsions with MD

The physical, chemical and electrical properties of MD including emulsions are given in Table 2A. The separated oil phase percent decreased with increasing amounts of soluble solids and therefore the kinetic stability of the w/o emulsion was further improved. This could be due to the gradual decrease of volume of water in the emulsion or increase in the viscosity of the water phase. As stated in the study of Cakmak et al. [12], the increase in the dispersed phase fractions (Φ) leads to the coalescence and phase separation. Maltodextrins are not surface-active compounds, and they can improve emulsion stability by viscosity modification, acting as a thickening agent and gelatinization of continuous water phase [17].

Viscosity of the emulsions with MD were statistically in the same group up to 4% ratio (p>0.05), however the viscosity of emulsion decreased in the latter ratios of MD (p<0.05).

Table 2A. Properties of MD including emulsions.

Maltodextrin amount (%, w/w)	Sep. oil % (v/v)	Viscosity (mPa.s)	Electrical conductivity (pS/m)	Surface tension (mN/m)
0	21.46^{d}	113.64^{e}	-	33.3^{a}
1	12.47^{c}	112.54^{d}	1947.7^{e}	33.3^{a}
2	$12.03^{b,c}$	$111.85^{c,d}$	1701.2^{d}	33.3^{a}
4	$10.34^{a,b}$	111.19^{c}	1506.9^{c}	33.2^{a}
8	$10.42^{a,b}$	109.48^{b}	1309.7^{b}	33.3^{a}
16	9.73^{a}	107.68^{a}	1159.6^{a}	33.4^{a}

Table 2B. Properties of WPI including emulsions.

Maltodextrin amount (%, w/w)	Sep. oil % (v/v)	Viscosity (mPa.s)	Electrical conductivity (pS/m)	Surface tension (mN/m)
0	21.46^{d}	113.64^{d}	-	33.3^{a}
1	12.44^{c}	113.19^{d}	1935.9^{e}	33.2^{a}
2	$11.52^{b,c}$	112.74^{d}	1797.3^{d}	33.2^{a}
4	$10.75^{a,b}$	111.60^{c}	1362.3^{c}	33.2^{a}
8	9.61^{a}	109.03^{b}	1132.3^{b}	33.1^{a}
16	9.37^{a}	107.93^{a}	908.4^{a}	33.1^{a}

Table 2C. Properties of MD+WPI including emulsions.

Maltodextrin amount (%, w/w)	Sep. oil % (v/v)	Viscosity (mPa.s)	Electrical conductivity (pS/m)	Surface tension (mN/m)
0	21.46^{b}	113.64^{c}	-	33.3^{a}
1	10.84^{a}	111.58^{b}	1656.7^{e}	33.1^{a}
2	9.49^{a}	111.64^{b}	1597.1^{d}	33.3^{a}
4	9.35^{a}	111.60^{b}	1389.6^{c}	33.2^{a}
8	9.08^{a}	111.61^{b}	1053.2^{b}	33.2^{a}
16	9.03^{a}	107.59^{a}	838.9^{a}	33.2^{a}

[a-e] Different letters in the same column are statistically different ($p<0.05$).

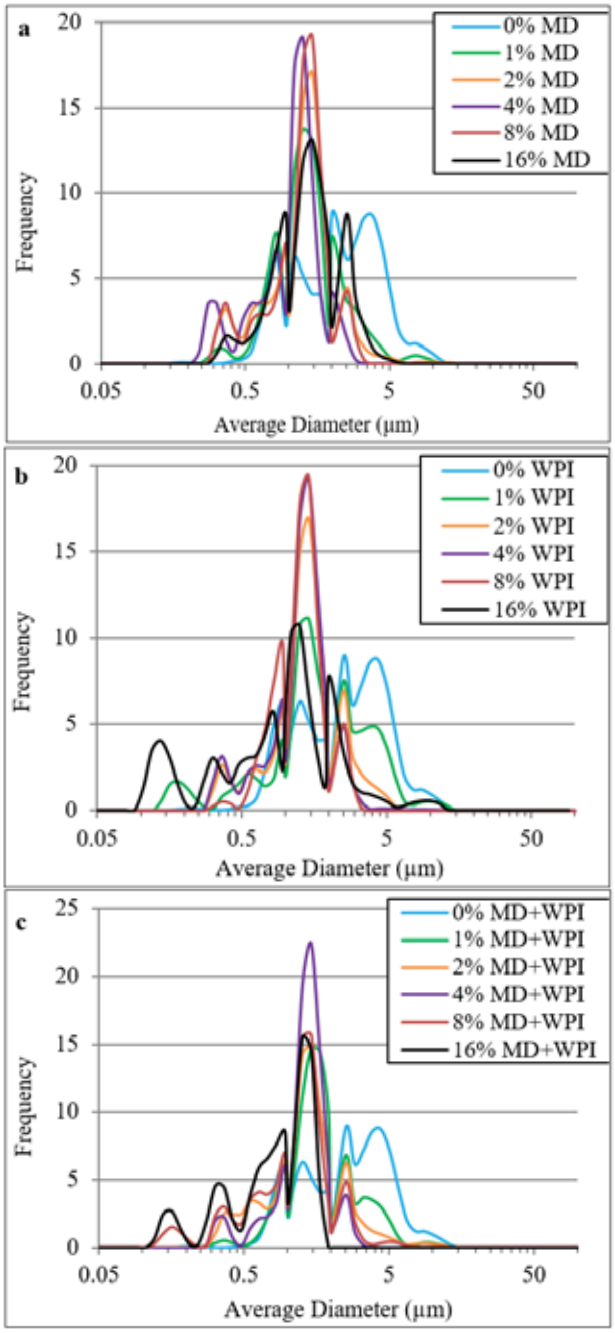

Figure 1. Average particle diameter distribution of emulsion with MD (a); emulsion with WPI (b); emulsion with MD+WPI (c)

Even though the food emulsions are generally known to be having non-Newtonian flow behaviour, the results of the present study are contrary to this knowledge. Similar to this present study, Ushikubo and Cunha [18] have stated that water-in-soybean oil emulsions prepared with PGPR at 70:30 (oil:water) ratio had a Newtonian flow behaviour; however it was stated that at 60:40 ratio emulsions had a shear-thinning behaviour.

The increment in the ratio of MD further increases the dispersed phase viscosity, however the formed emulsions had lower viscosity than the control emulsion (0% MD). Polydisperse emulsions can be packed more efficiently compared to the monodisperse emulsions, so the viscosity of a polydisperse emulsion may be less than the monodisperse emulsions [1]. As shown in Fig. 1A, the studied emulsions had a polydisperse size distribution apart from the MD ratio in the dispersed phase. Depending on the equation derived by Einstein, the viscosity of an emulsion (suspension) is correlated with the viscosity of the continuous phase [1]. However this equation is valid when the continuous phase is Newtonian, dispersed particles are rigid with spherical shape and in case of no particle-particle interaction is observed. For most of the food emulsions, the viscosity of dispersed phase are rather has no importance because of the droplets acts as rigid spheres [1].

The electrical conductivities of the emulsions are found

Table 3A. Average particle diameter and span values of emulsion with MD.

MD amount (%, w/w)	d_{32} (μm)	d_{43} (μm)	span
0	$1.748^{d;C}$	$2.793^{d;D}$	1.757
1	$1.247^{c;B}$	$1.678^{c;C}$	1.487
2	$0.942^{a,b;A}$	$1.294^{b;B}$	1.225
4	$0.900^{a;A}$	$1.175^{a;A}$	1.023
8	$0.932^{a,b;A}$	$1.182^{a;A}$	1.027
16	$0.966^{b;A}$	$1.344^{b;B}$	1.482

Table 3B. Average particle diameter and span values of emulsion with WPI.

MD amount (%, w/w)	d_{32} (μm)	d_{43} (μm)	span
0	$1.748^{c;C}$	$2.793^{e;E}$	1.757
1	$1.023^{b;B}$	$2.037^{d;D}$	2.597
2	$1.070^{b;B}$	$1.440^{c;C}$	1.416
4	$0.988^{b;B}$	$1.272^{a,b;A,B}$	1.072
8	$1.074^{b;B}$	$1.230^{a,b;A}$	0.941
16	$0.423^{a;A}$	$1.344^{b;B,C}$	1.722

Table 3C. Average particle diameter and span values of emulsion with MD+WPI.

MD amount (%, w/w)	d_{32} (μm)	d_{43} (μm)	span
0	$1.748^{e;E}$	$2.793^{f;F}$	1.757
1	$1.354^{d;D}$	$1.831^{e;E}$	1.713
2	$0.988^{c;C}$	$1.450^{d;D}$	1.567
4	$1.028^{c;C}$	$1.265^{c;C}$	0.905
8	$0.748^{b;B}$	$1.153^{b;B}$	1.292
16	$0.574^{a;A}$	$0.855^{a;A}$	1.259

[a-f] Different letters in the same column are statistically different ($p<0.05$).
[A-F] Different letters in the same column are statistically different ($p<0.01$).

to be gradually decreasing with increasing amounts of MD, which directly corresponds to the gradual decrease of volumetric amount of water in the dispersed phase. Phase separation (gravitational) or phase inversion can be determined by measuring electrical conductivity [1, 6, 19]. The sharp decrease in electrical conductivity occurs when the o/w emulsion inverts to w/o emulsion [19]. The electrical conductivity of continuous oil phase was 13.5 pS/m and pure water having of comparably higher electrical conductivity, the emulsion conductivity was therefore closer to the continuous phase. But if there was a phase separation depending on the instability of the emulsion, we could observe that the electrical conductivity of the emulsions might be much higher, even getting closer to the water phase. The dispersed phase conductivity with increasing amount of MD dissolved was increased in spite of the opposite trend was observed for the emulsion conductivity. 16% MD solution had an average electrical conductivity of 34.5±0.0 mS/m.

The surface tension of the emulsion were not statistically different ($p>0.05$) depending on the MD amount dissolved. Moreover, the surface tension of the pure oil (32.9 mN/m) was also similar to these emulsions.

Particle size distribution and average particle diameter values of MD including emulsion are shown in Fig. 1A and Table 3A. Multimodal droplet diameter distribution was observed for all MD including emulsions. However, depending on the increase in the MD amount dissolved, the polydispersity of droplet diameter decreased and narrow diameter distributions with much smaller diameters were observed. The smallest d_{43} values were observed for 4% and 8% MD emulsions, but the smallest span value was observed for 4% MD emulsion. Higher span values are associated with a more polydisperse and therefore a lower stability of the emulsion [20]. If the phase separation values and average droplet diameter values were analysed together, the smallest average diameter were not observed in the lowest phase separated values. Small droplet diameter values are desired for increasing the emulsion stability; however decrease in the droplet size induces Brownian motion which may promote destabilization of emulsion by flocculation mechanism [21].

Properties of Emulsions with WPI

The physical, chemical and electrical properties of emulsions with WPI are given in Table 2B. Separated oil phase of the WPI emulsions were found exponentially decreasing with the amount of WPI dissolved (R^2=0.9767), similar to the viscosity (R^2=0.9429) and electrical conductivity change (R^2=0.9794). Milk proteins and especially whey proteins are often used with surfactants for increasing the emulsion stability by contributing steric stabilization against flocculation and coalescence [9]. Proteins are able to cover the oil droplets as a monolayer during homogenization and thus it lowers the interfacial tension and prevent droplet coalescence in o/w emulsions [22, 23]. The increment in the WPI content resulted in a similar behaviour with the MD including emulsions, so that the lower separated oil phase, viscosity and electrical conductivity was observed in higher dissolved material concentrations. However, the electrical conductivity of 16% WPI emulsion was statistically lower than the 16% MD emulsion ($p<0.05$). This result is contrary to the electrical conductivity of the solutions with MD and WPI. 16% MD solution had an average electrical conductivity of 34.5±0.0 mS/m while 16% WPI emulsion had an average conductivity of 195.2±0.3 mS/m. As stated by McClements [22], surfactants may affect the protein conforma-

tion and the interactions; such as non-ionic surfactants may bind to the protein molecules with hydrophobic interactions. Also the change in molecular characteristics of the globular proteins (such as WPI) may then alter the interfacial properties of the emulsion.

The surface tension of the emulsions with WPI were found again similar to the oil, and there was no change observed depending on the amount of material dissolved ($p>0.05$).

Particle size distribution and average particle diameter values of WPI including emulsion are shown in Fig. 1B and Table 3B. Average particle diameters were in accordance with the separated oil phase amount, however the smallest d_{43} values were observed in the emulsion with 8% WPI. In addition, the particle diameter distribution is shifted towards left, which demonstrates the narrower particle diameter with smaller average diameters were observed depending on the increment in the WPI amount. 16% WPI emulsion had a lot more number of particles smaller than 0.5 μm compared to the other emulsions, and these results in accordance with the surface-weighted mean diameter. Moreover the type of the dissolved material did not have any significant effect on the kinetic stabilities of the emulsions, but on microscopic level differences were revealed by the droplet diameter distributions.

The stability of emulsions with proteins can be further improved with addition of polysaccharides for controlling rheology, and hence the phase separation and gravity induced creaming is delayed [9]. The use of proteins together with the polysaccharides provides some advantages such as; improvement of the physicochemical and storage stability as well as textural and mouthfeel properties [23]. Ercelebi and Ibanoğlu [24] stated that, the creaming instability of the protein stabilized emulsions were decreased by the use of polysaccharides (pectin vs. guar gum), and WPI-guar gum complex produced the more stable emulsions compared to the WPI-pectin complexes.

Properties of Emulsions with MD+WPI Mixture

The kinetic stability of the MD+WPI emulsions were found statistically in the same group ($p>0.05$), which was not in accordance with the general trend observed in MD or WPI emulsions. Protein and polysaccharide conjugates improve the emulsion stability better than protein used alone [5]. But there was no data about the improvement of emulsion stability when protein and polysaccharide is used as a solution instead of conjugate. As shown in Table 2C, the kinetic stability of emulsion with 1:1 mixture of MD+WPI was further improved even at 1% incorporation level. Although the dispersed phase fraction was similar for each dispersed material type (protein, polysaccharide or their mixture), the viscosities of 1-2-4 and 8% MD+WPI were found in the same group as well ($p>0.05$). These findings support our claim that not only conjugates but the solution of maltodextrin with whey protein isolate at 1:1 level may improve the stability of w/o emulsions. Also, the electrical conductivity of the MD+WPI solution were found between the MD and WPI solutions alone, however the conductivity of 16% MD+WPI mixture was statistically lower compared to the 16% MD and 16% WPI emulsions (data not shown). This data also was consistent with the previous findings, and the interfacial tension between water and oil phase of the emulsion with 16% MD+WPI mixture might possibly decreased.

The droplet diameter distributions and the average particle diameters of the MD+WPI emulsions are given in Fig. 1C and Table 3C, respectively. The diameter distribution of the emulsions gets narrower with increasing amount of dissolved material, and there was no particle observed above 2 μm diameter for 16% MD+WPI. The degree of polydispersity was reduced, and even better results were obtained compared to WPI emulsions when the MD+WPI mixtures were used as the dispersed phase at 16% incorporation level. So, MD+WPI solutions at 1:1 level may further be used to improve the stability of w/o emulsions.

Thermal Properties of the Emulsions

DSC analysis provides practical information about the thermodynamic changes occurred during phase transition of edible oils, and these thermodynamic characteristics may help to identify the chemical composition, phase separation (instability of emulsion) as well as identification or detection of the adulteration of these edible oils [25-28]. Thermal properties of the emulsions between freezing and melting processes are shown in Table 4. During freezing, a major exothermic peak around -40°C and a smaller peak around -10°C was observed in the thermograms of pure olive oil and 1% WPI including emulsion (data not shown). Two endothermic peaks, one of them having a much steeper peak around -5°C was observed during melting. For extra virgin olive oil, a minor peak at -13°C and a major peak at -38°C was observed during freezing as it was stated in the study of Chiavaro et al. [26]. Similar to this present study, Calligaris et al. [29] stated that a major peak between -18°C and 0°C with a minor peak between 0-10°C was observed during melting of extra virgin olive oil. These distinct differences in two peaks are related with the chemical composition of the oil; since saturated fatty acids (triacylglycerol) crystallize at higher temperatures and melt at higher temperatures compared to the unsaturated fatty acids [26, 28-30].

Melting and freezing enthalpies of the emulsions were

Table 4. Freezing and melting properties of emulsions.

Sample	$T_{fr,on}$ (°C)	$T_{fr,p}$ (°C)	$T_{fr,off}$ (°C)	ΔH_{fr} (J/g)	$T_{m,on}$ (°C)	$T_{m,p}$ (°C)	$T_{m,off}$ (°C)	ΔH_m (J/g)
Olive oil	-35.67±1.12	-40.14±0.15	-51.22±0.22	34.39±0.40	-19.24±0.04	-4.01±0.05	9.98±0.04	67.91±0.84
0%	-35.09±0.09	-38.14±0.03	-44.52±0.27	63.59±1.11	-15.77±0.09	0.64±0.03	8.99±0.14	106.35±1.35
1% MD	-34.72±0.29	-38.40±0.01	-45.41±0.38	62.75±1.09	-16.61±0.47	0.61±0.08	9.41±0.34	105.20±1.80
1% WPI	-34.94±0.14	-38.20±0.01	-43.81±0.09	64.29±0.10	-16.55±0.24	0.62±0.01	9.54±0.17	109.35±0.05
1% MD+WPI	-34.73±0.36	-38.33±0.03	-44.47±0.29	62.08±0.65	-16.32±0.15	0.62±0.01	9.21±0.07	105.55±1.75
16% MD	-34.96±0.16	-38.78±0.05	-45.10±0.05	53.90±0.07	-14.90±0.16	0.45±0.05	8.98±0.00	91.14±0.18
16% WPI	-33.34±0.16	-38.77±0.02	-43.05±0.05	60.45±0.20	-16.57±0.00	0.34±0.01	9.95±0.11	100.40±0.30
16% MD+WPI	-34.30±0.06	-38.67±0.02	-43.84±0.20	57.06±0.18	-17.05±0.60	0.27±0.00	10.12±0.15	97.76±0.40

significantly higher than the olive oil itself, since water and emulsifier (PGPR) addition to oil contributed to this increase as similarly stated by the literature [16]. However, there is no clear difference in the melting or freezing enthalpies observed depending on the type of material dissolved (either protein or polysaccharide) or the amount of material in the dispersed phase. The droplet diameter also is an important parameter on freezing temperature, such as the emulsion with a smaller mean diameter have a lower freezing temperature [16], however there was no significant difference observed in the freezing temperatures of the emulsions depending on the average droplet diameter in this present study.

CONCLUSION

The physical and chemical stability of the emulsions can be determined with various methods; however the effects of soluble solid type and the amount of soluble materials not yet discussed. In this study, whey protein isolate and maltodextrin were incorporated individually or together into the dispersed water phase of the w/o emulsion and depending on the obtained results; MD+WPI mixtures at 1:1 rate could successfully increase the kinetic, chemical and thermal stability of w/o food emulsions. Especially 16% MD+WPI incorporation level have significantly reduced the average particle diameter (d_{43}). The kinetic stability, and viscosity of MD and WPI incorporated emulsions was in the same group with the MD+WPI emulsion for 16% level, however the electrical conductivity of the emulsion with MD+WPI was significantly lower than both of the emulsion with MD and WPI. Further studies may focus on testing the stability of primary w/o emulsions with respect to homogenization conditions or effect of different protein and polysaccharide sources on emulsion stability may be tested.

ACKNOWLEDGEMENT

This study was funded by The Scientific and Technological Research Council of Turkey (TUBITAK) with the Grant No. 214O405 and by Ege University Science and Technology Project Commission (BAP) with the Grant No. 15-BIL-024. Authors also would like to thank Dr. Ismail Tontul and Prof. Dr. Ayhan Topuz for their help in droplet diameter measurements, Dr. A. Evren Yavuz for his help in surface tension measurement, G. Ela Gurpuz and Neslihan Bozdogan for their help in some of experimental studies. Some parts of this study was presented in the 21st National Thermal Science and Technology Congress (2017) held in Çorum.

References

1. McClements D.J. Food Emulsions: Principles, Practices, and Techniques, 2nd ed., CRC Press, Boca Raton, p. 609, 2005.
2. Pichot R. Stability and Characterisation of Emulsions in the Presence of Colloidal Particles and Surfactants, PhD Thesis, University of Birmingham, UK, p. 204., 2010.
3. Tadros T.F. Emulsion Science and Technology, Wiley-VCH Verlag GmbH & Co. KGaA, Weinheim, p. 344, 2009.
4. Herrera M.L. Analytical Techniques for Studying the Physical Properties of Lipid Emulsions, Springer, New York, p. 61, 2012.
5. Akhtar M., Dickinson E. Whey protein–maltodextrin conjugates as emulsifying agents: an alternative to gum arabic. Food Hydrocolloids 21(4) (2007) 607-616.
6. Tavernier I., Wijaya W., Van der Meeren P., Dewettinck K., Patel A. R. Food-grade particles for emulsion stabilization. Trends in Food Science & Technology 50 (2016) 159-174.
7. Aserin A. Multiple Emulsions: Technology and Applications, John Wiley & Sons Inc., Hoboken, p. 326, 2008.
8. Lam R.S., Nickerson M.T. Food proteins: a review on their emulsifying properties using a structure–function approach. Food Chemistry 141(2) (2013) 975-984.
9. Dickinson E. Interfacial structure and stability of food emulsions as affected by protein–polysaccharide interactions. Soft Matter 4(5) (2008) 932-942.
10. Evans M., Ratcliffe I., Williams, P.A. Emulsion stabilisation using polysaccharide–protein complexes. Current Opinion in Colloid & Interface Science 18(4) (2013) 272-282.
11. Derkach S.R. Rheology of emulsions. Advances in Colloid and Interface Science 151(1-2) (2009) 1-23.
12. Cakmak H., Gurpuz G.E., Bozdogan N., Kumcuoglu S., Tavman S.

Dispersed Phase and Emulsification Conditions on the Stability of Water-in-Oil Emulsion. Food Studies 7(1) (2017) 29-37.
13. Wardhono E.Y. Optimization of Concentrated W/O Emulsions: Stability, Trapping and Release of Polysaccharides, PhD Thesis, Université de Technologie Compiégne, France, p. 168, 2014.
14. Tontul, I., Topuz, A. Mixture design approach in wall material selection and evaluation of ultrasonic emulsification in flaxseed oil microencapsulation. Drying Technology 31(12) (2013) 1362-1373.
15. Komaiko J., Sastrosubroto A., McClements, D.J. Formation of oil-in-water emulsions from natural emulsifiers using spontaneous emulsification: sunflower phospholipids. Journal of Agricultural and Food Chemistry, 63(45) (2015) 10078-10088.
16. Zafimahova-Ratisbonne A., Wardhono E.Y., Lanoisellé J.L., Saleh K., Clausse D. Stability of W/O emulsions encapsulating polysaccharides. Journal of Dispersion Science and Technology 35(1) (2014) 38-47.
17. Silva K.A., Rocha-Leão M.H., Coelho M.A.Z. Evaluation of aging mechanisms of olive oil–lemon juice emulsion through digital image analysis. Journal of Food Engineering, 97(3) (2010) 335-340.
18. Ushikubo F.Y., Cunha R.L. Stability mechanisms of liquid water-in-oil emulsions. Food Hydrocolloids 34 (2014) 145-153.
19. Maali A., Mosavian, M.H. Preparation and application of nanoemulsions in the last decade (2000–2010). Journal of Dispersion Science and Technology 34(1) (2013) 92-105.
20. Eisinaite V., Juraite D., Schroën K., Leskauskaite, D. Preparation of stable food-grade double emulsions with a hybrid premix membrane emulsification system. Food Chemistry 206 (2016) 59-66.
21. Tadros T., Izquierdo P., Esquena J., Solans, C. Formation and stability of nano-emulsions. Advances in Colloid and Interface Science 108 (2004) 303-318.
22. McClements D.J. Protein-stabilized emulsions. Current Opinion in Colloid & Interface Science 9(5) (2004) 305-313.
23. Sun C., Gunasekaran S., Richards, M.P. Effect of xanthan gum on physicochemical properties of whey protein isolate stabilized oil-in-water emulsions. Food Hydrocolloids 21(4) (2007) 555-564.
24. Ercelebi E.A., Ibanoğlu, E. Influence of hydrocolloids on phase separation and emulsion properties of whey protein isolate. Journal of Food Engineering 80(2) (2007) 454-459.
25. Tan C.P., Man, Y.C. Differential scanning calorimetric analysis of edible oils: comparison of thermal properties and chemical composition. Journal of the American Oil Chemists' Society 77(2) (2000) 143-155.
26. Chiavaro E., Vittadini E., Rodriguez-Estrada M.T., Cerretani L., Bendini A. Differential scanning calorimeter application to the detection of refined hazelnut oil in extra virgin olive oil. Food Chemistry 110(1) (2008) 248-256.
27. Fasina O.O., Craig-Schmidt M., Colley Z., Hallman H. Predicting melting characteristics of vegetable oils from fatty acid composition. LWT-Food Science and Technology 41(8) (2008) 1501-1505.
28. Jafari M., Kadivar M., Keramat, J. Detection of adulteration in Iranian olive oils using instrumental (GC, NMR, DSC) methods. Journal of the American Oil Chemists' Society 86(2) (2009) 103-110.
29. Calligaris S., Sovrano S., Manzocco L., Nicoli, M.C. Influence of crystallization on the oxidative stability of extra virgin olive oil. Journal of Agricultural and Food Chemistry 54(2) (2006) 529-535.
30. Barba L., Arrighetti G., Calligaris S. Crystallization and melting properties of extra virgin olive oil studied by synchrotron XRD and DSC. European Journal of Lipid Science and Technology 115(3) (2013) 322-329.

Hittite Journal of Science and Engineering, 2019, 6 (2) 99-107
ISSN NUMBER: 2148-4171
DOI: 10.17350/HJSE19030000134

Methodology on Co-Registration of Mri and Optoelectronic Motion Capture Marker Sets: In-Vivo Wrist Case Study

Senay Mihcin
Katip Çelebi University, Biomedical Engineering, İzmir/Turkey

Article History:
Received: 2018/07/15
Accepted: 2019/02/04
Online: 2019/06/30

Correspondence to: Senay Mihcin, Katip Çelebi University, Biomedical Engineering, İzmir, TURKEY
E-Mail: senaymihcin@ikc.edu.tr
Phone: 0232 329 37 61

ABSTRACT

Skin-surface mounted markers provide incomplete spatial information of the underlying-bone. A new methodology is developed combining optoelectronic motion capture (MOCAP) and imaging modalities to co-register the positions of underlying-bone and external markers. Skin surface-mounted markers, utilized in MR imaging, were coated with reflective material to collect spatial data in passive infra-red optoelectronic MOCAP system. Two-link jig mechanisms were designed to mount-on marker sets; these were rotated in increments through 180° of angular rotation at pre-determined angles. The rotations were recorded within the MOCAP system and 3T MRI scanner under a 3D STIR (short tau-inversion recovery) sequence. A 3D in-silico model was built for the co-registration of marker centroids' on a 1 to 1 scale. Differences were calculated from the co-registered data obtained from these two systems using the same set of markers. Root mean square error (RMSE) and angular rotation was less than 1.5 mm in translation and 1° respectively in-vitro. Concordance Correlation Coefficients (CCC) was calculated as (0.9788 to 1). Mean-Difference plots showed good agreement. Next, adduction/abduction movements of the natural wrist joint were investigated in six healthy subjects. MOCAP data was collected for three sets of motions, and MRI scans were repeated twice to derive within-subject repeatability data. Within-subject, the maximum RMSE for wrist angular rotations was 1.28° and 1.30° respectively in vivo. Pearson correlation coefficient was calculated for adduction and abduction as 0.70 and 0.71 respectively. Paired Student-t test identified systematic differences. The used methodology established the way to analyze the relationship between the bone and external markers.

Keywords:
Joint angle; Optoelectronic motion capture systems; Cross sectional imaging modalities; Image registration; Wrist kinematics.

INTRODUCTION

The measurement of human kinematics is underpinned by the need to isolate and model the movement of bony segments [1]. Advances in the study of human kinematics are challenged however by the difficulty of measuring skeletal movement using surface mounted markers [2]. One of the major confounders in this field is soft tissue movement artefact (STA), caused by differential movement of the skin-mounted markers relative to the underlying bones [3]. Although alternative techniques exist that incorporate direct modelling of the internal structures, such as stereo radiography and single plane fluoroscopy, as well as measurements derived from bone pins or external fixation devices [4,5,6,7], these methods are either invasive or expose the subject to ionizing radiation. Mundermann et al [8] suggested markerless motion capture for lower limbs. Although this would represent a non-invasive and non-constraining method, it also requires drawing of inference for internal structures from surface measurements. Also for very complicated joints such as the spine, the accuracy and relevance remains uncertain and the technique is not at the stage of application for clinical purposes.

For some anatomical regions such as the talus in the hind foot and the spine, the anatomy is either not accessible from the surface or is functionally too complex to relate surface mounted marker outputs to the underlying bony segments reliably. In this study, I explored the feasibility of a combined approach in which the coordinates of reflective coated, surface-mounted-MRI-marker set can be mapped explicitly onto the underl-

ying anatomy using internal imaging, as a first step towards clinical applications for subject specific implant modelling. Andriacchi et al. [9], described briefly a similar methodology for understanding knee kinematics, but the work was aimed at generating animations and no substantive quantitative results were reported. A recent report by Andersen et al [10] investigated the accuracy of a linear STA model in human movement analysis by simultaneously recording bone-mounted pin and skin marker data for the thigh and shank using bi-planar radiographs for walking, cutting and hopping. However, without use of the cortical bone pins, the problem of STA still remains challenging and our study aimed to identify whether a non-invasive solution might be achievable.

The specific aims of the current study were i) to establish a methodology for the proof of concept and to quantify the error associated with the co-registration of the two data sets; as surface marker data in (MOCAP) and surface marker data in (MRI) in vitro model and ii) once proof of concept was established, to determine the error associated with the technique in the natural wrist joint, for co-registration of the surface markers (MOCAP) and (MRI) universes and for the relationship of the surface markers to the underlying segmented bone data (MRI).

MATERIAL AND METHODS

In-Vitro Phase

Twelve surface markers were attached to a purpose built jig mechanism consisting of two links and a revolute joint which was constructed from polyethylene and fixed to a base produced from a polyamide (nylon) composite material (DuraForm, 3D Systems) (Fig. 1). The base of the jig was manufactured using a Vanguard Selective Laser Sintering Rapid Prototyping machine (Sinterstation HIQ Series, 3D Systems, Valencia, CA) and contained a grid of internal calibration channels with a diameter of 6.4 mm filled with saline water for warping investigation of MRI images. The hinge mechanism of the two links was designed to represent a highly constrained planar movement, as a simplified representation of radial-ulnar deviation of wrist joint.

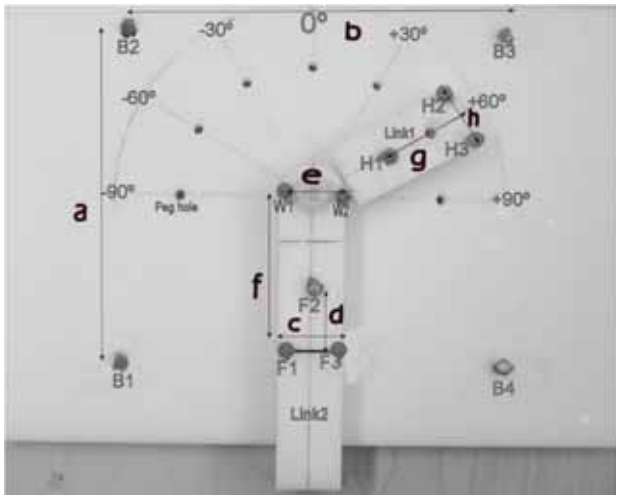

Figure 1. Two-link mechanism with a grid surface base filled with saline water with 6.4 mm diameter holes securely fitted at the ends and at the angle of +60° degrees for Link1
Dimensions of the field of view for MRI

a=160 mm	c=30mm	e=30mm	g=30mm
b=160mm	d=30mm	f=80mm	h=30mm

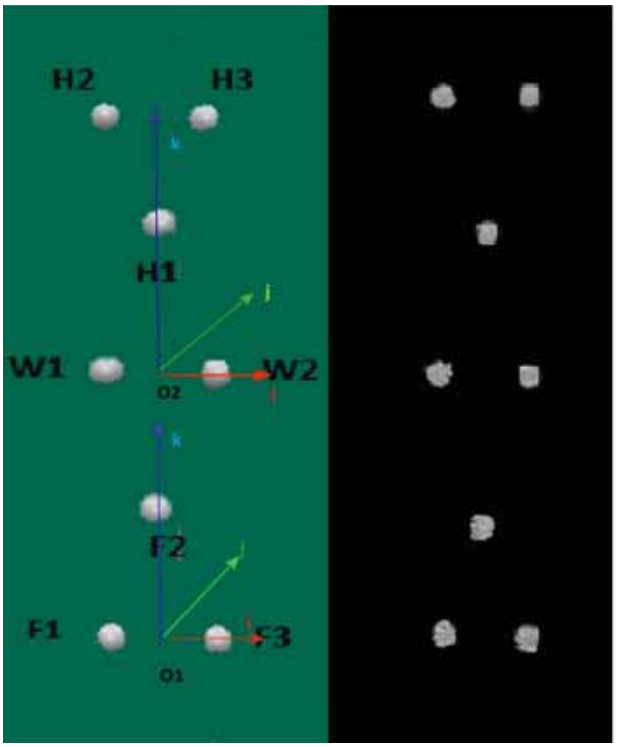

Figure 2. Markers in a) the motion capture system (MOCAP) showing the reference frames on two segments and in b) the MRI system, with Link 1 aligned at 0°in both cases.

The twelve 6mm PinPoint® markers (Beekley Corp., CT, USA) were attached to the jig in the configuration illustrated in Fig. 1. The markers consisted of spherical balls, filled with a proprietary fluid (Radiance ®) which generates high signal on MRI. Prior to use, markers were also coated with retro-reflective material to enable their use with the passive infra-red reflective marker motion capture system. The markers were positioned as follows: four markers (B1, B2, B3, B4) were placed to serve as a local coordinate system for the base, three tracking markers were placed on each of the fixed (F1, F2, F3) and rotating links (H1, H2, H3) and two calibration markers (W1, W2) were placed at each side of the revolute joint representing the wrist (Fig. 2 a and b).

Experimental Protocol in Vitro

Link1 on the jig mechanism (Fig. 1) was adjusted to rotate around the revolute joint through 180° in seven increments, with a peg-and-hole arrangement precision mac-

hined into the jig at 30° intervals to ensure consistency of positioning. Marker data for each position was captured using both a 3D passive marker motion analysis system (Vicon MX, Oxford Metrics, UK) and an MRI scanner (Siemens Magnetom 3 Tesla MRI using 3D voluming), as detailed below.

The MOCAP system used in this study was a part of GAIT laboratory for clinical studies in a hospital which consisted of eight passive-marker cameras (Vicon MX with T40 cameras, Oxford Metrics, UK) capturing at 150 Hz and 2 Mega-pixel resolution. The system is installed for regular patient examination. It is installed and according to the quality management regulations of the hospital. The cameras have 6.5-15.5 mm Varifocal lenses. Technical error for the cameras within a working volume of 10 x 11 x 2.5 m was calculated as less than 0.2 mm for this experimental set-up. The motion analysis data were acquired using Vicon Nexus 13.1 and transferred to Visual3D software (C Motion, Germantown, MD) for initial post processing.

The jig was then transferred to the MRI suite where imaging was performed using a 3T Siemens Magnetom Verio scanner with a 32 channel body coil. The images were acquired using a 3D SPACE sequence (TR=540ms, TE=108ms, 0.85mm isotropic resolution). The grid surface of the test rig was initially assessed for residual warping after a proprietary distortion correction algorithm, built into the scanner's standard software, had been applied. The standard deviation of the measured dimensions from the known dimensions was calculated as 1.01 mm in the X direction and 1.07 mm in the Y direction over the whole field of view (160 mm by 60 mm) after application of the distortion correction algorithm. This algorithms was applied to all subsequent image datasets. The fixed link (Link2) was aligned with the long axis of the MRI coil co-centrically. As with the motion analysis data capture, Link1 was sequentially rotated in constrained 30° increments through the 180° range of motion and the jig was imaged at each increment.

In-Vivo Phase

Participants

The right wrists of six healthy subjects (3male and 3 female, average age of 34 in the range of 31- 45) were investigated in this study. The subjects had no history of wrist injury. Ethical committee permission was obtained from university's ethics committee, and written consent was obtained from all participants prior to their involvement in the study.

Experimental Protocol in Vivo

A revised experimental jig was designed so that the subjects could place their forearms in three constrained positions representing adducted, neutral and abducted positions of the wrist (Fig. 3a). This jig consisted of a resting surface with a peg and a hole mechanism to place the hand in the pre-determined positions. At the wrist and along the forearm, supporting pegs and Velcro bands secured the forearms of the participants for stability.

Optoelectronic motion data was initially gathered from the participants at the gait lab (Fig. 3b) with the markers placed on wrist in the same configuration using the Vicon system as defined previously for the in-vitro phase. Static and dynamic coordinates of the markers derived from the

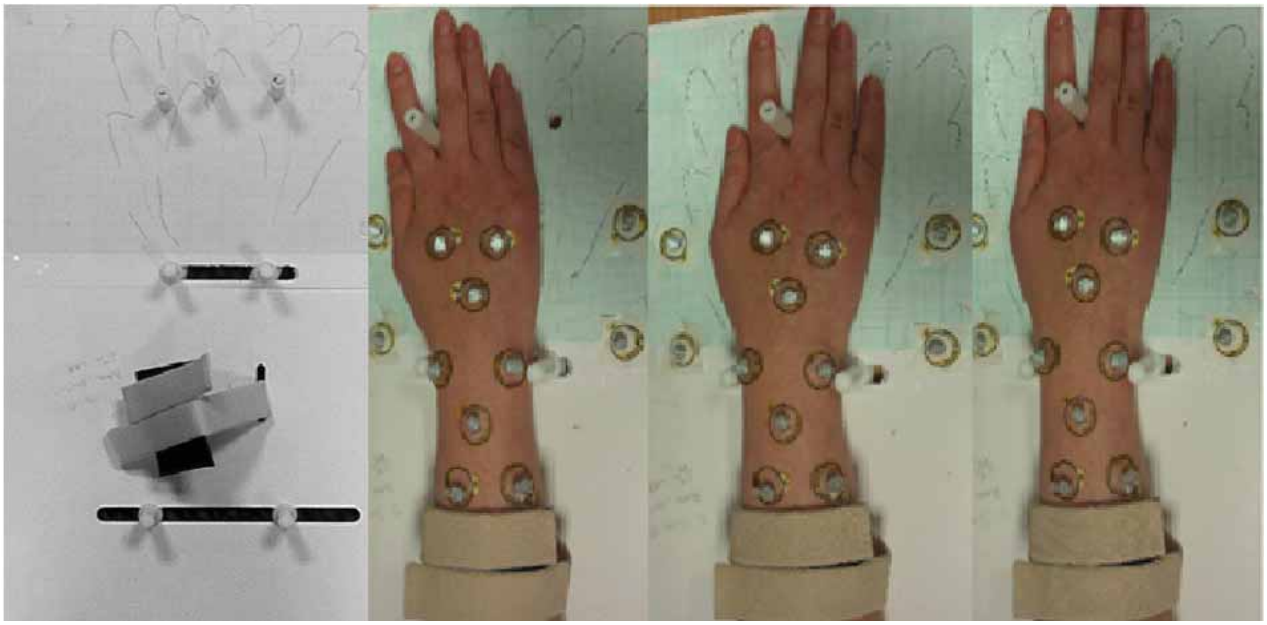

Figure 3. a) The jig used for b) stabilizing the predetermined positions of the hand and forearm marker locations during data collection in vivo.

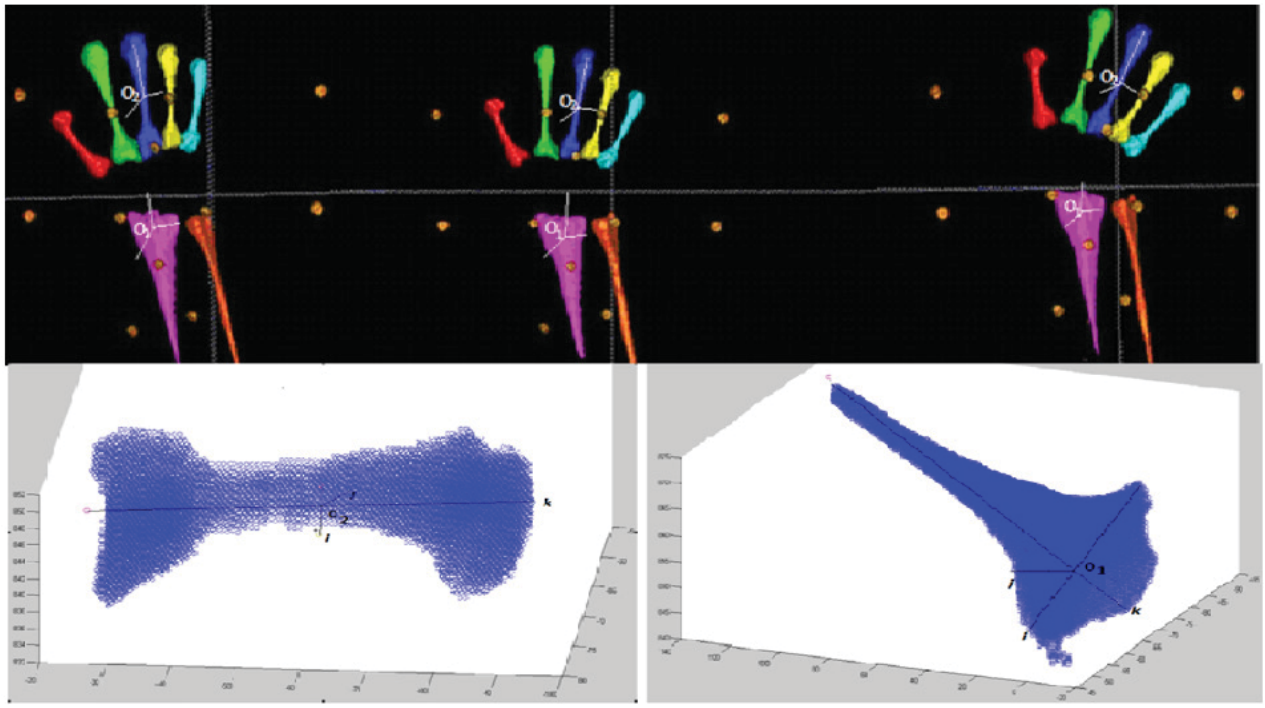

Figure 4. a) Adducted neutral and abducted postures of metacarpal, radius and ulna bones and external markers with coordinate centres shown based on PCA analysis b) Third metacarpal bone and c) radial bone information cloud derived from segmented images for PCA analysis.

MOCAP data outputs were recorded for the three different positions of the wrist.

For repeatability purposes, motion capture acquisition was repeated three times. Subjects were then taken to MRI unit with the markers still in situ and scanned in each of the three positions using the same MRI protocol as described previously. This three-position scan set was then repeated a second time to allow evaluation of reliability.

Post Processing

Image Processing

For the MOCAP data, the surface marker coordinate values were obtained directly from Visual 3D.

For the MRI images, the surface markers were isolated in the 3D image data by binarizing the image at a threshold selected by eye. Each connected component was then labelled and the centroid of each resulting labelled region was located using Snap ITK (Apache 2.0 license, Insight Software Consortium, NY, USA). The image was then registered to an arbitrary default grid using the versor based landmark transform algorithm of ITK (Apache 2.0 license, Insight Software Consortium, NY, USA) using the base markers (B1-4) to enable comparison with the MOCAP dataset.

For the in vivo phase, a manual segmentation process was undertaken to identify the metacarpal and radial bones in the MRI images of each of the six subjects (Fig. 4a). The third metacarpal bone and radial bone were selected to investigate the joint angle between the forearm and the hand. The segmented images of the two bones were converted to point-clouds and a principal component analysis was undertaken in MATLAB in order to consistently compute the origin and orientation of a coordinate system for each bone in each position (Fig. 4b,c). These coordinates were then used to calculate the joint angles of the bone.

Angular Calculations

The relative angles between the two links for the in vitro phase and the two bones for the in vivo phase were calculated using a bespoke code in MATLAB (version R2008a, The MathWorks Inc., USA) based on the coordinate data derived from the surface markers (MOCAP and MRI) and the segmented bones (MRI).

For the in vitro phase, two right handed reference frames, with orthogonal axes i, j and k, were defined on Link1 and Link2 (Fig. 2 a). The i and k directions were defined for each rigid body and the j vector was calculated as their cross-product. For reference frame1 (on the moving link frame Link 2), O_1 was defined as the average of the wrist markers (W1 and W2), the i vector was calculated as a vector from O_2 to W2 and the k vector as a line from O2 to centre of the H2 and H3 markers. For reference frame2 (on the fixed Link 1), O_2 was defined as average of wrist markers (F1 and F3), i was defined as a line from O1 to marker F3 and k as a line from O_2 to O_1 .

It was assumed that this local coordinate system was rigid and did not change during the movement, as the mar-

kers represent the rigid body corresponding to the logic of static measurements in Visual 3D. The i, j, and k directions were calculated for Link 2 as it rotated around Link 1, for the seven orientations at 30° intervals. The joint angle was defined by the relative orientation of one local coordinate system (H1-3) with respect to the other (F1-3) and was independent of the position of the origin of these coordinate systems.

For the in vivo phase, similar convention was used. PCA analysis provided the extreme points on the third metacarpal bone and the radial bone to use as internal bone marker co-ordinate data (Fig. 4). Centre of 3rd metacarpal bone was named as O_2 and centre of radial bone was named as O_1 (Fig. 4b). The k direction was defined as the line connecting the first component of third metacarpal bone O_2 and i direction was defined as the line connecting the second component of PCA to O_2. On radial bone k was defined from the centre of the first component of PCA to O_1 and i was defined as the line from the second component of PCA to O_1 (Fig. 4c).

Joint angles are rarely represented by an orientation matrix, but instead by a parameterized representation of this. A 3-D rotation matrix (in other words the orientation of one local coordinate system with respect to another) is represented by three successive rotations about unique axes. This ensures that three elements (angles) fully specify the nine components of a 3x3 rotation matrix. In this study, the rotation matrix was defined by multiplying the orientation matrix of the jig or wrist in two positions to calculate the joint angle. By elaborating the rotation matrix for the y-x-z sequence, the Cardan angles were extracted and designated α (alpha) for the first rotation, β (beta) for the second rotation, and γ (gamma) for the third rotation [11].

In order to validate the bespoke code written in MATLAB, initial post processing of the surface marker data with Visual 3D (C-Motion Inc, US) using an Y-X-Z Cardan sequence was undertaken to provide an industry standard benchmark. For the in vitro phase, the bespoke MATLAB and Visual 3D algorithms were used to calculate the angular rotation using both the MOCAP and MRI surface marker datasets. For the in vivo phase, to confirm that the code worked in the less constrained non-rigid system of natural wrist, the surface marker data (MRI) were fed back into Visual 3D. Rotational angular values were then calculated by using the Y-X-Z Cardan sequence in both Visual 3D and MATLAB and the outputs were compared.

Analysis

For the in vitro phase, the surface marker data from the MOCAP and MRI systems consisted of X, Y and Z coordinates. However, with a constrained jig, the Z coordinate was assumed to be constant for the surface markers on the two link mechanism. The translational (X, Y) coordinate data for the two modes of acquisition were compared by determining the root mean square (RMS) error for the seven different positions of Link 1. The results for angular rotation about the hinged axis were also compared between the two systems (Fig. 5), because this represents the relevant clinical output.

For the in vivo phase, the following comparisons were made:

a) Surface marker (MOCAP) data versus marker (MRI) data

The surface marker (MOCAP) data were deemed to constitute the best available gold standard for the lab-derived marker coordinates and the resulting angular rotations were calculated using Visual 3D (C-Motion Inc, US). These angles were compared with those derived from the surface marker (MRI) data, calculated using the bespoke MATLAB code to check if the systems were comparable irrespective of the input source data and code used. To determine the repeatability, the RMS error was also calculated for the repeated measurements undertaken using both MOCAP and MRI systems.

b) Surface marker (MRI) data versus segmented bone (MRI) data

The angular rotations calculated by the bespoke MATLAB code for the surface marker (MRI) data and segmented bone (MRI) data were compared. This was to determine the correlation between the bone and the surface markers when both measures were taken using the same (MRI) system.

c) Surface marker (MOCAP) versus segmented bone (MRI) data

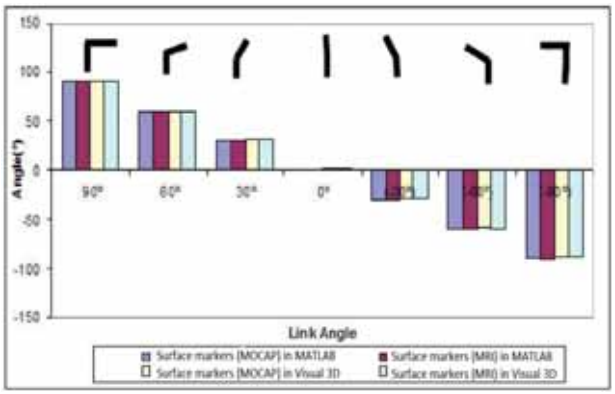

Figure 5. Calculated relative angle of Link1 with respect to Link2 using in-house MATLAB routines and Visual 3D based outputs for both MOCAP and MRI acquired data

Table 1. RMS difference between MRI and MOCAP data in (mm)

	Fixed markers (mm)									Rotating markers (mm)		
	B1	B2	B3	B4	F1	F2	F3	W1	W2	H1	H2	H3
X	0.19	0.15	0.24	0.42	0.29	0.45	0.61	0.23	0.33	0.51	0.69	0.31
Y	0.07	0.44	1.1	0.93	0.41	0.72	0.59	0.82	0.95	1.43	1.42	1.18

The outputs of Visual 3D for the surface markers (MOCAP) were compared with the outputs of the MATLAB code for the segmented bone (MRI) inputs. This was to represent the practical application of the method and determine if systematic errors existed between the two measurements that could be accounted for.

To assess the agreement between the two systems, mean-difference plots, a graphical method introduced by Bland & Altman [12], were derived for the angular values of the two segments relative to each other (Fig. 6). Finally, the concordance correlation coefficient was calculated as described by Lin [13] for angular data, providing a numerical indicator of agreement between the two acquisition protocols.

RESULTS

In Vitro

Marker Coordinates

The markers were analyzed in two sets; the fixed markers (B1 - B4, F1 - F3, W1 and W2) and the rotating markers attached to Link1 (H1 - H3). The maximum RMS errors for all the scan angles were found to be 0.69 mm and 1.43 mm in the X and Y directions respectively for all markers (Table1). The RMS errors were observed to be higher in the Y direction than in X both for fixed and rotating markers.

High levels of agreement were found between the marker positions determined from the MOCAP and MRI systems. Mean-Difference plots were constructed and the Concordance Correlation Coefficient (CCC) values were calculated separately for the X and Y coordinates. The mean of the differences was -0.18 ± 0.59 mm for the X direction and 0.66 mm ± 0.63mm for the Y direction. The CCC varied between 1 and 0.9998 for the fixed markers, and between 0.9999 and 0.9788 for the rotating markers.

Angular Rotations

The difference (RMS error) between the angular values determined from the MOCAP and MRI based data was found to be less than 1 °, with a maximum difference of 0.88° (Table 2). Good agreement was found between the in-house code and the proprietary Visual 3D output (Fig. 6a,b).

Table 2. Angular differences between MOCAP and MRI based data, both calculated using in-house code in MATLAB

Angular Difference between MOCAP and MRI Marker data(Matlab Derived)						
90°	60°	30°	0°	(-30°)	(-60°)	(-90°)
0.07	0.42	0.16	0.11	0.3	0.01	0.88

Mean-difference plots were constructed for angular values for the outputs from the MOCAP and MRI custom MATLAB routines. The RMS error was 0.05° (95% confidence interval= 0.39°) and the CCC for angular agreement between MOCAP and MRI data was 1.000.

In Vivo

The in-vivo data was derived from the mean of the outputs of the bespoke code and the gold-standard Visual 3D for the inputs of surface marker (MRI) data obtained from MRI scans in each position as explained in section 2.2.4 as a first step . To assess the agreement between the two systems, Bland & Altman plots were plotted for the angular values of the two segments relative to each other for abducted and adducted angles (Fig. 6b). Maximum angular difference was less than 1°. This showed that the MATLAB code calculates the angles not much different than the gold standard Visual 3D software for the less constrained system of natural wrist. Surface marker (MOCAP) versus (MRI) angle showed good agreement (Fig. 6b). CCC for adducted and abducted angular values between MATLAB and Visual 3D for the surface marker (MRI) data was 0.92 and 0.96 respectively. CCC was 0.97 and 0.98 for adduction an abduction respectively for the outputs of Visual 3D for the input data of Surface Markers (MOCAP) and outputs of MATLAB code for the surface markers (MRI).

The outputs of Visual 3D for the surface markers (MOCAP) were compared with the outputs of the MATLAB code for the segmented bone (MRI) inputs (Fig. 6c). Maximum RMS values were calculated for Visual 3D and MRI and segmented bone (MRI) data as 1.28°, 1.3°, and 0.98 ° respectively. This was to ensure the comparability of the bespoke code for reporting angular rotations when using

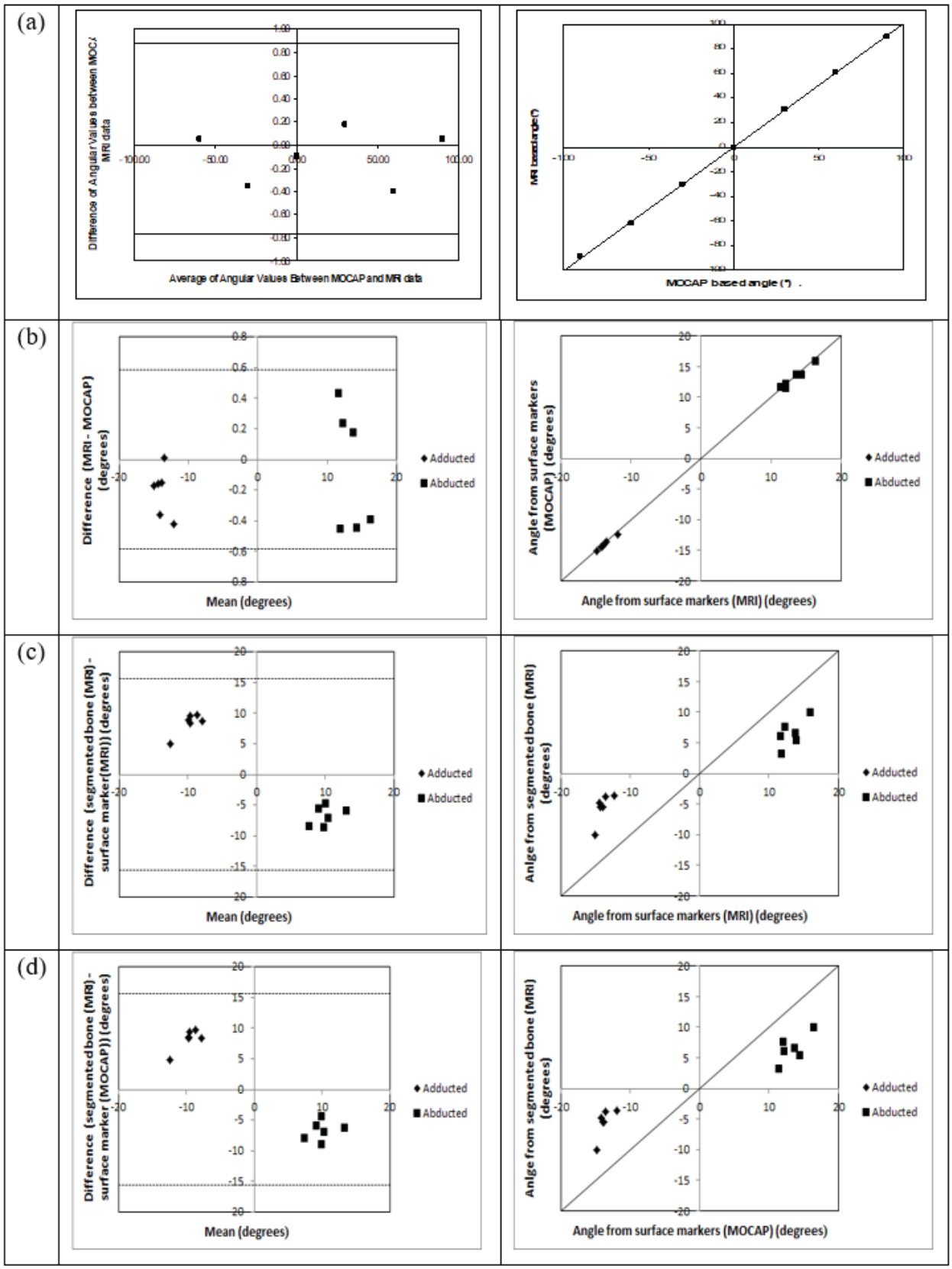

Figure 6. Difference-mean and agreement plots for (a) the in vitro phase and (b) to (d) the in vivo phase, showing the angular measurements calculated from (a) the MRI versus MOCAP marker jig positions; (b) the surface marker (MRI) versus the surface marker (MOCAP); (c) the bone segmentation (MRI) versus surface marker (MRI) and (d) the bone segmentation (MRI) versus surface marker (MOCAP).

markers visible in both MOCAP and MRI universes, so as to support the subsequent validity of data from the segmented bones which could not be cross-referenced to Visual 3D. CCC was calculated as 0.05 and 0.1 between the outputs of Visual 3D for the input data of Surface Markers (MOCAP) and outputs of segmented bone (MRI) for adduction and ab-

duction respectively.

The outputs of MATLAB code for the input data of Surface Markers (MRI) and outputs of segmented bone (MRI) inputs were compared (Fig. 6d) CCC was calculated as 0.05 and 0.09 between the outputs of MATLAB code for the input data of surface Markers (MRI) and outputs of segmented bone (MRI) for adduction and abduction respectively.

A Student-t test for differences between the angular values calculated using surface markers (MOCAP) and segmentation of the internal bone (MRI) yielded a significant difference and therefore evidence of a systematic error for both adducted and abducted positions (p= 0.000095 p=0.000154 respectively). For both the adducted and abducted positions the angle derived from surface-mounted markers over-estimated the change in position of the underlying bony segment.

DISCUSSION

This study addressed the aim of establishing the proof of concept that marker coordinates derived independently using MRI and motion capture, could be accurately co-registered in a highly constrained system in vitro. Using an idealized environment, free from the confounding effect of skin movement artefact, the technical potential of the concept was demonstrated. Although both MRI and MOCAP systems are widely used in the field separately, when two systems are combined, the agreement between the data sets requires rigorous validation prior to use in clinical applications. Theoretical estimations are possible for the technical accuracy of the systems, but these estimates often relate poorly to real-world applications, due to confounders such as inhomogeneities in the magnetic field in MRI scanning and the orientation of the anatomy relative to the field [14].

Combination methods for internal imaging and motion capture have been described but only in abstract form to our knowledge [15] and there does not appear to be any peer reviewed literature formally investigating proof of concept and quantifying the associated errors.

To explore the differences between MRI and MOCAP systems quantitatively. I validated the data obtained from both systems using both bespoke MATLAB code (MATLAB version R2008a, The MathWorks Inc., USA) and Visual 3D (C-Motion Inc, US), the latter considered an industry standard. The novel code showed excellent agreement with the industry standard Visual 3D outputs in the in vitro phase, although we recognize that the benchmark itself will not be completely free of error. The in vivo study confirmed that there is a good agreement between Visual 3D and the MATLAB code in calculating outputs from the same surface marker inputs (MRI) despite the less constrained system.

For the in vitro study, in the absence of the possibility of surface movement relative to the rigid bodies, the MOCAP data represent the best available gold standard against which to compare the MRI outputs. Known sources of error in MR imaging, such as inhomogeneities in the main magnetic field and non-linearity in the applied magnetic field gradients are likely to have an effect when studying large volumes such as used in motion capture. The fixed markers yielded lower RMS error than rotating markers. Furthermore, the error along the Y axis, having a slightly higher systematic offset, was observed to be greater than for the X axis and largest at link position +/-90° when the rotating markers were at the greatest distance from the field iso-centre. In clinical applications for the wrist, neck or ankle it is likely that the ranges of motion would not exceed ± 45° and so this is the region in which the co-registration was required to be most accurate. In our study, for positions within ±60° of the longitudinal axis of the jig, the error in the coordinate data was less than 1 mm in both X and Y directions.

The concordance correlation coefficient results showed very high agreement between the MOCAP data and MRI data in the highly constrained in-vitro simulation. The CCCs for the estimates of surface marker coordinates were very high, and agreement between the two systems for angular rotation was effectively perfect. This provided confidence that, in a constrained system without the confounders of skin artefact, the two systems were able to predict highly similar outputs.

The relationship between surface marker (MOCAP) and segmented bone (MRI) data is similar for abducted and adducted postures. Student-t tests show that there is a significant difference between the angles calculated by surface markers (MOCAP) and internal segmented bone (MRI) data with the surface mounted markers significantly overestimating the rotations occurring in the underlying bony segments. This finding warrants further research as there is the potential to solve for systematic errors such as this is the over-estimation is predictable across a range of rotations or conditions.

One significant advantage of the co-registration of MRI and MOCAP universes is the elimination of the use of invasive techniques such as bone-mounted pin and unnecessary exposure ionising radiation. This would open up the technique to use in patient populations where study is limited due to ethical concerns.

Although this proof of concept study used the wrist

to represent a constrained rotation, there is potential to develop the technique for other joints, particularly joints in which surface mounted markers do not represent well the underlying bony segments. Although the field of view for accurate MRI scanning is limited due to increasing field inhomogeneity at the margins the 3D distortion correction algorithm provided a practically useful field of view in the current study. There is potential to map this further should a wider field of view be required.

I acknowledge that this proof of concept work focused solely on healthy subjects and as a minimum next-step prior to any clinical application, use of the technique to represent motions in the presence of pathological anatomy or function is required.

CONCLUSION

This study demonstrates the technical feasibility of using combination coated markers in both magnetic resonance imaging and optoelectronic motion capture universes, an approach that may have clinical applications for subject-specific studies subsequently.

In this study, the maximum magnitude of the error for the translational data in-vitro was less than 1.5 mm and for angular rotation, an accuracy of better than 1° was attained. In vivo the comparability of directly observed surface mounted markers was lower than in the in vitro simulations but remained within useful limits. A systematic difference was observed between the angles derived from the surface marker data and internal bone segments derived from MRI. Further studies are required to determine whether this systematic error is an intrinsic fault of MOCAP technologies using surface mounted markers. In the interim, care may be required in interpreting surface mounted marker data in terms of absolute values. It may be possible to solve for these differences on an individual basis but further work is required. It appears unlikely that a single correction factor could be applied which would be valid across different patients.

Prior to clinical applications where subject-specific kinematic models may provide insight into disease processes or treatment response models, this technique could now be evaluated in pathological states.

ACKNOWLEDGEMENT

The authors would like to thank to Dr. Richard Holbrey for this technical contribution to the marker registration algorithm.

CONFLICT OF INTEREST

Authors confirm there is no conflict of interest in this manuscript.

References

1. Strimpakos N 'The assessment of the cervical spine. Part 1: Range of motion and proprioception.' Journal of Bodywork and Movement Therapies 2011 15 ;1: 114-124
2. Andriacchi TP, Alexander EJ. 'Studies of human locomotion: past, present and future.' Journal of Biomechanics 2000 33:1217–1224.
3. Stagni, R., Fantozzi, S., Cappello, A., Leardini, A., 'Quantification of soft tissue artefact in motion analysis by combining 3D fluoroscopyand stereophotogrammetry: a study on two subjects.' ClinicalBiomechanics 2005; 20: 3; 320–329.
4. Jonsson, H., Karrholm, J., ' Three-dimensional knee joint movements during a step-up: evaluation after cruciate ligament rupture'. Journal of Orthopedic Research 1994; 12; 6: 769-779.
5. Reinschmidt, C., Borgert, A.J., van den, Nigg, B.M., Lundberg, A., Murphy, N., 'Effect of skin movement on the analysis of skeletal knee joint motion during running.' Journal of Biomechanics 1997; 30: 729-732.
6. Holden J, Orsini J, Siegel K, Kepple T, Gerber L, Stanhope S. Surface movements errors in shank kinematics and knee kinematics during gait. Gait and Posture 1997; 3:217–227.
7. Banks, S.A., Hodge, W.A., "Accurate measurement of three dimensional knee replacement kinematics using single-planefluoroscopy.' IEEE Transactions on Biomedical Engineering 1996; 43; 6 : 638-649.
8. Mundermann L, Corazza S, Andriacchi T, The evolution of methods for the capture of human movement leading to markerless motion capture for biomechanical applications. Journal of NeuroEngineering and Rehabilitation. 2006; 3; 6:1-11.
9. Alexander, E.J, Andriacchi, T.P., Lang, P.K Dynamic Functional Imaging of the Musculoskeletal System, Proceedings of the 1999 ASME Winter International Congress and Exposition, Nashville, Tennessee, November 1999; 14;19: 297-298.
10. Andersen S. Michael, Damsgaard M.,Rasmussen J, Ramsey D, ' Gait & Posture' 2012; 35; 606-611.
11. Joseph Hamill, W. Scott Selbie, and Thomas Kepple ' Unpublished book chapter from Visual 3D software group' Chapter 2 14. 2. 2011.
12. Bland M, Altman D G 'Statistical methods for assessing agreement. between two methods of clinical measurement'. Lancet 1986 ; 327; 8476: 307-310.
13. Lin, L I-Kuei 'Concordance Correlation Coefficient to Evaluate Reproducibility', Biometrics, 1989; 45;1: 255-268.
14. Stanescu T, Hans-Sonke J, Keith Wachowicz, B. Gino F 'Investigation of a 3D system distortion correction method for MR images'. Journal of Applied Clinical Medical Physics 2010; 11;1: 200-216.
15. Lang, P, Alexander, E.J, Andriachi, T.P. 'Functional joint imaging: A new technique integrating MRI and biomotion studies. International Society of Skeletal Radiology Annual Conference 2000.

Hittite Journal of Science and Engineering, 2019, 6 (2) 109-117
ISSN NUMBER: 2148-4171
DOI: 10.17350/HJSE19030000135

An Experimental Investigation of the Influence of Point Angle and Fluctuation in Thrust Force On Chip Morphology

Zulkuf Demir
Batman University, Mechanical Engineering, Batman/Turkey

ABSTRACT

Drilling is a widely used machining method in engineering applications, playing a major part in machining operations. Chip morphology is an indicator, which shows the quality of machining. Especially, chip thickness ratio is a characteristic to show the level of deformation and cutting effects during machining operations. In the present paper, the influences of parameters such as feed rate, spindle speed, point angle, and fluctuation size on the chip morphology investigated. The most influential parameter on the chip thickness was feed rate, while point angle on the chip width. The most favourable chip thickness ratio values and a lower fluctuation size in thrust force were achieved at 100° and 118° point angles. Although the higher fluctuation in thrust force and chip thickness ratio values were observed at 136° and 154° point angles, the most favourable chip morphology was obtained at these point angles. In other words, the higher point angles were found to be advantages in drilling operations to obtain a better chip morphology and chip geometrical dimensions.

Article History:
Received: 2019/02/28
Accepted: 2019/05/29
Online: 2019/06/30

Correspondence to: Zulkuf Demir, Batman University, Mechanical Engineering, Batman, TURKEY
E-Mail: zulkuff75@gmail.com, zulkuf.demir@batman.edu.tr
Phone: +90 505 438 27 01
Fax: +90 488 215 72 01

Keywords:
Drilling; Point angle; Chip thickness; Chip morphology; Chip width.

INTRODUCTION

Drilling is a machining method, improving attractive geometric and dimensional precision in manufacturing operations [1]. Among the conventional metal cutting manufacturing methods, drilling is one of the significant operation, playing a part approximately 33 % in metal machining [2]. Most of the researches are done using drilling manufacturing method to complexity of manufacturing process and application in a very large variety in drilling operations [3]. Many factors influence the drilling process like point angle of drill, the materials of drill and specimen. The tool materials affect the precision of the hole, by the impressions of wear of the drill, surface roughness [4].

Chip formation is a complex process with including both elastic and plastic deformations shapes [5]. These shapes reflect the behaviour of the breaking of the material as three kinds of chips in continuous, adherent, and discontinuous forms. Continuous chip can be achieved when the ductile materials are machined at low feed rates and high spindles speeds, while adherent chip taken place at medium spindle speeds. Moreover, at larger feed rates and smaller point angles chip obtain in brittle and short forms, relative to the increasing in the hardness [6, 7]. In other words, the continuous chip forms, which indicates the better results, are obtained at low cutting conditions, while the more undesired chip forms are obtained at extreme drilling conditions [8, 9]. A composite of chip dimensions commonly points out that two cutting edges angles and their lengths on both side are different. At higher cutting speeds, helix and long ribbon chip form are achieved, while at higher feed rates only long ribbon chips can be gained. This points out that stringent wear on drill taken place at higher feed rates. The loose helix chips cause to little wear on the tool [10]. Furthermore, at smaller spindle speeds short break-up chips come into existence because of the non-continuous distortion in the shear plane. At average spindle speeds provided obtaining the long helical chips. Increasing point angle causes to rise the dimension of the arc of the broken chips. At higher spindle speeds, the continuous chip achieves, while on-shaped discontinuous chip form obtains at lower spindle speed [11].

In machining operations, feed rate causes to inc-

rease pressure on the tool, which leads workpiece to plastic deformation. Lower chip thickness ratio causes to larger grade of shear plane angle, in turn induces low shear stress in the chip and decrease the using up necessary of energy. The plastic deformation region becomes smaller at larger cutting speeds. the chip thickness ratio decreases in with increasing the cutting speed in machining operations [12]. Cutting forces have a major influence on the procedure grade in machining fabricating methods. High cutting forces cause to change the shape of tool and workpiece. Naturally, thrust force increases at high feed rates due to increase the pressure load on the drill, but this pressure decreases with increasing spindle speed [13].

Thrust force and torque in drilling operations are generally carried out by the cutting and chisel edges of the drill. Most of the thrust force and torque are on the cutting edge due to the cutting action. Since the drill radius on the cutting edge is bigger than the radius on the chisel edge. The orientation of the cutting lip causes the specific cutting pressure, which has a sudden change on the efficiency of the cutting. Consequently, the point angle of the tool has a major impact on thrust force values, namely thrust force fluctuation size during the drilling process. Additionally, dispersion of cutting forces on the cutting edge effected by the radius of the drill, workpiece microstructure, and selected conditions, such as spindle speed, feed rate, cutting depth, and tool geometry [3, 14 - 16]. With optimization in results provides a diminution in thrust force and torque of around 40 % [17]. Increasing the point angle cuts down the axial impact on the workpiece and thus lower thrust forces can be achieved at lower spindle speeds. The cutting force especially thrust force in drilling process, brings about tool wear. The increase in point angle produces smaller thrust force at higher spindle speeds [9, 11, 18]. The variation in thrust force can be related to the size of the tool side. The dimension of the tool edge changes at alteration of point angles [19 - 21].

The dissimilarity in the thrust force throughout the drilling operation can be ascribed to the regional alteration in layer thickness of the laminate and the existence of the fore-cracks in the territory of the chisel edge [22, 23]. Cutting forces are essentially depended on the mechanical characteristic of the machined material, process conditions, and tool geometrical construction. When the chisel edge start penetrating in to the workpiece in the first stage thrust force reaches the maximum value until the second edge involves in cutting. The magnitude and varying inclinations in thrust force occurs at the beginning of the operation. Then the thrust force stabilizes for a while and a small alteration in the thrust force may ascribe to little geometric distinctions on the tool cutting sizes. A periodic variation containing an abruptly decrease and gradually raise in thrust force can be attributed to the cutting fluctuation of the saw-teeth structure [24, 25].

The major point of this experimental study is to examine the impact of feed rate, spindle speed and especially point angle of the tip of the drill, on chip thickness, chip width, chip thickness ratio and chip morphology. Furthermore, the investigation of the effect of the fluctuation size in thrust force on the chip geometrical dimensions and chip morphology is another important aim of this experimental research paper.

MATERIALS AND METHODS

Experiments were realized on MEXUS 510 C-II Model Mazak Vertical Centre CNC Milling, as demonstrated in Fig. 1 (a). The AISI 1050 alloy workpieces were preliminary setup in sizes of 100x100x15 mm^3. The holes were pre-drilled 5 mm in diameter as guiding eye. The space between the centres of the holes were arranged 20 mm. The foremost hole centre was calibrated 10 mm from the corners of the sample.

Figure 1. Experimental Setup (a) MAZAK Vertical Centre NEXUS 510 C-II Model Milling Machine and Dynamometer Apparatus, (b) Kistler Type 5233 A Model Data Logger, (c) Computer.

The forces in three directions were measured in Newton unit, by using Kistler 5233A Control Unit of the dynamometer, during drilling processes, as shown in Fig. 1 (a). With the help of data logger of dynamometer as seen in Fig. 1 (b), force data were collected and recorded via a computer, as observed in Fig. 1 (c). Moreover, data was recorded on computer by using specific software, belongs to the Control Units, and data logger. Since the thrust forces in the Z direction are considerably greater than the radial and tangential forces, only the thrust force values are taken into account. Furthermore, workpieces were pre-drilled 5 mm in diameter and 13 mm in depth, in case of cutting liquid using at 1600 rpm spindle speed and 0.1 mm/rev feed rate. After holes were pre-drilled as guiding eyes, they were drilled 10 mm

Table 1. Processing conditions.

Spindle speeds	*n1=800, n2=1200, n3=1600 rpm*
Feed rates	*f1=0.025, f2=0.050, f1=0.075 mm/rev*
Point angles	*Φ1=100°, Φ2=118°, Φ3=136°, Φ4=154°*

in depth from the top surface of the workpieces in conditions, as demonstrated in Table 1.

The impact of the point angle on the outcomes studied in performed operations. For this reason, four different point angles, which were 100°, 118°, 136°, and 154° selected. The both sides or cutting edges of drills, with 10 mm in diameter, were grinded, on a grinder machine to constitute cutting edges in different point angles. Tools were fastened to spindle of CNC machine with the help of the fastening equipment, as the clamping equipment grasped all of the shank of the drill.

The fluctuation sizes in thrust force, obtained during the drilling operations, are shown as in Fig. 2. By the help of Kistler 5233 A-model dynamometer thrust forces measured during the drilling operations. The data logger saved thrust forces values in hundreds in one-second time. Only one minimum and one maximum of these data of the fluctuation size in thrust force taken into account for per unit of a second time. Thus, the deviation in thrust force in the processes were gained from the beginning of the drilling until it was completed and drill tool started regurgitating. The fluctuation size in one-second time calculated as seen in equation 1.

$$\text{Fluctuation Size in Thrust Force}\,(\%)_{1Second} = \frac{(F_{max} - F_{min})}{F_{max}}.100 \quad (1)$$

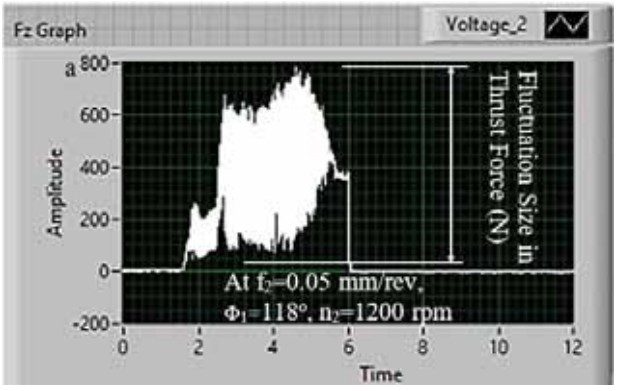

Figure 2. Fluctuation size in thrust force.

In Fig. 2 b, the chip morphology can be seen. During the drilling operation, removed chips collected for each experiment, separately. Chips morphology and chip geometrical properties were investigated by using chip photos, which were taken by using macro photo camera. Then the chips thicknesses and their widths were measured at six different positions by using digital clapper as shown in Fig. 3. The arithmetic average values of these measured data were taken into account for chip thicknesses and chip widths for each experiment separately.

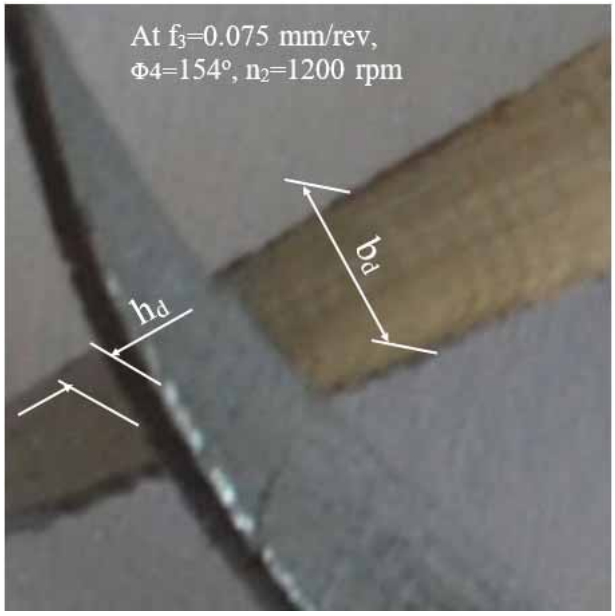

Figure 3. Chip thickness (h_d) and chip width (b_d).

THEORY OF CHIP DIMENSIONS

The shape of the tools, particularly the point angle of the drills, have an important effect on the chip geometrical dimensions, such as chip thickness and chip width in drilling operations. Because the cutting speed has an alteration on the cutting side. While at the circumference of the cutting speed takes the greatest value, these values approach zero close to the centre-line of the web of the drill, where the tool side combined to a chisel form [26]. Moreover, according to the results obtained from the experimental procedure of the present paper, with increasing point angle from 100° to 154°, thrust forces and also fluctuation in thrust forces were decreased. Even at higher spindle speeds the optimum chip shapes without deformations cracks and serration form were observed. Removed chips geometrical dimensions indicates the quality of the drilling operations, hence investigating the chip thickness and chip width consistent with the selected parameters have a major phenomenon. In Fig. 4 a and b, the shape of the tip of the drill and chip geometry can be seen. According to the chip geometry, chip geometrical dimensions, such as chip thickness and chip width can be calculated by using equations from 1 to 5, which written as at below.

If the specimens were not fore-drilled the dimension of the tool sides would be $|C_{1.1}\text{-}A_1|$, $|C_{1.2}\text{-}A_1|$, $|C_{1.3}\text{-}A_1|$, $|C_{1.4}\text{-}A_1|$ for 100°, 118°, 136°, 154° point angles, respectively. But in the present paper, we fore-drilled specimens 5 mm in diameter to exclude the effectuate of the chisel side. Consequently, the dimension of the tool side, which were used in the present paper, were $|B_1\text{-}A_1|$, $|B_2\text{-}A_1|$, $|B_3\text{-}A_1|$, $|B_4\text{-}A_1|$ for 100°, 118°, 136°, 154° point angles respectively.

In the present investigation the specimens were fore-drilled 5 mm in diameter ($Ød_o$) to exclude the influence of the chisel edge. In case of the selected specimens, not pre-drilled, the un-deformed chip width namely the dimension of tool side can be computed with the help of equation 2, consistent with Fig. 5 (b). l is equal to the un-deformed chip width (b_D) of samples without pre-drilled. It had been identified with dimension of $|C_1A_1|$ as seen in Fig. 4 a.

$$l = |C_1A_1| = b_D = \frac{d_h - d_o}{2.\sin\varphi} \text{ mm} \quad (2)$$

The thickness of the un-deformed chip (h_d) can be computed relying on feed rate (f_z) and one half point angle (φ) as in equation 3, as demonstrated in Fig. 4 (a).

$$h_d = h_{de} = f_z.\sin\varphi \text{ mm} \quad (3)$$

As seen in Fig. 3 (a) the region of $|C_1C_{11}\text{-}\ A_1A_{11}|$ is representing the un-deformed chip in the operation, in which the workpieces are not fore-drilled. These can be computed relying on the dimensions of the chips (h_d and b_d), as demonstrated in Equation 4.

$$A_c = |C_1C_1^1|.|C_1A_1| = h_d.b_d \text{ mm}^2 \quad (4)$$

In the present paper, the specimens were fore-drilled 5 mm ($Ød_o$) in diameter, as guiding eye. Consequently, in fore-drilling parameters the size of the tool side, in other words the width of un-deformed chip and un-deformed chip thickness are specified as (b_{de}) and (h_{de}), respectively. The effective un-deformed chip thickness is equal to the un-deformed chip thickness as shown in equal 2. But the effective un-deformed chip width is different from un-deformed chip width, because of the diameter ($Ød_o$) of fore-drilled hole. It is described as in equation 5. le is equal to the effective un-deformed chip width of samples with pre-drilled holes, which is specified in Fig. 4 (a), the dimension of $|B_1A_1|$.

$$l_e = |B_1A_1| = b_{de} = \frac{d_h - d_o}{2.\sin\varphi} \text{ mm} \quad (5)$$

In the present case, the effective are of un-deformed chip (Ae) can be calculated relying on effective un-deformed chip width (b_{de}) and (h_{de}), which is shown in equation 6.

$$A_{ce} = |B_1B_1^1 - A_1A_1^1| = h_{De}.b_{De} \text{ mm}^2 \quad (6)$$

In the present paper, there are 4 dissimilar point angles (Φ1, Φ2, Φ3, Φ4) are expressed in the Fig. 4 (b), which were selected in experimental study, as 100°, 118°, 136°, 154° respectively. Consistent with the form of tool point, the alteration of cutting side dimension (l) and (l_e), in other words un-deformed chip widths (b_d) and (b_{de}), are replaced with different of point angles.

The zone of un-deformed chip in the processes, considerably depend on the tool side dimension, in other words un-deformed chip wideness. Consistent with the equations 2, 4, and 5, the effectual un-deformed chip height (h_d), the tool side dimension (l_e) in other words un-deformed chip width (b_d), and accordingly, un-deformed chip area (A_{ce}) can compute in compliance with feed rate and point angle. Relying on the form of the tip of the tool, as mentioned at above, the un-deformed chip height is only associated with both one cutting edge feed rate (f_z) at per rotation and point angle. The drill side dimension in other words un-deformed chip width is depending on diameter and point angle of the drill. Hence forth, every both one feed rate and one-point angle

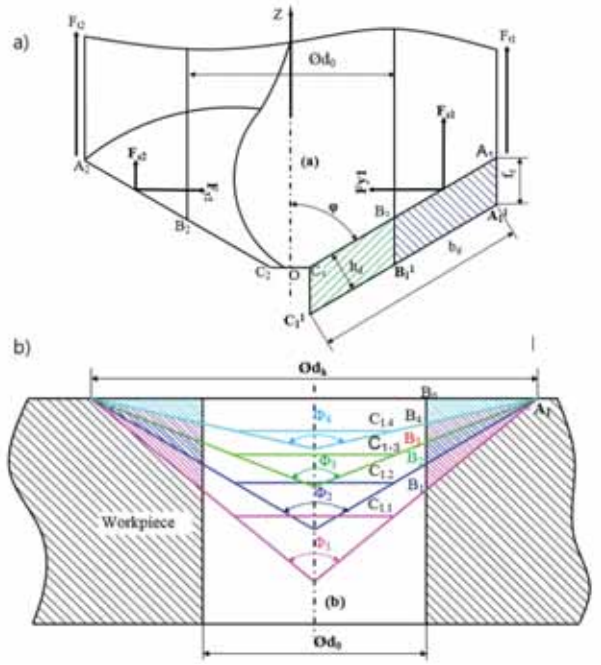

Figure 4. (a) The front view of the tip of the drill, chip thickness and chip width (b) removal chip area consistent with the point angle and pre-drilled hole geometry.

Table 2. Computed un-deformed chip dimension are consistent with feed rate and point angle, demonstrated with icon.

Icon	Feed Rate	Point Angle	$h_{de}=h_d$	b_d namely l_e	Ace=h_{de}*b_{de}
A	f_{z1}=0.025 mm/rev	Φ1=100°	0.0161 mm	3,2635 mm	0.0525 mm²
B	f_{z2}=0.050 mm/rev		0.0321 mm		0.1048 mm²
C	f_{z3}=0.075 mm/rev		0.0482 mm		0.1573 mm²
D	f_{z1}=0.025 mm/rev	Φ2=118°	0.0129 mm	2,9166 mm	0.0376 mm²
E	f_{z2}=0.050 mm/rev		0.0258 mm		0,0753 mm²
F	f_{z3}=0.075 mm/rev		0.0386 mm		0,1126 mm²
G	f_{z1}=0.025 mm/rev	Φ3=136°	0.0094 mm	2,6963 mm	0,0254 mm²
H	f_{z2}=0.050 mm/rev		0.0187 mm		0,0504 mm²
I	f_{z3}=0.075 mm/rev		0.0281mm		0,0758 mm²
J	f_{z1}=0.025 mm/rev	Φ4=154°	0.0056 mm	2,5658 mm	0,0144 mm²
K	f_{z2}=0.050 mm/rev		0.0112 mm		0,0287 mm²
L	f_{z3}=0.075 mm/rev		0.0169 mm		0,0434 mm²

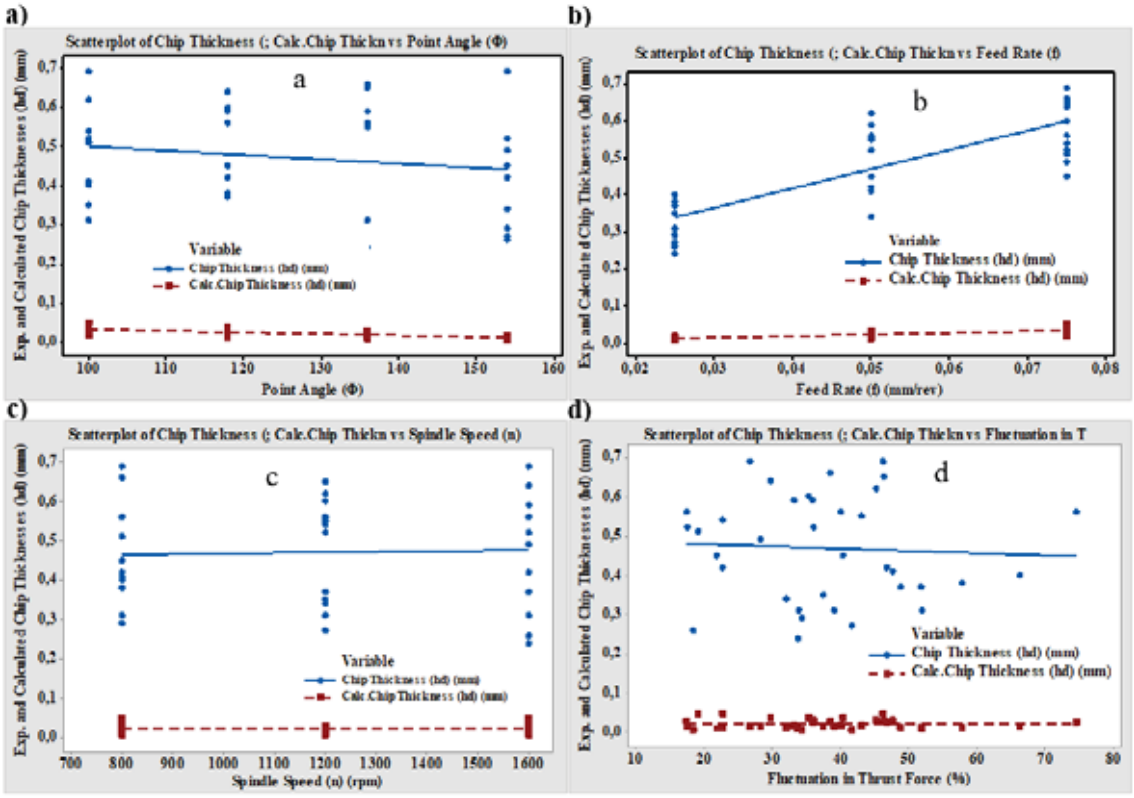

Figure 5. The effect of (a) point angle (b) feed rate, (c) spindle speed, (d) fluctuation in thrust force on experimental and calculated chip thicknesses.

conditions pairs are demonstrated with icons: A, B, C, D, E, F, G, H, I, J, K, and L, as seen in Table 2. The effective undeformed chip area (A_{ce}), in Table 2, was calculated according to equation 5.

Chip geometrical dimensions demonstrate the quality of the drilling. Especially, the chip thickness ratio, which can be identified proportion of distorted chip thickness to the un-distorted chip thickness, is a major geometrical characteristic, which demonstrates the quality of the process. This quality is evaluable according to the chip thickness ratio. When chip thickness ratio is bigger than 60 not available, between 60-30 confined available, chip thickness ratio is between 30-11, it is available, and when chip thickness ratio is between 10-3 is the best. Additionally, the chip thickness ratio is smaller than 3 is good in machining operations, which is demanding ratio with regard to the quality of the process [27]. In this study, chip morphology was investigated according to the chip geometrical dimensions, especially chip thickness ratio.

RESULTS AND DISCUSSION

Chip Geometrical Dimensions and Fluctuation Size in Thrust Force

Due to they are important dimensions, the chip geometrical dimensions, such as chip thickness, chip width and chip morphology indicates the quality of the drilling operation. In this study, the theoretical chip thickness and chip width calculated using equations 2 and 4 consistent with the feed rate for per tool side (f_z) and point angle. Experimental chip thickness and chip width dimensions were measured by using digital clapper as seen in Fig. 3. Therefore, the calculated and experimental chip thickness and width values were compared.

In Fig. 5 a, b, c, and d, the influence of point angle, feed rate, spindle speed, and fluctuation size in thrust force on both experimental and calculated chip thicknesses values can be shown, respectively. According to these graphs, the most influential parameter on chip thicknesses was feed rate, which followed by point angle, fluctuation size in thrust force and spindle speed, respectively. The experimental chip thickness values were greater than the calculated values. Moreover, with increasing point angle and fluctuation in thrust force experimental chip thickness values were little decreased, but it was increased linearly with increasing feed rate. However, spindle speed did not affect neither experimental nor calculated chip thickness values. Moreover, this consequence verifies the accuracy of the equations 4, 5, and 6.

The effect of point angle on the experimental chip thickness was smaller than calculated chip thickness, due to motions and deformations effect in drilling operations. Calculated chip thickness was decreased linearly by increasing point angle from 100° to 154°. Chip thicknesses values were

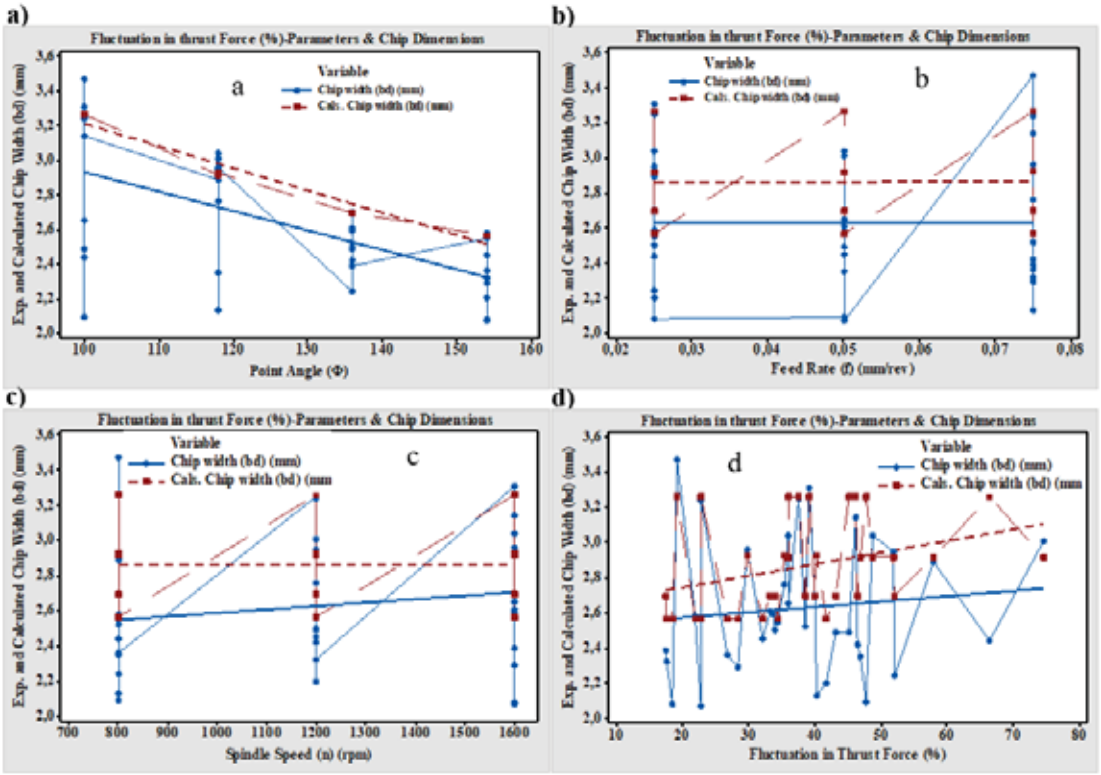

Figure 6. The effect of (a) point angle, (b) feed rate, (c) spindle speed, (d) fluctuation in thrust force on experimental and calculated chip widths.

not change with changing spindle speed, while there was a little variation in chip thicknesses values with changing fluctuation size in thrust force. However, both experimental and calculated chip thicknesses values were increased linearly with increasing feed rate. Calculated chip thickness shown an increase with increasing feed rate according to equation 2. In equation 2, un-deformed chip thickness relies on only the feed rate and point angle of per cutting edge in one revolution.

Like chip thickness, chip width dimension effects the removal chip volume in drilling operations. The effects of the parameters, namely point angle, feed rate, spindles speed, and fluctuation size in thrust force are shown in Fig. 6 a, b, c, and d, respectively. Consistent with the equation 4, feed rate and spindle speed did not have any effect on calculated chip width, while they had a little effect on experimental chip width, due to the motion and thrust effects of the drill. According to the equation 4, the calculated chip width decreased regularly with increasing point angle from 100o to 154o. In comparison with chip thickness, the chip width decreased linearly with increasing point angle. This outcome indicates that chip width is a parameter, depending on point angle of drill, in drilling operations. Both experimental and theoretical chip widths values graphs shown a collateral variation. Fluctuation size in thrust force effected the calculated chip width values more than the experimental values. With increasing fluctuation size in thrust force, chip width values were increased linearly.

Main effect of parameters on both calculated and experimental chip thicknesses and chip thick ratio can be demonstrated as in Fig. 7 a, b, and c, respectively. According to these graphs, both calculated and experimental chip thickness values were regularly increased with increasing feed rate, but calculated chip thickness decreased. At point angles bigger than 136° experimental chip thickness linearly decreased. Spindle speed had not any effect on calculated chip thickness. However, experimental chip thickness values were shown a little changing in the direction of increase, due to the motion and thrust effects during drilling.

The most influential parameter on chip thickness ratio was feed rate. Therefore, at higher selected feed rates chip thickness was regularly decreased, but with increasing point angle chip thickness ratio was increased. Although this result is not demanded in machining operations they are not poor, due to the differences between calculated and experimental chip thickness values, according to the point angle. Calculated chip thickness values were small according to equation 2, but experimental chip thickness values were enormous. Thus, the ratio of these values naturally resulted in high values. Chip width is a dimensional result in machining operations, affecting the volume of the removal chip. According to the equation 4, the most influential parameter on chip width is point angle. Therefore, increasing in point angle provided to decrease in calculated chip width, as seen in Fig. 7 d. However, calculated chip width is not shown any variation with changing both spindle speed and feed rate. While the variation in both experimental and calculated chip widths shown a collateral decreasing with increasing

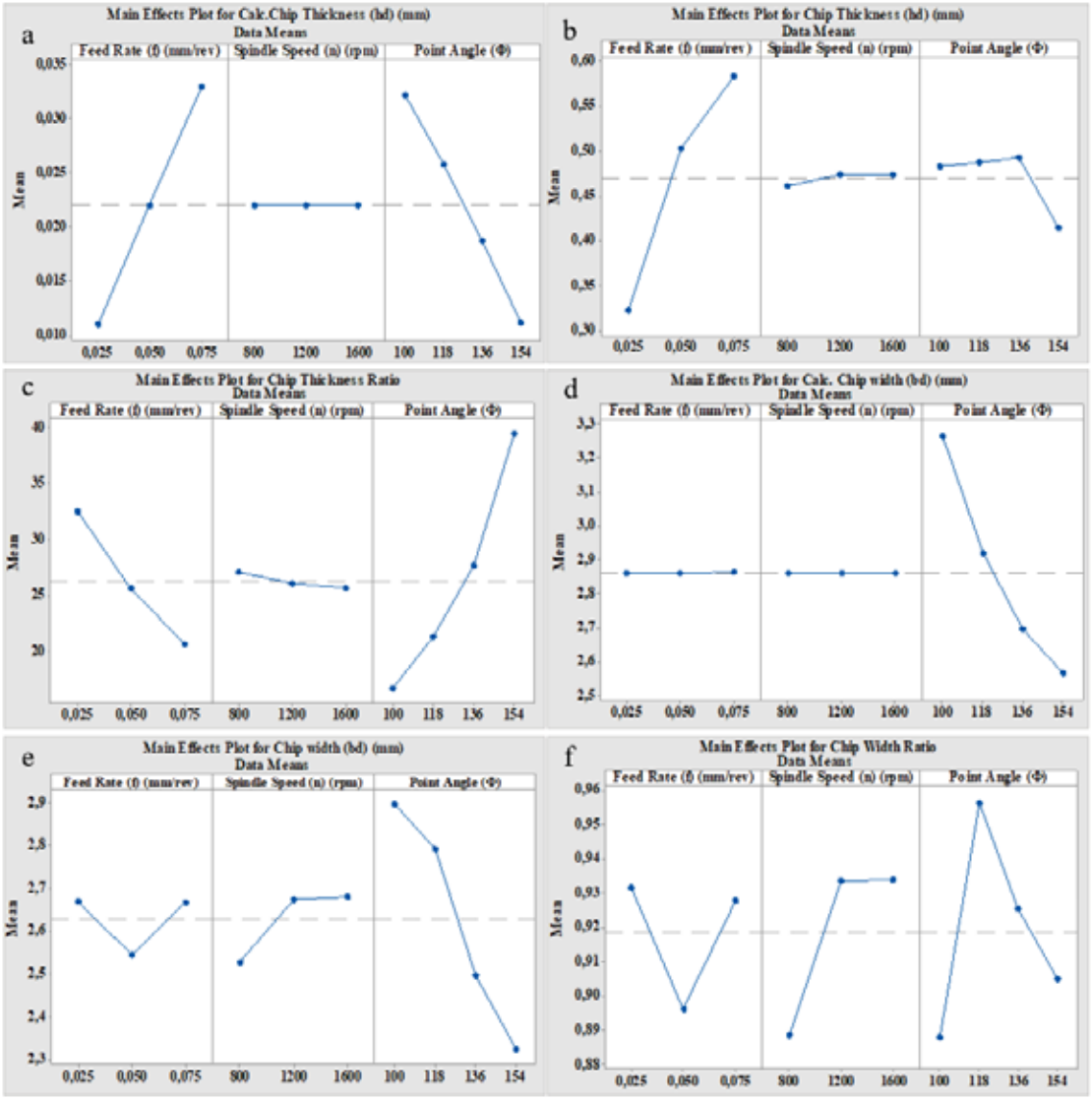

Figure 7. Main effect of parameters on (a) calculated chip thickness (b) experimental chip thickness (c) chip thickness ratio (d) calculated chip width (e) experimental chip width (f) chip width ratio.

point angle, there was a little changing only in experimental chip width values with increasing both spindle speed and feed rate, as observed in Fig. 7 e.

Chip thickness ratio was got its peak value at point angles between 100° and 118°, but then it was decreased regularly with increasing point angle to 154°. It was reduced at smaller feed rates, but it was increased at higher selected spindle speeds. However, this variation in chip thickness ratio consistent with both feed rate and spindle speed was shown an irregular changing, as seen in Fig. 7 f.

Chip Morphology

Chip thickness ratio is a major result in machining operations, identifying the quality of the process according to the morphology of removed chips. The most demanded chip ratio values in the machining operations are between 3-10. When the removal chip thickness ratio is in these limits, it shows that the machining operation carried out in the most appropriate conditions. Additionally, continuous, ductile, and longer form chips indicate better machining conditions. The effect of chip thickness ratio, chip width ratio and fluctuation size in thrust force on chip morphology can be seen in Fig. 8 a, at 0,025 mm/rev, in Fig. 8 b, at 0,050 mm/rev, and in Fig. 8 c, at 0,075 mm/rev feed rates.

At 0,025 mm/rev feed rate, chip morphology showed variations depend on chip thickness ratio, chip width ratio, and fluctuation size in thrust force, from brittle, shorter chip forms to continuous, ductile, and longer. Even at lower chip thickness ratios and fluctuation in thrust forces, the chips removed in the form of brittle and shorter forms, at 100° and 118°, but at 136° and 154° point angles, even at higher chip thickness ratio, chip width ratio, and fluctuation size in thrust force values, removed chips were in long, continuous and ductile forms, which indicate better results. However,

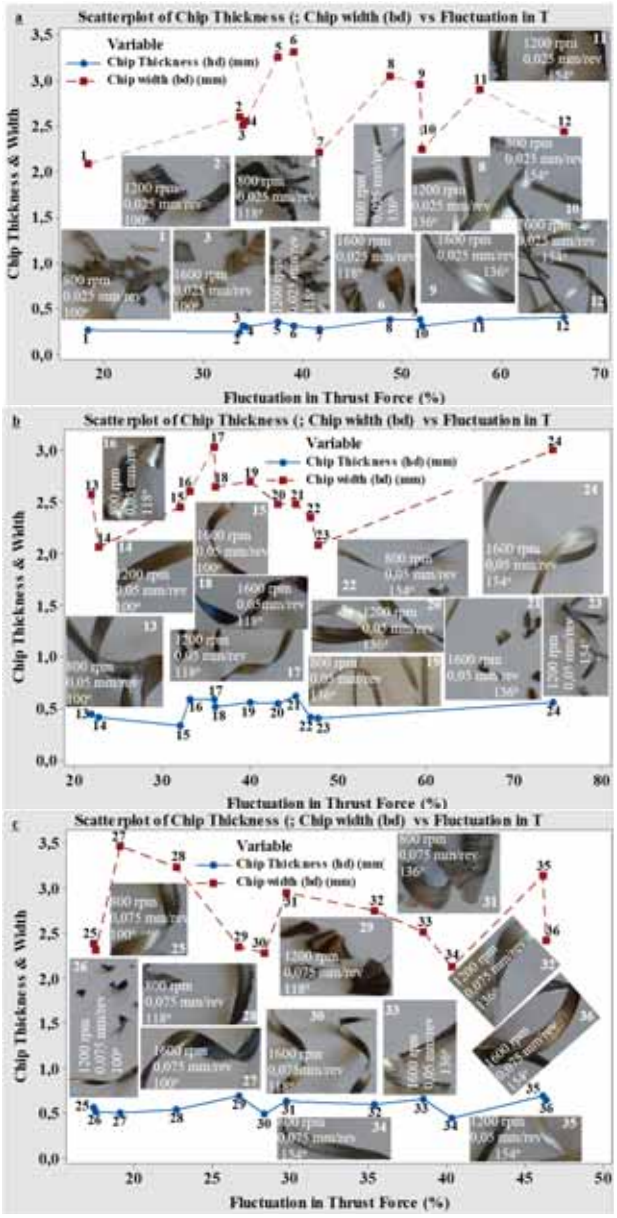

Figure 8. Chip morphology according to chip thickness ratio, chip width ratio, and fluctuation size in thrust force, (a) at 0,025 mm/rev, (b) at 0,050 mm/rev, (c) at 0,075 mm/rev feed rates.

there were deformation traces and cracks on the chip morphology at 0,025 mm/rev feed rate. Additionally, the lower fluctuation in thrust force (%) recorded at 154° point angle and chip thickness ratio values were bigger than 21.

The least chip thickness values were recorded as 12,77 µm and 10,58 µm at 100° point angle, at both 0,050 and 0,075 mm/rev feed rates, respectively. But there were deformation cracks and traces on removed chip shapes collective with burning marks at higher spindle speeds. At 0,050 mm/rev feed rate, both chip thickness and chip width ratios were decreased at higher point angles. Although there was higher fluctuation size in thrust force at higher point angles, chip thickness and chip width ratios were decreased and removed chips were obtained in the continuous, ductile, and longer forms.

At 0.075 mm/rev feed rate, the effect of thrusting causes to deteriorate the deformed chip morphology as deformation traces and cracks on the chips. Beside, at higher spindle speed, there were burning marks in the black colour on the deformed chips, at all selected the remain parameters. At 0,050 mm/rev feed rate and 1600 rpm spindle speed conditions, the removed chip form can be shown as an example for this phenomenon, as seen in Fig. 8 c.

According to the chip thickness and chip width ratios criterion, also fluctuation size in thrust force, 100° and 118° point angles were appropriated parameters. However, according to the chip morphology criterion, 136° and 154° point angles were more appropriate parameters. In addition to all achieved results, namely chip thickness, chip width, chip thickness ratio, chip width ratio, and fluctuation size in thrust force, the most appropriate parameters were 0,025 mm/rev feed rate - 800 rpm spindle speed, 0,050 mm/rev feed rate- 1200 rpm spindle speed, and 0,075 mm/rev feed rate – 1600 rpm spindle speed couples.

CONCLUSION

Chip morphology and especially distorted chip sizes like chip thickness, chip width, chip width and chip thickness ratios, affect the results in machining operations. Continuous, ductile, and longer chip forms, which demanded deformed chip forms, while brittle and shorter chip forms, which were undesired in machining operations.

The most influential parameters on both theoretical and experimental chip thicknesses were feed rate and point angle, while little influential parameters only on experimental chip thickness were spindle speed and fluctuation size in thrust force.

Chip thickness ratio was bigger than 10, while chip width ratio smaller than 1,1. This indicated that chip thickness ratio was more changeable dimensional parameter than chip width and it was the most influential dimensional result, which affects the quality of the machining operations.

The most influential parameters on chip thickness were feed rate, followed by point angle. However, the most influential parameter on chip width was only point angle. Therefore, point angle was a vital parameter, affecting the chip morphology and chip dimensional geometries in drilling operations.

Decreasing in point angle provided appropriate chip morphology in drilling operations, even at higher fluctuations in thrust force and chip thickness ratio. While at lower point angles the brittle and shorter chip morphology were obtained, at higher point angles continuous, ductile, and

longer chip forms were obtained. The most appropriate chip morphology was resulted in at lower feed rate, higher spindle speed and point angles. However, at higher spindle speeds there were burning marks on the removed chips in black colour. Additionally, even at higher spindle speed and point angles, the most demanded chip morphology was achieved.

According to chip thickness ratio and chip morphology criterion, the most appropriate parameters couples were 800 rpm-0,025 mm/rev, 1200 rpm-0,050 mm/rev, and 1600 rpm-0,075 mm/rev spindle speeds and feed rates, respectively.

The lower chip thickness ratio values were recorded at 100° and 118° point angles, at 0,025 mm/rev feed rate and 800 rpm spindles speed. However, the obtained deformed chips were in brittle and shorter forms.

References

1. Thakre, A. A. and Soni, S. (2016) Modelling of bur size in drilling of aluminium silicon carbide composites using response surface methodology, Eng. Sci. Technol. Int. j., http://dx.doi.org/10.1016/j.jetch.2016.02.007.
2. Chen, W. C. and Tsao, C. C. (1999) Cutting performance of different coated twist drills, J. Mater. Process. Technol. 88, 203 – 207.
3. Lazar, M. B. and Xiraouchhakis, P. (2013) Mechanical load distribution along the main cutting edges in drilling, J. Mater. Process. Technol., 213, 245 – 260.
4. Kalidas, S. Devor, R. E. Kapoor, S. G. (2001) Experimental investigation of the effect of drilling coatings on hole quality under dry and wet drilling conditions. Surf. Coat. Technol., 148, 117 – 128.
5. Taskesen, A. Kütükde, K. Biermann, D. (2013) Experimental investigation and multi-objective analysis on drilling of boron carbide reinforced metal matrix composites using grey relational analysis, Measurement, 47, 321-330.
6. Celik, Y. H. (2014) Investigation the effect of cutting parameters on the hole quality in drilling the Ti-6Al-4V. Mater. Technol., 95, 669-295.
7. Caydas, U. and Celik, M. (2017) Investigation of the effects of cutting parameters on the surface roughness, tool temperature and thrust force in drilling of AA 7075-T651 alloy, J. Polytech., 20(2), 419–425.
8. Caydas, U. Hascalık, A. Buytoz, O. Meyveci, B. (2011) Performance evaluation of different twist drills in dry drilling of AISI 304 austenitic stainless steel, Mater. Manuf. Process., 26, 951-960.
9. Palanikumar, K. and Muniaraj, A. (2014) Experimental investigation and analysis of thrust force in drilling cast hybrid metal matrix (Al-15%SiC-4%graphite) composite, Measurement, 53, 240–250.
10. Sultan, A. Z. Sharif, S. Kurniawan, D. (2015) Chip formation when drilling AISI 316L stainless steel using carbide twist drill, Procedia Manufacturing, 2nd Int. Mater. Ind. Manuf. Eng. Con., MIMEC2015 4-6 February 2015, Bali Indonesia, 2, 224-229.
11. Samy, G. S. and Kumaran, S. T. (2017) Measurement and analysis of temperature, thrust force and surface roughness in drilling of AA (6351)-B4C composite, Measurement, 103, 1–9.
12. Thamizhmanii, S. and Hasan, S. (2012) Machinability study using chip thickness ratio on difficult to cut metals by CBN cutting tool, Key Eng. Mater., 504-506, 1317–1322.
13. Celik, Y. H. Yildiz, H. Ozek, C. (2006) Effect of cutting parameters on workpiece and tool properties during drilling of Ti-Al-4V, Wear Test., 46, 1526–1535.
14. Ema, S. (2012) Effect of twist drill point geometry on torque and thrust. Sci. Rep. Fac. Educ. Gifu Univ. (Nat. Sci.) 36, 165-174.
15. Ramesh, B. Elayaperumal, A. Satishkumar, S. (2014) Effect of the standard and special geometry design of a drill body on quality characteristics and multiple performance optimization in drilling of thick laminated composites, Procedia Eng., 12th Global Con. Manuf. Manage., GCMM 2014 97, 390-401.
16. Wang, J. Feng, P. Zheng, J. Zhang, J. (2016) Improving hole exit quality in rotary ultrasonic machining of ceramic matrix composites using a compound step-taper drill, Ceram. Int., 42, 13387-13394.
17. Paul, A. Kapoor, S. G. DeVor, R. E. (2005) Chisel edge and cutting lip shape optimization for improved twist drill point design, Int. J. Mach. Tools Manuf., 45, 421-431.
18. Sui, J. Kountanya, R. Guo, C. (2016) Development of a mechanistic force model for CNC drilling process simulation, Procedia Manuf., 44th Proceedings of the North America Manuf. Research Inst. SME, 5, 787–797.
19. Tsao, C. C. and Hocheng, H. (2003) The effect of chisel length and associated pilot hole on delamination when drilling composite materials, Int. J. Mach. Tools Manuf., 43, 1087-1092.
20. Ghosh, R. Sarkar, R. Paul, S. Pal, S. K. (2016) Biocompatibility and drilling performance of beta tricalcium phosphate: Yttrium phosphate bioceramic composite, Ceram. Int., 42, 8263-8273.
21. Ahmadi, K. and Savilov, A. (2015) Modeling the mechanics and dynamics of arbitrary edge drills, Int. J. Mach. Tools Manuf., 89, 208-220.
22. Saoudi, J. Zitoune, R. Mezlini, S. Gururaja, S. Seitier, P. (2016) Critical thrust force predictions during drilling: Analytical modeling and X-ray tomography quantification, Comp. Str., 153, 886–894.
23. Anand, S. R. and Patra, K. (2017) Mechanistic cutting force modelling for micro-drilling of CFRP composite laminates, CIRP J. Manuf. Sci. Technol., 16, 55–63.
24. Karimi, N. Z. Heidary, H. Minak, G. (2016) Critical thrust and feed prediction models in drilling of composite laminates, Comp. Str., 148, 19-26.
25. Jia, Z. Fu, R. Niu, B. Qian, B. Bai, Y. Wang, F. (2016) Novel drill structure for damage reduction in drilling CFRP composites. Int. J. Mach. Tools Manuf., 110, 55–65.
26. Akkurt, M. (1996) Talaş kaldırma yöntemleri ve takım tezgahları, 3rd, Birsen Press, İstanbul.
27. Rey, R. A. LeDref, J. Senatore, J. Landon, Y. (2016) Modelling of cutting forces in orbital drilling of titanium alloy Ti-6Al-4V, Int. J. Mach. Tools Manuf., 106, 75–88.

Hittite Journal of Science and Engineering, 2019, 6 (2) 119-122
ISSN NUMBER: 2148-4171
DOI: 10.17350/HJSE19030000136

Drying of Drilling Sludge: Conventional and Microwave Drying

Suna Ozden Celik[1], Esra Tinmaz Kose[1], Soner Celen[2], Gizem Akin[1], Aylin Akyildiz[3]
[1] Namık Kemal University, Department of Environmental Engineering, Çorlu/Tekirdağ, TURKEY
[2] Namık Kemal University, Department of Mechanical Engineering, Çorlu/Tekirdağ, TURKEY
[3] Namık Kemal University, Department of Civil Engineering, Çorlu/Tekirdağ, TURKEY

ABSTRACT

Drilling sludge (DS) is one of the most important waste generated during drilling activities and management of drilling sludge (DS) is highly complicated because of its high moisture content, complex constituents and chemical characteristics. Treatment, transportation and disposal costs of DS are important issues about the management of DS. Restrictive environmental legislation has led to the optimization of solid–liquid separation. Drying process can be defined as an effective solution to reduce sludge mass and thus to reduce management cost.

In this study, conventional and microwave drying of DS were compared in terms of process efficiency. Microwave power levels, drying temperature, drying times, moisture content of the DS and energy consumption of drying processes were defined as control parameters. Microwave power levels of 120 and 700 W and 60 and 80 °C were performed to dry the DS sample for microwave and conventional drying, respectively. The results showed that the microwave drying was more effective than conventional method in the view of drying times and energy consumption.

Keywords:
Drilling sludge; Moisture, Energy; Conventional drying; Microwave drying

Article History:
Received: 2017/12/13
Accepted: 2018/11/06
Online: 2019/06/30

Correspondence to: Suna Özden Çelik, Namık Kemal University, Çorlu Engineering Faculty, Department of Environmental Engineering, Çorlu/Tekirdağ, TURKEY;
Tel: +90 282 2502362;
Fax: +90 282 2509924;
E-mail: sunacelik@nku.edu.tr

INTRODUCTION

Increasing numbers of petroleum and natural gas exploration, in parallel with rapidly increasing rise in fuel demand of the mankind, created a rise in the amounts and the types of the wastes, as well as environmental pollution problems.

In the oil industry, there are several steps namely exploration, drilling, production, transportation, handling, and refining from starting the exploration of oil and/or natural gas to their consumption. During these activities, solid, liquid, and gas wastes are emerged due to use of various chemicals and techniques. One of the most important wastes of these activities is drilling mud waste. Drilling mud (also known as drilling fluid) is used for cleaning the hole of cuttings created during the drilling process and other special purposes. Drilling mud is prepared by adding various organic, inorganic and antibacterial chemical additives for controlling the physical and chemical properties. During the drilling process, the cuttings are also carried to the ground within the drilling mud and thus drilling waste mud is produced.

There are on-site (in-situ) and off-site (ex-situ) methods for the removal of hydrocarbon-based (petroleum and natural gas) pollution from soil and groundwater. The ex-situ methods are defined as treatment for polluted soil, rubble material, sludge or hazardous materials and wastes in mobile or fixed installations established outsides. The applications used within this method are usually soil washing, thermal treatment, biological treatment (pump & treat technology), chemical treatment, ion exchange, use of organic solvents or water based washing solutions, metal extraction, and solidification/stabilization [1]. On the other hand, applicable in-situ methods include bioremediation, phytoremediation, soil washing, soil vapor extraction, vitrification, solidification/stabilization, thermal desorption etc.

This paper was presented orally in 6th International Symposium on Mining and Environment – ISME 2017, 27st - 29rd of September 2017, Bodrum, Turkey and its abstract was published in Conference Abstract Book.

As mentioned above, there are many different treatment methods for drilling sludge. However, the drilling sludge is characterized by its high moisture content and low bulk density, which result in a low conversion efficiency as well as difficulties in its collection, storage, and transportation. The high moisture content of the drilling sludge is a critical factor determining its disposal options [2, 3].

Drying process is an effective solution to reduce the mass of the sludge and thus to reduce its management cost. Drying is an energy intensive processes, and for that reason it is more important to select the technology that consumes less energy [4].

Microwave drying differs markedly from conventional drying methods. In conventional heating systems, the energy is transferred through conduction, convection and radiation. Due to the temperature difference between the hot surface and the colder interior, the heat is gradually transferred from the surface to the interior of the material in conventional drying. In microwave heating, energy is supplied directly to materials by molecular interaction with the electromagnetic field generated. In the case of microwave drying, the electromagnetic field influences the material as a whole. The water molecules in the material vibrates millions of times a second. The energy occuring by this vibration makes the moisture in the material evaporate quickly [5-7].

Microwave drying is a method used for the treatment of a wide variety of waste types and has many potential advantages. Microwave application is a fast and flexible process that can be controlled quickly (selectable) and easily (remotely controllable) and accessible to high temperature values. Microwave heating requires less than 1% of the time required for conventional heating methods. Compared to other conventional systems such as conventional drying, it has the advantage of being a cleaner energy source and energy saving. Microwave application, which can also be used for in-situ treatment of wastes, is a method that has significant gains in terms of providing a significant reduction in waste volume, treating or immobilizing hazardous compounds that meet the legal requirements for waste handling and storage.

Microwave drying has been one of the topics investigated in the treatment of various wastes in recent years due to its outstanding features compared to conventional heating methods [8- 12].

Chien (2012) previously conducted laboratory-scale studies on the microwave heating remediation of petroleum hydrocarbons contaminated sites to field measurements. The study suggested that the microwave heating was a permanent remediation method as well as cost effective and time efficient. Moreover, the results showed that polluted areas could be improved to such an extent that they can later be used for agricultural purposes [8].

Shang et al. (2006) investigated the microwave heating as a new method for the treatment of petroleum-contaminated drill cuttings by examining the thermal desorption of petroleum from the perspective of the influence of power, duration of treatment and moisture content. In the study, it was found that residual oil concentration would decrease considerably due to the microwave treatment for only 20 sec of petroleum-contaminated waste residues [10].

In this study, the drying of drilling sludge via conventional and microwave processes was studied, and the energy consumptions and drying times of these two methods were compared.

MATERIALS AND METHODS

Material and Sample Preparation

In this study, the drilling sludge (DS) was obtained from the petroleum and natural gas drilling operations carried out by Turkish Petroleum (TP) in Thrace Region. The sludge samples were stored at 4 °C. Triplicate samples was retrieved to room temperature before using for the experimental studies. The sample with a mass of 183,5±0,5 g was put into glass container having a diameter of 15 cm and 0,5 cm height both for the conventional and microwave drying processes. The initial moisture content of the sample was determined according to the method of ASTM 3173 using 10 g of raw material to dry at 105 °C in an oven for 24 h. The determined moisture content of DS was 45%.

Experimental Setup

Microvave drying experiments were was conducted according to procedure in Çelen et all., 2015 [13]. Microwave drying of DS samples was performed with modified domestic type Beko brand microwave oven having 2450 MHz frequency (Fig. 1) and 19 liters of internal volume. During the experiments, the moisture losses were calculated from the weight measurement by precision scale (Presica XB 620 M) which was put on the microwave oven. Performed microwave power levels were selected as 120 and 700 W in this study. The drying experiments were continued until the sample mass decreased below the pre-measured sample mass with moisture content of 20%. Preliminary studies were conducted to determine this value.

Two different temperature degrees of 60 and 80 °C were chosen for conventional drying experiments. The drying experiments were continued until the moisture con-

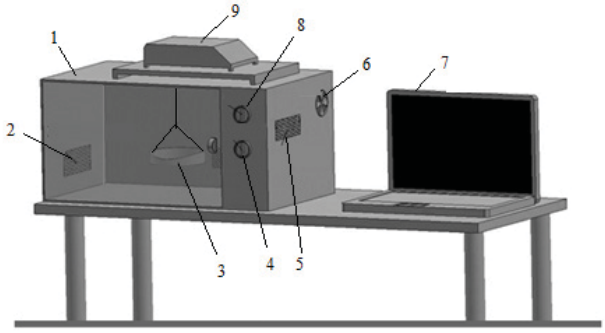

Figure 1. Microwave Drying System (1: Microwave oven, 2: Ventilation holes, 3: Tray, 4: Timer, 5: Magnetron, 6: Fan; 7: Computer, 8: Power switch, 9: Scales) The oven used in the conventional drying experiments was Kenton GX brand.

tent of the sample reached up to the same content as the microwave drying study.

Moisture content according to wet basis (Eq. 1) and dimensionless moisture ratio (Eq. 2) were calculated with the following equations:

$$\%m_{wb} = \left[M_w / \left(M_w + M_d\right)\right] \times 100 \quad (1)$$

$$m_r = \left(m - m_e\right) / \left(m_o - m_e\right) \quad (2)$$

where;
M_d: Dry mass of DS (g),
M_w: Wet mass of DS (g),
m_r: Dimensionless moisture ratio,
m: Moisture content of DS at a specific time,
m_e: Equilibrium moisture content,
m_o: Initial moisture content,
m_{wb}: Moisture content according to wet basis (g water/g wet matter).

Equilibrium moisture content in the microwave (m_e) accepted as zero [4, 13, 14].

Eq. 2 was defined as follows for the microwave drying (Eq. 3);

$$m_r = m / m_o \quad (3)$$

RESULTS AND DISCUSSION

In this study, microwave drying and conventional hot air drying were compared in the view of process efficiency. The microwave power levels of 120 and 700 W and hot air temperature degrees of 60 and 80 °C were selected to dry the drilling sludge sample. Obtained values of drying times, moisture ratio and energy consumption correlated with microwave power levels and hot air temperatures are presented in Table1. The drying experiments were continued until the equal moisture content/ratio obtained within MW drying and hot air drying process. Final moisture ratio was obtained about 20±1% for both microwave power levels and hot air temperature degrees while the initial moisture ratio was 45%.

Table 1. Obtained moisture ratio and energy consumption values

Type of heating	*Power/ Temperature*	*Time*	*Initial Sample Weight (g)*	*m_{wb}* (g water/g wet matter)*
Microwave	*700 W*	*5,5 min*	*183.367*	*0,2139*
	120 W	*48 min*	*183.842*	*0,1926*
Conventional	*60 °C*	*18 h*	*183.937*	*0,2044*
	80 °C	*12 h*	*183.184*	*0,2022*

**Calculated according to Eq-1.*

As seen from Table 1, as the MW power level was increased from 120 W to 700 W, the drying time decreased from 48 minute to 5,5 minute. The energy consumption for 700 and 120 W was 0,11 and 0,16 kW/h, respectively. According to this result, the energy consumption increased 45,45% because of the increasing drying time.

When the hot air temperature degree was increased from 60 °C to 80 °C, the drying time decreased from 18 h to 12 h which indicated about 33% decrease in the drying time. According to Fig. 2, energy consumption for 60 °C and 80 °C was determined as 0,9 and 0,99 kW/h, respectively. Accordingly, it is found that the energy consumption increased about 9,1%.

When comparing the energy consumption of the microwave and conventional drying applications for the same moisture content, the conventional drying process, was resulted in 84% more energy consumption based on the minimum energy consumption (700 W and 60 °C,) and 88% maximum energy consumption (120 W and 80 °C) compared to the microwave drying process.

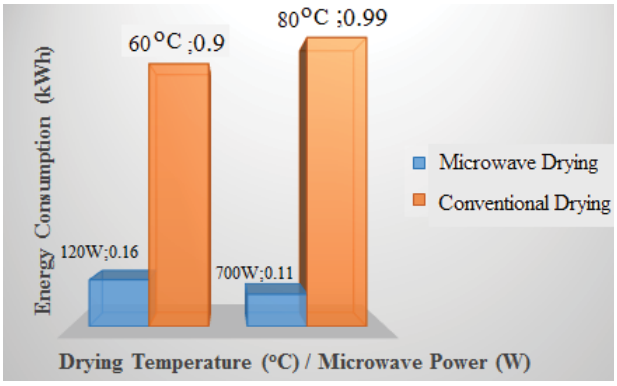

Figure 2. Energy consumption values for drying experiments

There was a significant difference among the microwave and conventional drying processes in terms of drying

time for the same moisture content of the sludge. According to Fig. 3, a linear decrease was shown in moisture ratio for microwave and conventional drying process time. The increase in drying time resulted with high energy consumption.

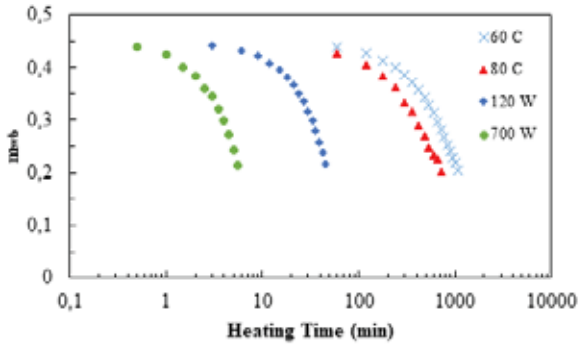

Figure 3. Drying ratio of DS at various MW power level and hot air temperature degree

As seen from Fig. 3, while there was no significant change on the drying of the sludge using the conventional heating, the microwave heating showed considerable decrease in the sludge mass, particularly at 700 W. These results clearly indicate that the microwave heating can be effectively used on the drilling mud drying following determination of the optimum parameters. Moisture content of sludge, reduced rapidly when drying time is increased. It is derived from the increase in drying temperature and microwave power. When microwave and conventional drying is compared, microwave drying has advantage on account of volume heating, drying time and energy consumption.

CONCLUSION

According to the result of the study, the drying of the drilling mud at microwave power level of 700 W seems to provide the lowest energy consumption and drying time compared to the conventional drying. It has been seen that the microwave drying of DS was much more effective than conventional drying in terms of drying time and energy consumption. It was determined that the moisture of the sludge decreased rapidly with the microwave drying which also decreased the drying time providing energy saving. Furthermore drying of DS, with reducing weight and volume, will also reduce the sludge collection, treatment, transportation, storage, and disposal costs as well as adverse environmental effects.

References

1. Jamieson E.J , Penna B., Riessen A., Nikraz H. The Development of Bayer Derived Geopolymers as Artificial Aggregates Hydrometallurgy. Hydrometallurgy 170 (2017) 74–81.
2. Tao T, Peng XF, Lee DJ. Skin Layer on Thermally Dried Sludge Cake. Dry Technology 24(8) (2006) 1047-52.
3. Zhang X.Y., Chen M.Q., Huang Y.W., Xue F. Isothermal Hot Air Drying Behavior of Municipal Sewage Sludge Briquettes Coupled With Lignite Additive. Fuel 171 (2016) 108–115.
4. Chen Z, Afzal M.T, Salema A.A. Microwave Drying Of Wastewater Sewage Sludge. Journal of Clean Energy Technologies 2 (3) (2014) 282–286.
5. Pereira, M.S.; Panisset, C.M.A.; Martins, A.L,; Sá C.H.M.; Barrozo M.A.S.; Ataíde, C.H. (2014). Microwave treatment of drilled cuttings contaminated by synthetic drilling fluid, Sep. Purif. Technol., , 124, 68–73.
6. Karaaslan S, Tunçer İK. 2009. Kırmızıbiberin fan destekli mikrodalga ile kurutulmasında kuruma karakteristiklerinin incelenmesi ve uygun kuruma modelinin belirlenmesi, KSÜ Doğa Bil. Derg., 12(2), p. 9–16. Turkish.
7. Eren Ö, Soysal Y, Öztekin S, Doğantan ZS. 2005. Mikrodalga sistemi ile donatılmış bir bantlı kurutucuda maydanoz kurutulması, III. Tarımsal Ürünleri Kurutma Tekniği Çalıştayı, 2–4 Mayıs 2005, Antalya, Turkey. Turkish..
8. Chien Y, Field Study of in situ Remediation of Petroleum Hydrocarbon Contaminated Soil on Site Using Microwave Energy. Journal of Hazardous Materials 199–200 (2012) 457–461.
9. Toreci I, Kennedy K.J, Droste R.L, Evaluation of Continous Mesophilic Anaerobic Sludge Digestion After High Temperature Microwave Pretreatment. Water Research 43 (2009) 1273–1284.
10. Shang H, Snape C.E, Kingman S.W, Robinson J.P. Microwave Treatment Of Oil–Contaminated North Sea Drill Cuttings İn A High Power Multimode Cavity. Seperation and Purification Technology 49 (2006) 84–90.
11. Robinson J.P, Kingman S.W, Onobrakpeya O. Microwave–Assisted Stripping Of Oil Contaminated Drill Cuttings, Journal of Environmental Management 88 (2008) 211–218.
12. Robinson J.P, Kingman S.W, Snape C.E, Barranco R, Shang H, Bradley M.S.A, Bradshaw S.M, Remediation Of Oil–Contaminated Drill Cuttings Using Continuous Microwave Heating, Chemical Engineering Journal 152 (2-3) (2009) 458-463.
13. Çelen S, Aktaş T, Karabeyoğlu S. S, Akyıldız A, Zeytin Pirinasının Mikrodalga Enerjisi Kullanılarak Kurutulması Ve Uygun İnce Tabaka Modelinin Belirlenmesi. Tekirdağ Ziraat Fakültesi Dergisi 12 (02) (2015).
14. Maskan M, Microwave/Air And Microwave Finish Drying Of Banana. Journal of Food Engineering 44 (2000) 71–78.

Hittite Journal of Science and Engineering, 2019, 6 (2) 123-130
ISSN NUMBER: 2148-4171
DOI: 10.17350/HJSE19030000137

Optimization of Nozzle Section in Plastic Injection Moulding Process

Baris Gurel[1], Osman Ipek[1], Yusuf Basogul[2], Ali Kecebas[3]
[1]Department of Mechanical Engineering, Suleyman Demirel University, 32200, Isparta, Turkey.
[2]Department of Mechanical Engineering, Adiyaman University, 02100, Adiyaman, Turkey,
[3]Department of Energy Systems Engineering, Mugla Sitki Kocman University, 48000, Mugla, Turkey.

ABSTRACT

In this study, the thermal analysis and numeric modelling of flow in nozzle of a real plastic injection machine with injection weight of 300 gram were conducted. The nozzle geometry was changed to optimize flow in nozzle for high-density polyethylene (HDPE) at temperature of 200 °C and injection pressure of 150 MPa. For numeric modelling, the ANSYS Fluent R14 was used. The analysis was made for four different geometries consisting of real system dimension (r-NG) and others design dimensions (NG1, NG2 and NG3). The results of the analysis showed that the most suitable flow was determined in the third (NG3) design. In this geometry, for flow in the nozzle section, rounding was made in the sudden shrinking flow section to give a throat shape and so, the geometry ensuring optimized flow was obtained. As a result, with changing of nozzle geometries of plastic injection machines having different pushing capacities they were used in the industry, the positive results will be able to be obtained.

Keywords:
Plastic injection; HDPE; Nozzle; Finite volume method, Optimization

Article History:
Received: 2018/04/10
Accepted: 2019/06/24
Online: 2019/06/30

Correspondence to: Baris Gurel;
Department of Mechanical Engineering,
Suleyman Demirel University, 32200, Isparta, Turkey
E-mail: barisgurel@sdu.edu.tr;
Phone: +902462110805;
Fax: +902462370859.

INTRODUCTION

Plastics was discovered at the end of the 19th century and developed further, especially after the Second World War. They were begun to be used in the industry and in our daily life with its thousands of varieties [1-3]. For plastic part manufacturing determined according to the physical and chemical characteristics of plastic, various manufacturing techniques have been developed (injection, extrusion, blowing, etc.). Almost 33% of plastic parts are manufactured by using injection moulding technique [4,5]. It is widely used in mechanical construction, automotive components, aerospace and aeronautical industries, and household products. Many studies have been made on manufacturing with injection moulding technique that has an extensive manufacturing capacity [6-9].

This technique enables a low cost and efficiency, fast production cadence, and high dimensional accuracy of complex plastic parts. The quality, geometrical structure, dimension tolerance, surface quality and factors affecting strength of the parts manufactured with the help of injection moulding technique have been the subject of several investigations. The dimensional change (contraction) is one of the main factors that has an effect on the quality of moulded product. It is tried to be put under control depending on the injection parameters (such as injection temperature, injection pressure, cooling period, additive material, kind of plastic raw material, crystallization rate of plastic, shape and wall thicknesses of moulded part, wall thickness change, number of inputs and distance between inputs, type of filling of mould space) [10,11]. In view of this, mould designers are using computer-based programs to optimize the injection moulding process. The factors affecting the product quality during the process have been tested and verified by many researchers in their theoretical and experimental studies [12-14] and by using various ready package programs [15,16]. Recently, Kuo and Su [17] optimized the plastic injection process with statistical methods in an experimental study by using the Taguchi technique. Shie [18] determined optimal parameters in the injection moulding process by using the artificial neural networks method. Shi et al. [19] developed a new model to

optimize the plastic injection process by using the genetic algorithm method. Lee and Lin [20] studied the runner and gating system parameters for a multi-cavity injection mould by using artificial neural networks with finite elements method. Mathivanan and Parthasarathy [21] developed an injection moulding model with mathematical and statistical techniques, by using the surface reaction methodology. Das Neogi [22] forecasted the analysing outputs of the change in dependent variables linked on the independent variables in the plastic injection process, by using the linear regression model. Zhang and Alexander [23] diagnosed the difficulties in the plastic injection process by observing the pressure signals in mould cavitation via the pressure cavity pressure signals.

The design of an injection moulded part and machining is difficult, especially the design of the feeding system, the latter which includes the sprue, the runners and the gates are more difficult. Although many principles and theories have been developed in the plastic injection modelling over past decades, there is no assurance that quality machining and a corresponding quality moulding can be manufactured. Traditionally, design of an injection moulded part and its machining is accomplished by accumulated experience. However, the ever-increasing customer demands for quality and low cost have led to the requirement of best possible quality [24].

Most defective and damaged plastic moulds are caused by incorrect design of the feeding system. Thus, most effective injection nozzle should be developed to remedy such design faults and allow plastic moulders to make better quality plastic parts with minimum investment and higher output. For this reason, Lau and Tse [25] talked about the anti-backflow, anti-leakage and pressure compensated (ABLPC) injection nozzle. They reported that the ABLPC nozzle showed a better performance compared to a standard nozzle. Yilmaz and Kirkkopru [26] modelled flow in extrusion of profiles having complicated cross-section. For analysis, they used the Bird-Carreau viscosity model in Polyflow program. Thus, they developed a method to solve the problem of unbalanced extrusion of polymer melt from mould. They determined that speed distribution at the mould outlet cross-section was consistent. Dumitrescu et al. [27] observed the flow behaviour of polymers passing from the nozzle section of 150 tones injection machine, during the plastic injection process. By using optical fibber probes with infrared spectrometer method, they optimized the polymer flow for different process features and materials. Ozdemir et al. [28] modelled the extrusion process during compounding of a polyamide material at a double-screw extruder machine, and compared the obtained results with actual results. They made the numeric modelling by using the Polyflow and Fluent software. They improved the extruder head geometrically to eliminate irregularities in flow. Sardarian et al. [29] simulated filling stage for low pressure injection moulding of aluminium by finite element method. They showed that simulation was found to correctly describe trends such as; an increase in the pressure required to fill moulds as temperature decrease. Zhuang et al. [30] developed a 3D thermal model to simulate viscoelastic polymer melt packing process in injection moulding. They showed that with an increase in melt temperature, the precise values of the first normal stress difference increased slightly, while the density decreased by stages. The high holding pressure enhanced significantly the first normal stress difference and density. Also, they reported that the present 3D thermal model was an effective tool for simulating real-world viscoelastic polymer melt packing processes. Zhang et al. [31] proposed an approach that could use the predicted errors when examining the micro-properties of typical microfluidic chips with micro injection moulding. They concluded that heat transfer coefficient showed a significant impact on filling of micro-properties. Wittemann et al. [32] provides a novel simulation method for reactive injection moulding that describes fibber-induced anisotropic flow behaviour with a fourth order viscosity tensor. Theirs study showed that cavity pressure and fibber orientations confirmed by experimental data.

Although, within the knowledge of authors, there is no study in literature that was determined about thermal and dynamic behaviours of flow in nozzle section of a plastic injection. The studies made on plastic injection process generally remain within the limits of inside of mould. If the melt material accumulated in the front of the nozzle section during the plastic injection process is propelled with pressure from side of screw, it demonstrates a flow in the nozzle section before entering in the mould. Although experimental modelling of flow in the nozzle section is technically very difficult, numeric modelling of flow in this section may be easier and give more reliable results. For removing the deficiency on this subject in the literature, using of optimization in practice will make a great contribution in the plastic injection process and in the literature.

MATERIAL AND METHODS

In this study, the referenced nozzle geometry is that of the nozzle used in the Ekin 160-B coded injection machine of 160 tones shown in Fig. 1, manufactured by the Ekin Machine Inc. Its technical features are given in Table 1. Also, this machine was used in the Industrial Thesis (SAN-TEZ) Program of the Ministry of Science, Industry and Technology in Turkey. In the study, flow in the nozzle section is optimized by using the Simple algorithm in ANSYS Fluent R14 software. The high-density polyethylene (HDPE), mostly used in manufacturing of

plastic products, are used in the study and its properties are given Table 2, at pressure of 150 MPa and temperature of 200 °C. To optimize flow in the nozzle, the most appropriate process characteristics are given in Table 3. Thus, the geometrical changes are made on the real nozzle geometry (r-NG). And then, three different geometries (NG1, NG2 and NG3) are obtained for the flow optimization. Finally, the obtained results were evaluated and compared with each other.

Figure 1. Ekin 160 – B plastic injection machine and its injection nozzle

In this study, some studies [3,27-33] are considered as a reference for solving of mathematical equations. For the finite volumes method, the balance equations such as the continuity, momentum, energy and Bird-Carreau viscosity model are solved numerically in the ANSYS Fluent R14 software, as given the following:

Continuity equation

$$\nabla \cdot u = 0 \tag{1}$$

Momentum equation

$$\rho \frac{\partial u}{\partial t} - \nabla \cdot \eta \left(\nabla u + \left(\nabla u \right)^T \right) + \rho u \cdot \nabla u + \nabla P = 0 \tag{2}$$

Energy equation

$$\rho C_P \frac{\partial T}{\partial t} = \frac{\partial P}{\partial t} + k \nabla^2 T + \eta \Phi \tag{3}$$

Bird-Carreau viscosity model

$$\eta = \eta_\infty + \left(\eta_0 - \eta_\infty \right) \left[1 + \left(\lambda \dot{\gamma} \right)^2 \right]^{\frac{(n-1)}{2}} \tag{4}$$

where $\dot{\gamma}$ denotes a scalar quantity and can be calculated using components of the strain rate tensor, as follow:

$$\dot{\gamma} = \sqrt{I_2 / 2} \tag{5}$$

where I_2 is the second invariant of the strain rate tensor as

$$I_2 = \sum_i \sum_j \dot{\gamma}_{ij} \dot{\gamma}_{ji} = \dot{\gamma}_{xx}^2 + \dot{\gamma}_{xy}^2 + \dot{\gamma}_{xz}^2 + \dot{\gamma}_{yx}^2 + \dot{\gamma}_{yy}^2 + \dot{\gamma}_{yz}^2 + \dot{\gamma}_{zx}^2 + \dot{\gamma}_{zy}^2 + \dot{\gamma}_{zz}^2 \tag{6}$$

The Bird-Carreau viscosity model was used in solving of viscosity equation because of the fact that gives more accurate and reliable result in modelling of polymer flows [3,28]. For discretization of these equations, the Simple Algorithm is used for the ANSYS Fluent R14 software.

Table 1. Technical properties of the Ekin 160 – B plastic injection machine

Properties	Value
Screw diameter (mm)	45
Screw L/D ratio	21
Shot size (cm^3)	332
Injection weight (g)	300
Injection rate (g/s)	118
Plasticizing capacity (g/s)	22
Injection pressure (MPa)	150
Screw speed (rpm)	0-230
Screw stroke (mm)	210
Clamping force (kN)	1600
Toggle stroke (mm)	385
Space between tie bars (mm)	410x410
Max mould height (mm)	450
Min mould height (mm)	100
Ejector stroke (mm)	120
Ejector force (kN)	35
Ejector number (PC)	1
Heater power (kW)	8.5
Machine dimensions (m)	5.4 x1.2 x1.8
Machine weight (T)	4

Table 2. Properties of high-density polyethylene (HDPE) at 200 °C

Properties	Value
Zero shear viscosity, μ_o (Pa.s)	5255
Infinity shear viscosity, μ_∞ (Pa.s)	0
Material density, ρ (kg/m3)	951
Natural time, λ(s)	0.96
Power-law index, n	0.496
Material melting temperature, T_{melt} (°C)	176 (440 K)

Table 3. Properties of the analysis process

Properties	Value
Inlet pressure, Pin (MPa)	150
Inlet temperature, Tin (°C)	200 (473 K)
Nozzle material	Steel
Nozzle wall	Adiabatic wall

RESULTS AND DISCUSSION

The purpose of this study is to make the optimization of nozzle section in plastic injection machine. In this process, cavitation that occur as a result of high pressure fluctuations cause sudden change in speed and temperature of injection process and thus phase of material changes. The change of phase causes porosity and gives da-

mage to the material structure in the mould. To increase the moulded material quality and improve the process, the nozzle geometry should be enhanced. In this study, flow in nozzle is optimized by the ANSYS Fluent R14 software considering to the features of plastic injection machine, properties of high-density polyethylene (HDPE) and conditions of injection process given in Tables 1-3 on the basis of original/real nozzle geometry of which solid model picture is given in Fig. 1. The original/real nozzle geometry (r-NG) and the developed design geometries (NG1, NG2 and NG3) are illustrated in Fig. 2.

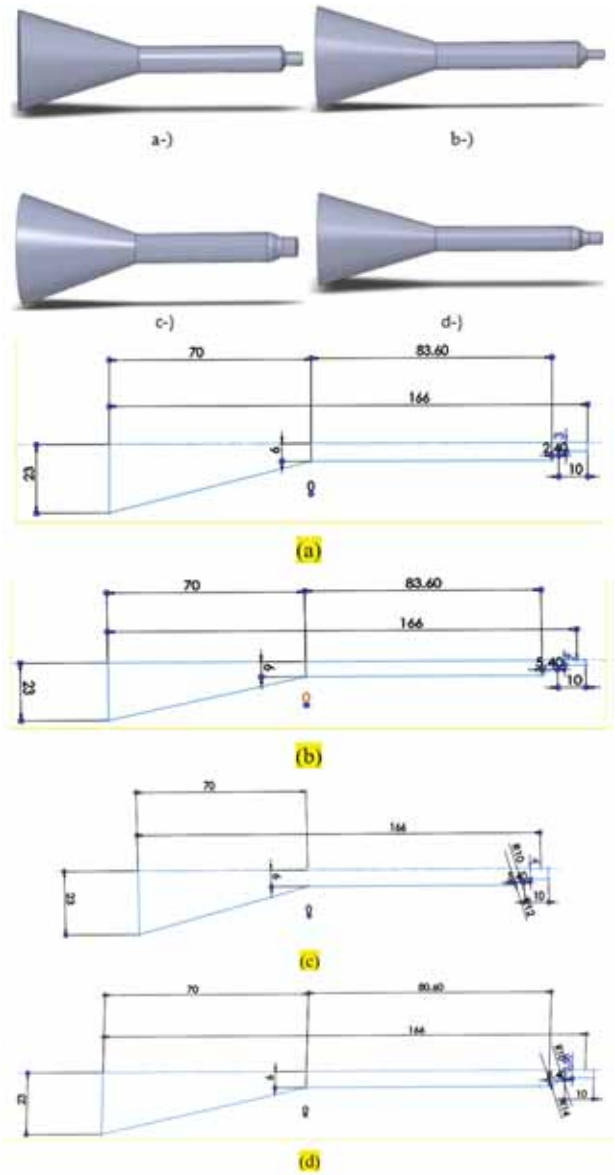

Figure 2. The solid modelling and measurement of (a) the real nozzle geometry (r-NG), (b) the first (NG1), (c) the second (NG2) and (d) the third (NG3) nozzle geometry designs.

The pressure and temperature contour distributions for the real nozzle geometry (r-NG) with its boundary conditions (see Fig. 2(a)) are shown in Fig. 3. As can be seen in Fig. 3(a), vacuum occurs in the sudden shrinking region of nozzle and pressure drops in this section. Then, when the fluid moves away from the sudden shrinking section, static pressure of the fluid (HDPE) increases again. And the fluid at exit of nozzle leaves the nozzle with about pressure of 7 MPa. From Fig. 3(b), in the sudden shrinking section where temperature increase occurs because of the viscosity of melting plastic fluid at nozzle walls, the temperature of plastic fluid in axis and throughout the nozzle falls below the melting temperature of the plastic material. Thus material solidification occurs. The temperature of the HDPE in the solidification section decreases to 52 °C (325 K). In the r-NG, the solidification process at the end of the nozzle occurs while the fluid passes from the nozzle section, as seen in Fig. 3(b) for blue colour sections. For optimizing of the r-NG, the second design (NG1) is obtained by extending the length of sudden narrowing section from 2.40 mm to 5.40 mm and reducing the exit diameter of the sudden narrowing section from 3 mm to 2 mm on the real nozzle geometry, as illustrated in Fig. 2(b).

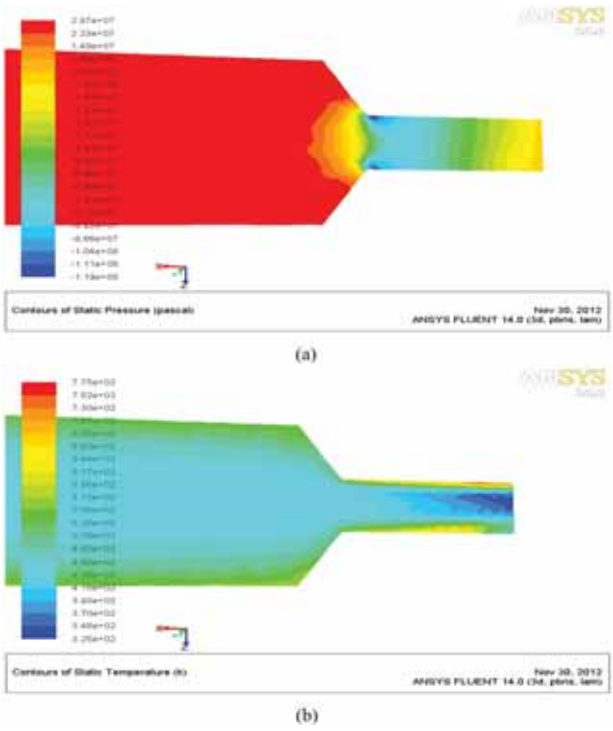

Figure 3. The distributions of pressure (a) and temperature (b) in nozzle section for the r-NG

The results of the analysis performed for the NG1 are presented in Fig. 4. In Fig. 4(a) for the pressure distribution, it is seen that vacuum occurs in the sudden shrinking section. This causes cavitation. As can be seen in Fig. 4(b), the temperature in middle of cross-section throughout the nozzle did not fall below 180 °C (453 K) while the temperature distribution throughout nozzle walls increases to 554 °C (827 K) because of the viscous dissipation. With a more stable increase in fluid velocity, there is no solidification zone in the flow of the HDPE material for the NG1 due to no sudden drop in temperature. However, the sections with temperature of 180 °C (453 K) tend to be close to solidification temperature. This is not a desirable result.

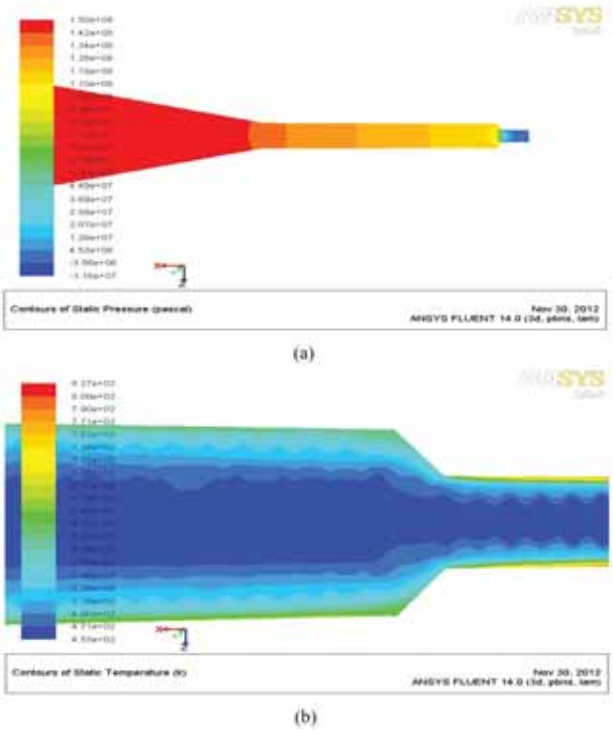

Figure 4. The distributions of pressure (a) and temperature (b) in nozzle section for the NG1.

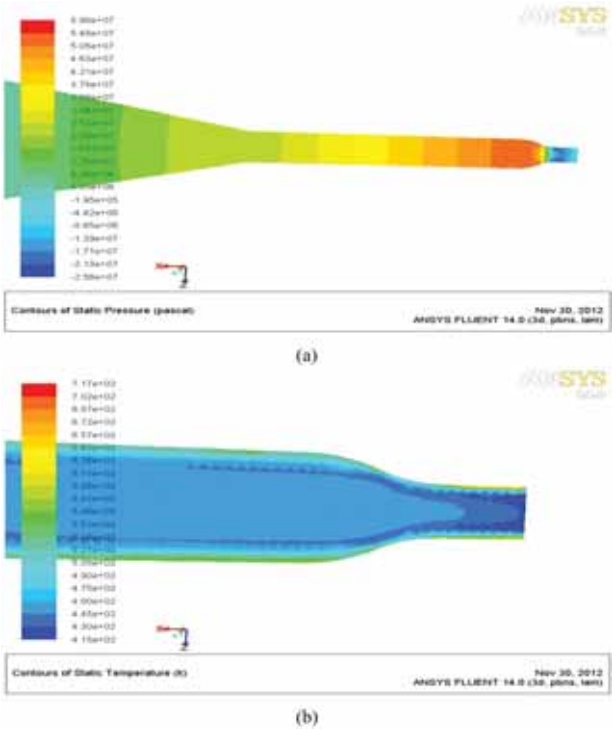

Figure 5. The distributions of pressure (a) and temperature (b) in nozzle section for the NG2.

To find a design in which the lowest temperature in the nozzle section will be higher than 440 K, design of the NG1 is changed. Thus, the second design (NG2) is considered as illustrated in Fig. 2(c). For more stable flow at nozzle, by rounding sudden shrinking section of 10 mm and increasing the exit diameter of the sudden shrinking section from 2 mm to 4 mm in the NG1, the NG2 geometry is obtained. Fig. 5 shows the results of analysis for the NG2. In Fig. 5(a), it is observed that cavitation occurs at the tip of nozzle because of sudden pressure fluctuations in the pressure distribution counters in the nozzle section. With sudden increase in fluid velocity, phase change in the HDPE material is occurred. Regard in Fig. 5 (b), it can be seen that the temperature of fluid in the middle cross-section decreases to 142 °C (415 K) while the temperature at the side walls of nozzle increases to 444 °C (717 K), because of the viscous heating in flow of the nozzle section. In here the solidification formation is observed as the temperature of fluid in the middle cross-section of nozzle tip fell below the melting temperature of 167 °C (440 K). Because of solidification condition, the nozzle in the NG2 becomes unusable. For this reason, the third design (NG3) is passed, as illustrated in Fig. 2(d).

In the NG3, the nozzle outlet diameter is conducted as 3.50 mm, and nozzle outlet is rounded to diameter of 14. The results of analysis for the NG3 are shown in Fig. 6. For the pressure distribution counters, it can be seen from Fig. 6(a) that vacuum occurs in the sudden shrinking section of nozzle tip. During flow of the HDPE material in the nozzle section, the temperature in the middle cross-section is higher value compared to nozzle section in the original (r-NG) and the others (NG1 and NG2) designs, while the temperature distribution increases to 459 °C (732 K) at wall sections of nozzle tip (see Fig. 6(b)). In the NG3, the temperature in the middle cross-section of nozzle decreases to 200 °C (473 K).

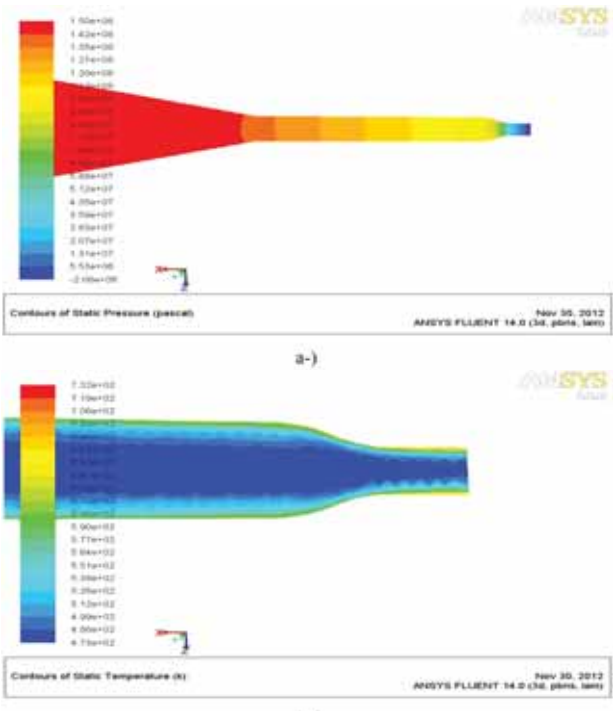

Figure 6. The distributions of pressure (a) and temperature (b) in nozzle section for the NG3.

In the optimization work, due to solidification in nozzle section of the original/real (r-NG) and second (NG2)

designs, these type nozzles are not recommended to use in the plastic injection process. As a result, the first (NG1) and third (NG3) designs can be used in the plastic injection process. For the NG1 and the NG3 designs, the more stable flow in the nozzle section can also be investigated. The Reynolds number distribution for each design is shown in Fig. 7. Note that the temperature at nozzle tip of the NG3 decreases to 200 °C (473 K) while that of the NG1 decreases to 184 °C (457 K). In addition, it can be understood that the maximum Reynolds number in flow of nozzle section in the NG1 increase to 12.5 while that in the NG3 increases to 8.08, as shown in Figs. 7(a) and 7(b), respectively.

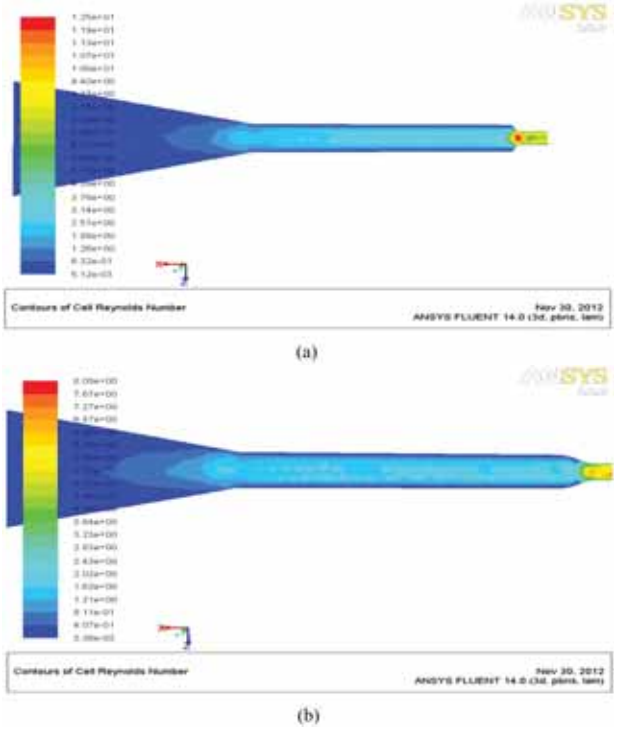

Figure 7. The distributions of the Reynolds number in nozzle section for the NG1 and NG3 nozzle geometries.

Optimizing criterion of flow is summarized that: (i) Reynolds number distribution in the flow section must be lower (namely, laminar flow), (ii) the lowest value of temperature at nozzle exit must be higher. According to the determined criterion, the nozzle geometry in the NG3 is optimum nozzle geometry.

CONCLUSION

In this study, the nozzle section of the Ekin 160-B coded plastic injection machine with 160 tones is numerically investigated for the thermal analysis of the HDPE material flow. First, the original/real nozzle geometry (r-NG) is analysed by ANSYS Fluent R14 software. The others nozzle geometries (NG1, NG2 and NG3) are then optimized by changing the r-NG. According to the analyses, the r-NG and NG2 are not convenient as there will be solidification in the flow of nozzle section in plastic injection machine. For the NG1 and NG3, no solidification occurs in flow of nozzle section of the plastic material. Additionally, in the NG3 the Reynolds number change is smaller value while the temperature in nozzle output is 200 °C (473 K). However, in the NG1, the Reynolds number change is higher value as the temperature of HDPE material is 184 °C (457 K). The temperature of flow in nozzle output should not be near to melting temperature (167 °C = 440 K) of HDPE material. This is the most ideal situation. In other words, the nozzle geometry in the NG3 is the most optimum geometry. Porosity formation during flow will be very less and thus the material quality in mould will be the highest. Rounding of narrowing cross-section geometry in the sudden narrowing flow sections during the plastic injection process prevents porosities that occur in the flow and ensures the flow to be more perfect. Extensive usage of nozzle designs in the industrial applications to be made by considering the nozzle geometry established as a result of geometrical improvements will create an important economic advantage for the plastic injection process that is one of the widely used manufacturing methods. In future studies to be realized by taking this study as a basis, the improvements will be made in the nozzle section of different capacity machines for plastic injection process, very important advantage in cost of plastic injection process will be obtained and besides, and optimization of this process will be able to be realized.

ACKNOWLEDGEMENTS

The authors wish to thank Mechanical Engineering Department of Suleyman Demirel University for their constant interest and valuable advice in this project. This work was partially supported by the Industrial Thesis (SAN-TEZ) Program of the Ministry of Science, Industry and Technology in Turkey through a research Grant No. 00012.STZ.2006-1.

NOMENCLATURE

C_p	specific heat capacity (kJ/kgK)
I	invariant of strain rate tensor
k	heat transfer coefficient (W/mK)
L	length (m)
n	flow behaviour exponent /power-law (-)
P	pressure (Pa)
Re	Reynold number (-)
t	time (s)
T	temperature (°C or K)
u	velocity (m/s)

Greek symbols

γ	scalar quantity
ρ	fluid density (kg/m3)

η_0	zero stress viscosity (kg/ms)
η_∞	infinity shear stress viscosity (kg/ms)
λ	time constant (s)
∇	nabla

Subscripts

in	input
out	output
x, y, z	coordinate

Abbreviations

ABLPC	anti-backflow, anti-leakage and pressure compensated
D	dimension
HDPE	high-density polyethylene
NG	nozzle geometry

References

1. Bird RB, Stewart WE, Lightfoot EN. Transport Phenomena. John Wiley and Sons, New York, USA, 1960.
2. Guldas A. Mathematical modelling and experimental investigation of the flow molten plastic in injection moulding. Ph.D. Dissertation, Gazi University, Ankara, Turkey, 2004.
3. Uluer O. Numerical analysis and experimental investigation of three dimensional polymer melt flows in injection moulding. Ph.D. Dissertation, Gazi University, Ankara, Turkey, 2009.
4. Del Coz Diaz JJ, Garcia Nieto PJ, Ordieres Mere J, Bello Garcia A. Computer simulation of the laminar nozzle flow of a non–Newtonian fluid in a rubber extrusion process by the finite volume method and experimental comparison. Journal of Non–Crystalline Solids 353 (2007) 981–3.
5. Gava A, Lucchetta G. Numerical simulation of PA66 numerical flow behavior in a hot runner gate. Macromollecular Symposia 263 (2008) 53–66.
6. Hieber CA, Shen SF. A finite element/finite difference simulation of the injection–moulding filling process. Journal of Non–Newton Fluid Mechanics 7 (1980) 1–32.
7. Seow LW, Lam YC. Optimizing flow in plastic injection moulding. Journal of Materials Processing Technology 72 (1997) 333–41.
8. Mok SL, Kwong CK. Review of research in the determination of process parameters for plastic injection moulding. Advances in Polymer Technology 18 (1999) 225-36.
9. Jiang B, Zhong J, Huang B, Ui X, Li Y. Element modelling of FEM on the pressure field in the powder injection mould filling process. Journal of Materials Processing Technology 137 (2003) 74–7.
10. Tadmor Z, Gogos CG. Principles of Polymer Processing, Wiley, New York, USA, 1979.
11. Sasmal GP. A finite volume approach for calculation of viscoelastic flow through an abrupt axisymetric contraction. Journal of Non–Newton Fluid Mechanics 56 (1995) 15–47.
12. Oktem H, Erzurumlu T, Uzman I. Application of Taguchi optimization technique in determining plastic injection moulding process parameters for a thin–shell part. Materials and Design 28 (2007) 1271–8.
13. Chen WC, Fu GL, Tai PH, Deng WJ. Process parameter optimization for MIMO plastic injection moulding via soft computing. Expert Systems with Applications 36 (2009) 1114–22.
14. Kurt M, Kamber OS, Kaynak Y, Atakok G, Girit O. Experimental investigation of plastic injection moulding: Assessment of the effects of cavity pressure and mould temperature on the quality of the final products. Materials and Design 30 (2009) 3217–24.
15. Chen CP, Chuang MT, Hsiao YH, Yang YK, Tsai CH. Simulation and experimental study in determining injection moulding process parameters fort thin–shell plastic parts via design of experiments analysis. Expert Systems with Applications 36 (2009) 10752–9.
16. Kumar A, Ghoshdastidar PS, Muju MK. Computer simulation of transport process during injection mould–filling and optimization of the moulding conditions. Journal of Materials Processing Technology 120 (2002) 438–49.
17. Kuo FCJ, Su TL. Optimization of multiple quality characteristics for polyether ether ketone injection moulding process. Fibers and Polymers 7 (2006) 404–13.
18. Shie JR. Optimization of injection moulding process for contour distortions of polypropylene composite components by a radial basis neural network. International Journal of Advanced Manufacturing Technology 36 (2008) 1091–103.
19. Shi F, Lou ZL, Lu JG, Zhang YQ. Optimization of plastic injection moulding process with soft computing operations. International Journal of Advanced Manufacturing Technology 21 (2003) 656–61.
20. Lee KS, Lin JC. Design of the runner and gating system parameters for a multi–cavity injection mould using FEM and neural network. International Journal of Advanced Manufacturing Technology 27 (2006) 1089–96.
21. Mathivanan D, Parthasarathy NS. Prediction of sink depths using nonlinear modeling of injection moulding variables. International Journal of Advanced Manufacturing Technology 43 (2009) 654–63.
22. Das Neogi P. Comparing the predictive ability of T–method and linear regression method. In: Proceedings of the Industrial Engineering Research Conference, Miami, USA, 2009.
23. Zhang J, Alexander SM. Fault diagnosis in injection moulding via cavity pressure signals. International Journal of Production Research 46 (2008) 6499–512.
24. Barbosa RCN, Campilho RDSG, Silva FJG. Injection mold design for a plastic component with blowing agent. Procedia Manufacturing 17 (2018) 774–782.
25. Lau KH, Tse TTM. Enhancement of plastic injection moulding quality through the use of the ABLPC nozzle. Journal of Materials Processing Technology 69 (1997) 55–57.
26. Yilmaz O, Kirkkopru K. Template to a method for providing a balanced material output from mould in profile extrusion. In: The fourth Ege Energy Symposium, Izmir, Turkey, 2008.
27. Dumitrescu OR, Baker DC, Foster GM, Evans KE. Near infrared spectroscopy for in–line monitoring during injection moulding. Polymer Testing 24 (2005) 367–75.
28. Ozdemir K, Kocak C, Cakır MK. Material flow modeling on output head of twin screw extruder for polyamide compound material in extrusion process, In: The sixth Automotive Technologies Congress, Bursa, Turkey, 2012.
29. Sardarian M, Mirzaee O, Habibolazadeh A. Mould filling simulation of low pressure injection moulding (LPIM) of alumina: Effect of temperature and pressure. Ceramics International 43 (2017) 28–34.

30. Zhuang X, Ouyang J, Li Y, Jiang C, Wang L. A three–dimensional thermal model for viscoelastic polymer melt packing process in injection moulding. Applied Thermal Engineering 128 (2018) 1391–403.
31. Zhang H, Fang F, Gilchrist MD, Zhang N. Precision replication of micro features using micro injection moulding: Process simulation and validation. Materials and Design 177 (2019) 107829.
32. Wittemann F, Maertens R, Karger L, Henning F. Injection molding simulation of short fiber reinforced thermosets with anisotropic and non–Newtonian flow behavior. Composites Part A: Applied Science and Manufacturing 124 (2019) 105476.
33. Versteeg HK, Malalasekera W. An Introduction to Computational Fluid Dynamics the Finite Volume Method, Prentice Hall, New Jersey, USA, 2007.

Hittite Journal of Science and Engineering, 2019, 6 (2) 131-136
ISSN NUMBER: 2148-4171
DOI: 10.17350/HJSE19030000138

Taxonomic Status of Water Vole, (Arvicola Amphibius Linneaus, 1758) in Western Anatolia

Bulent Gozcelioglu[1], Zeycan Helvaci[2] Ercument Colak[3]
[1]The Scientific and Technological Research Council of Turkey (TÜBİTAK), Turkey
[2]Department of Biology, Faculty of Science and Letter, Aksaray University, Aksaray, Turkey
[3]Department of Biology, Faculty of Science, Ankara University, Ankara, Turkey

ABSTRACT

A total of 116 specimens of the genus Arvicola were collected from western part of Turkey (Western part of Anatolia and Turkish Thrace) and examined based on geometric morphometrics and traditional morphometrics. Morphometrical analyses showed that A. amphibius populations in western part of Turkey are highly differentiated as Anatolian and Thrace populations. Depend on morphometrical differentiation, we conclude that these two populations, classified within two subspecies; Arvicola amphibius persicus and Arvicola amphibius cerncavskii respectively.

Article History:
Received: 2019/03/16
Accepted: 2019/06/27
Online: 2019/06/30

Correspondence to:Bülent Gözcelioğlu,
The Scientific and Technological Council of Turkey, TURKEY
E-Mail: bulent.gozcelioglu@tubitak.gov.tr

Keywords:
Arvicola; Geometric morphometrics; Morphology; Thrace; Anatolia; Taxonomy.

INTRODUCTION

Over the last few decades, many studies have done to clarify the taxonomy of water voles (genus Arvicola Lacépede, 1799). Recent studies showed that water voles divided into three species; A. sapidus (Miller, 1908) , A. amphibius (Linnaeus, 1758) (formerly known as A. terrestris) and A. scherman (Musser and Carleton, 2005). The first records of water vole (A. amphibious) from the Turkey reported by Steiner and Vauk (1966) around Lake Beyşehir.

Depend on morphological and biometrical features, three water vole subspecies identified in Turkey; Arvicola amphibius persicus (Anatolia), Arvicola amphibius hintoni (Southeastern Anatolia Region), Arvicola amphibius cernjavskii (Thrace) (Mursaloğlu, 1975). amphibius comprises two ecological types which are aquatic and fossorial forms, each with different living habits and these ecotypes are often morphologically distinct (Meylan, 1977). And also recent studies lowerline that, water voles are characterized by an extraordinary morphological and ecological plasticity (Castiglia et al., 2016). Basically, geometric morphometrics allow to compare morphological objects by their shapes which can be described as the study of biological shapes. Traditional morphometrics has been quite a useful means in morphometrics for long years (Zelditch et al., 2004). Also, it has the most common use in morphometrics, and it is based on direct measurements and then comparison.

Therefore, usage of morphological methods may highly informative to obtain taxonomical situation of water vole that distributed in western part of Anatolia. Moreover, a biogeographic comparison allows the identification of the specific morphological response of water vole to the different environments.

In addition to that, our findings may be enlightening for further studies on population genetics and evolution of water vole because of the study area's biogeographic importance for Europe and Middle East. Furthermore, climate change and drying of inland water highly effect on genetic structure of this species therefore water vole populations can be a good model to investigate and contribute to those current problems.

Consequently, this study aimed to identify the patterns of morphological differentiations to better lowerstanding of taxonomy of water vole subspecies along the Turkish Thrace and Western part of Anatolia.

Figure 1. Localization of the sampling localities of water vole considered in the present study (1. Kırklareli , 2. Denizli, 3. Uşak, 4. Eskişehir, 5. Bolu, 6. Eber Gölü (*Çay*, Afyon), 7. Beyşehir (Konya) 8. Ankara, 9. Kırşehir)

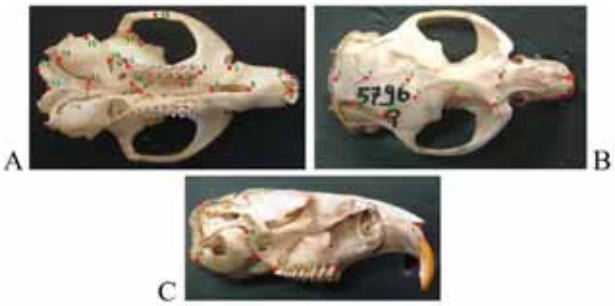

Figure 2. Landmarks used to capture skull shape on the water vole; Dorsal (A), ventral (B), lateral (C)

MATERIALS AND METHODS

Water voles were collected from 9 localities Western part of Anatolia between 2004-2007 (Fig. 1). Skulls of 85 adult individuals of two subspecies were examined.

Thrace samples were collected from Kırklareli at around 41° 67' N and 27° 07' E associated with temperate conditions. Anatolian samples were collected from western part of Anatolia vary at 40° 81' N and 32° 83' E and 38° 53' N and 28° 64' E (Table 1).

The skull images were taken with Leica MZ 16 stereomicroscope. Photographs were first input to TpsUtil1.34 and then 2D coordinates of each landmark were digitized using the Tps-Dig1.40 (Rohlf, 2004). The landmark configurations were superimposed to the same reference form by generalized least squares (Rohlf, 1999) in Morpheus (Slice, 2002).

Geometric morphometric data consisted of four sets; one referring to 11 landmarks on the dorsal side (Fig. 2A), 18 landmarks on the ventral side (Fig. 2B) and the other to 8 landmarks on the lateral side of the skull (Fig. 2C).

Depend on their close geographic position, some localities are combined and then 6 group defined; trak (Thrace), beys (Beyşehir), deus (Denizli-Uşak), abes (Ankara-Bolu-Eskişehir), kirs (Kırşehir), eber (Eber) (Table 2.).

4 external and 35 internal characters are measured. Table 2 shows that average measurements of morphometrical characters, minimum, maximum and standard deviations of Anatolian populations of Arvicola terrestris persicus(Table 3).

4 external and 35 internal morphometric characters are measured. Table 2 shows that average measurements of morphometrical characters, minimum, maximum and standard deviations of Thrace populations of Arvicola terrestris cernjavskii.

All statistical analyses to identify shape variations of water voles were performed using the SPSS 13.0 (SPSS, 2004).

Table 1. Trapping localities of water vole with per coordinates

Species	*Locality*	*Latitude*	*Longitude*
Arvicola terrestris persicus	*Kırşehir – Stream Kılıçözü*	*39.130926*	*34.151859*
Arvicola terrestris persicus	*Kırşehir – 12 km*	*39.167069*	*34.145164*
Arvicola terrestris persicus	*Kırşehir – 10 km*	*39.165871*	*34.145508*
Arvicola terrestris persicus	*Lake Seyfe*	*39.199802*	*34.418106*
Arvicola terrestris persicus	*Ankara –Ayaş*	*40.086379*	*32.118230*
Arvicola terrestris persicus	*Bolu –Yeniçağa*	*40.773327*	*32.030725*
Arvicola terrestris persicus	*Bolu –Eskiçağa*	*40.819168*	*32.036862*
Arvicola terrestris persicus	*Kahramanmaraş –Göksun*	*38.018886*	*36.486969*
Arvicola terrestris persicus	*Afyon – Lake Eber*	*38.668411*	*31.177356*
Arvicola terrestris persicus	*Konya –Beyşehir*	*37.682450*	*31.747616*
Arvicola terrestris persicus	*Denizli – Çivril*	*38.301485*	*29.741691*
Arvicola terrestris persicus	*Denizli – Çivril Yuvaköy*	*38.301485*	*29.741691*
Arvicola terrestris persicus	*Uşak – Kula*	*38.542283*	*28.651150*
Arvicola terrestris persicus	*Uşak – Yenişehir*	*38.676711*	*29.033657*
Arvicola terrestris persicus	*Eskişehir – Gülçayır*	*39.248721*	*31.399511*
Arvicola terrestris cerjavskii	*Kırklareli – İnece*	*41.704660*	*27.063521*

Table 2. External and internal lineer measurement characters of *Arvicola terrestris persicus*

	Measurements Characters	N	avg.	Min.	Max.	SS (+/-)
1.	Total lenght	79	305,20	213,00	378,00	34,23
2.	Tail	79	125,96	81,00	152,00	14,39
3.	Hind leg	79	36,78	27,00	42,00	2,47
4.	Ear length	79	16,88	9,00	21,00	2,62
5.	Weight	79	142,14	59,00	237,00	38,09
6.	Zygomatic width	79	23,05	19,35	25,94	1,62
7.	Least breadth of skull	79	4,85	3,96	6,10	0,37
8.	Condylobasale length	79	37,63	31,26	41,48	2,34
9.	Condylobasale length	79	39,86	33,59	43,80	2,31
10.	Occipitonasale length	79	38,11	19,55	42,71	3,67
11.	Basale length	79	36,39	29,26	40,17	2,14
12.	Nasal length	79	10,92	8,72	12,70	0,98
13.	Nasal width	79	4,77	3,65	6,99	0,64
14.	Perietal suture uzunluğu	79	7,96	6,16	9,04	0,56
15.	Face area lenght	79	24,02	10,16	34,01	2,49
16.	Brain area lenght	79	15,47	11,09	17,43	1,12
17.	Mastoid width	79	11,00	9,11	12,48	0,70
18.	Bulla tympanica length	79	13,10	11,61	14,80	0,68
19.	Bulla tympanica width	79	11,88	9,82	70,93	6,81
20.	Occipitale width	79	15,65	12,42	17,48	1,06
21.	Brain capsule width	79	14,57	12,60	15,65	0,59
22.	Diestama lenght	79	13,19	10,34	15,54	1,12
23.	Palatal lenght	79	21,69	17,91	24,09	1,47
24.	Insisiva length	79	6,68	4,46	9,76	0,74
25.	Bulla tympanica length	79	9,88	7,66	11,17	0,54
26.	Bulla tympanica width	79	7,04	6,12	8,36	0,35
27.	Mandibulae length	79	26,29	22,21	29,15	1,64
28.	Mandibulae height	79	6,45	5,16	8,84	0,57
29.	Upper molar alveoli length	79	9,13	7,72	10,44	0,62
30.	Upper molar length	79	10,13	9,02	11,90	0,61
31.	Length of lower teeth alveoli	79	9,24	7,82	10,55	0,64
32.	Lower molar length	79	9,98	8,54	11,68	0,58
33.	Coronoid prossess height	79	13,99	11,45	16,09	1,05
34.	First upper molar length M1	79	8,59	7,63	10,26	0,62
35.	Second upper molar length M2	79	6,25	5,00	7,36	0,55
36.	Third upper molar length M3	79	6,22	3,16	7,63	0,68
37.	First lower molar length M1	79	9,26	7,63	11,05	0,73
38.	Second lower molar length M2	79	6,00	5,00	8,94	0,59
39.	Third lower molar length M3	79	5,95	4,73	8,94	0,63

N: number of sample, avg: avarage, min: minimum, max: maksimum, SS: Standart deviation

Table 3. External and internal lineer measurement characters of *Arvicola terrestris cernjavskii*

	Measurements Characters	N	avg.	Min.	Max.	SS (+/-)
1.	Total lenght	6	314,67	297,00	340,00	16,79
2.	Tail	6	121,17	104,00	130,00	9,43
3.	Hind leg	6	34,50	33,00	36,00	1,05
4.	Ear length	6	17,17	14,00	19,00	1,83
5.	Weight	6	173,50	152,00	193,00	16,28
6.	Zygomatic width	6	23,45	22,95	24,54	0,68
7.	Least breadth of skull	6	4,77	4,52	5,04	0,17
8.	Condylobasale length	6	37,81	36,15	39,76	1,51
9.	Condylobasale length	6	39,73	38,27	42,06	1,61
10.	Occipitonasale length	6	38,83	37,41	41,45	1,67
11.	Basale length	6	32,59	17,65	37,91	8,41
12.	Nasal length	6	10,55	10,08	10,82	0,35
13.	Nasal width	6	4,51	4,11	5,07	0,40
14.	Perietal suture uzunluğu	6	7,97	7,07	8,88	0,69
15.	Face area lenght	6	24,28	23,34	26,28	1,17
16.	Brain area lenght	6	15,60	15,06	16,14	0,52
17.	Mastoid width	6	11,71	11,11	12,20	0,45
18.	Bulla tympanica length	6	12,69	12,08	13,12	0,40
19.	Bulla tympanica width	6	11,08	10,72	11,36	0,26
20.	Occipitale width	6	15,77	15,18	16,47	0,60
21.	Brain capsule width	6	14,80	14,44	15,42	0,41
22.	Diestama lenght	6	13,23	12,08	14,35	0,92
23.	Palatal lenght	6	21,65	20,29	23,73	1,23
24.	İnsisiva length	6	6,51	5,81	7,01	0,47
25.	Bulla tympanica length	6	9,78	9,16	10,62	0,53
26.	Bulla tympanica width	6	7,02	6,90	7,12	0,10
27.	Mandibulae length	6	26,42	24,76	28,00	1,14
28.	Mandibulae height	6	6,46	6,22	6,63	0,14
29.	Upper molar alveoli length	6	9,07	8,71	9,55	0,37
30.	Upper molar length		10,11	9,56	10,81	0,47
31.	Length of lower teeth alveoli	6	9,26	8,92	9,94	0,40
32.	Lower molar length		10,16	9,61	10,93	0,61
33.	Coronoid prossess height		13,27	11,86	14,22	0,93
34.	First upper molar length M1	6	8,77	8,15	9,47	0,52
35.	Second upper molar length M2	6	6,49	6,31	6,84	0,21
36.	Third upper molar length M3	6	6,00	5,79	6,05	0,12
37.	First lower molar length M1	6	8,90	8,15	10,52	0,92
38.	Second lower molar length M2	6	5,74	5,26	6,31	0,39
39.	Third lower molar length M3	6	5,84	5,52	6,31	0,43

N: number of sample, avg: avarage, min: minimum, max: maksimum, SS: Standart deviation

RESULTS

Based on shape analysis of dorsal view of water vole UPGMA dendogram (Fig.3A) we find no significant differentiation basis for Turkish Thrace and Western part of Anatolia populations.

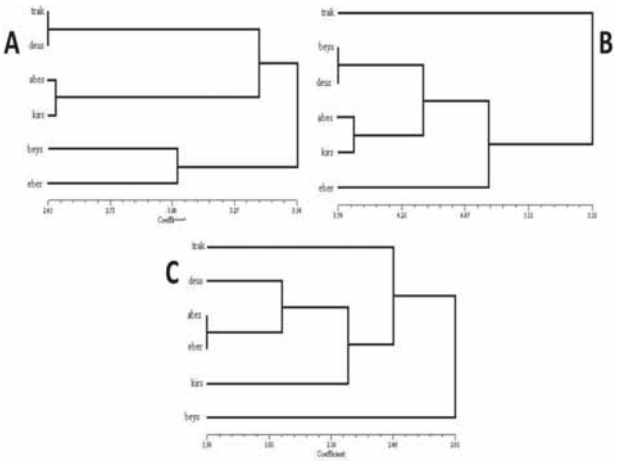

Figure 3. Dorsal (A), ventral (B) and lateral (C) differentiation between localities based on UPGMA by using landmark geometric morphometric (Groups; trak: Thrace, beys: Beyşehir, deus: Denizli-Uşak, abes: Ankara-Bolu-Eskişehir, kirs: Kırşehir, eber: Eber)

Our UPGMA dendogram results indicate clear confirmation of the subspecies-level status of Arvicola amphibius persicus (Anatolia) and Arvicola amphibius cernjavskii (Thrace) depend on ventral and lateral view of water vole skull (Fig. 3B, C). Fig. 3C also indicates that Beysehir population is different from all other populations, and Thrace population is much closer to the other populations. Comparing to Arvicola terrestris subspecies populations; tail, ear, condilobasale lenght, basale lenght, nasal lenght, parietal sutur lenght, mastoid, width, diestama lenght, damak lenght, bulla tympanica lenght, bulla tympanica width, mandibul lenght, Mandibulae height, under molar alveoli length, under molar length, coronoid prossess height, under M2, under M3 ve upper M2 measurements are quite different within 2 subspecies.

Comprasion of Arvicola terrestris populations depend on measurements of external and internal characters shown on Fig. 4.

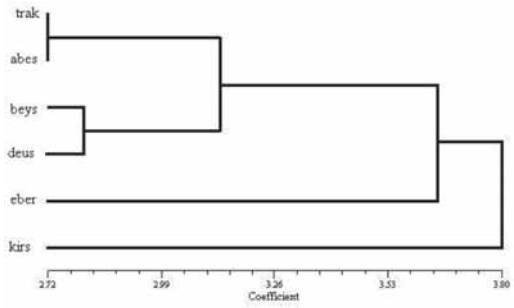

Figure 4. UPGMA dendogram that shows morphometrical relations of *Arvicola terrestris* populations depend on external and internal measurements

DISCUSSION

The shape of organs or structures are important in the interaction between the organism and its environment. It is quite common to associate taxonomic differentiation with morphological divergence (Renaud and Michaux, 2003; Rohlf, 1990).

Arvicola subspecies; Arvicola amphibius persicus, Arvicola amphibius armenius and Arvicola amphibius hintoni which are recorded from Anatolia and those subspecies are investigated in a previous study (Mursaloğlu, 1975) and only persicus and hintoni accepted as a subspecies because of differentiation of populations depend on morphological and biometrical features. And armenius noticed as a synonym of percicus. Concequently Mursaloğlu (1975) defined Arvicola amphibius cernjavskii from Turkish Thrace and Arvicola amphibius persicus from Central Anatolia. Again, this review stops more than 40 years ago. For example, the data and statements presented by Krystufek & Vohralik (2005) are not considered.

In this study, in Anatolian populations; average head-body length 179 mm, tail lenght 125 mm, hind lenght 27-42 mm, condylobasale lenght 39,26-41,48 mm, in Thrace populations; average head-body length 193,5 mm, tail lenght 121.17 mm, hind lenght 33-36 mm, condylobasal lenght 36,15-39,76 mm are measured. Depend on these measurements except tail measurements of Anatolian populations are consistent with Miller (1912) and the other differences is head and body length of Thrace populations.

Mursaloğlu (1975) recorded Arvicola terrestris cernjavskii from Trakya, and Arvicola terrestris persicus subspecies from Central Anatolia. According to Mursaloğlu (1975), the average and minimum - maximum measurements of 11 Arvicola terrestris persicus samples obtained from Central Anatolia; the length of the whole length is 297.5 mm (229 - 318), the head - body length is 180.2 mm (115 - 200) and the weight is 170.6 g (130 - 209). Measurements of Western Anatolian Arvicola terrestris persicus specimens examined in this study compared with the samples obtained from Central Anatolia by Mursaloglu, whole lenght, head-body lenght and weight measurements were found to be smaller. These average whole lenght values are greater than the maximum value given by the researcher for the whole length (318 mm) and head - body length (200 mm). In addition, the mean value of the weight measurements of Arvicola terrestris persicus subspecies samples of Mursaloğlu (1975) is 170.6 gr. The average weight of the samples collected in this study is larger.

In our study, it is first time we analysed geometric morphometrics on Turkish Arvicola samples distributed on

western part of Anatolia. A total of 37 landmarks on dorsal, ventral and lateral view of the skull were used to identified differentiation level of Arvicola populations in western part of Anatolia. We found any evidence of differentiation between Thrace and Anatolia populations according to dorsal view of water vole skull. However ventral and lateral view of water vole skull strongly support that Turkish Thrace and Western part of Anatolia water vole populations are highly differentiated two subspecies of water vole Arvicola amphibius persicus and Arvicola amphibius cerncavskii distributed through Western part of Turkey by using landmark based geometric morphometrics.

Thus, ventral and lateral view of skull is quite efficient to determine intraspecies variations of water vole by using geometric morphometrics. On the other hand, dorsal view of water vole skull is not informative to explain intraspecific variations of water vole subspecies throughout Western part of Turkey.

In addition to these, during field study, we observed that the distribution area of Arvicola amphibius is highly limited by water pollution, anthropogenic impact and climate change.

References

1. Castiglia R, Aloise G, Amori G, Annesi F, Bertolino S, Capizzi D, Mori E, Colangelo P, The Italian peninsula hosts a divergent mtDNA lineage of the water vole, Arvicola amphibius s.l., including fossorial and aquatic ecotypes. (2016) 27, doi:10.4404/hystrix–27.2–11588.
2. Kryštufek B, Vohralík V. Mammals of Turkey and Cyprus: Rodentia I: Sciuridae, Dipodidae, Gliridae, Arvicolinae. Zgodovinsko društvo za južno Primorsko, Koper.2005
3. Miller G.S. Catalogue of the Mammals of Western Europe in the collection of the British Museum. British Museum: (Nat. Hist), London. 1912
4. Meylan A, Fossorial Forms of the Water Vole, Arvicola terrestris (L.), in Europe1. EPPO Bulletin 7, 209–218, doi:10.1111/j.1365–2338. (1977) tb02723.x.
5. Mursaloğlu B, Türkiye su sıçanlarının, Arvicola, coğrafik varyasyonları. Tübitak V. Bilim Kongresi Tebliğleri, (1975) 353–368.
6. Musser GG, Carleton MD, Family Muridae. In: Wilson, D.E., Reeder, D.M. (Eds.), Mammal Species of the World. A Taxonomic and Geographic Reference. The Johns Hopkins University Press, Baltimore. 2005
7. Renaud S, Michaux JR, Adaptive latitudinal trends in the mandible shape of Apodemus wood mice. Journal of Biogeography 30, (2003) 1617–1628, doi:10.1046/j.1365–2699.2003.00932.x.
8. Rohlf FJ, Fitting curves to outlines. In: Rohlf FJ, Bookstein FL, eds. The University of Michigan Museum of Zoology. 1990
9. Rohlf FJ, Shape statistics: Procrustes superimpositions and tangent spaces. J. Classif 16, (1999) 197–223.
10. Rohlf FJ, Tps Series. State University of New York, Stony Brook, Department of Ecology and Evolution. 2004
11. Slice DE, Morpheus, Software for Morphometric Research. Department of Biomedical Engineering Wake Forest University School of Medicine, Winston–Salem, NC, USA. 2002
12. SPSS, SPSS for Windows, Release 13.0. Standard Version. SPSS Inc., Chicago, IL, USA. 2004
13. Steiner H, Vauk G, Saugetiere aus dem Beyşehir Gebiet (vil. Konya, Kleinasien). Zoologischer Anzeiger 176, (1966) 97–102.
14. Zelditch M. L., Swiderski D. L., Sheets H. D. and Fink, W. L. 2004. Geometric morphometrics for biologists: a primer, Elsevier, 443 p.

Hittite Journal of Science and Engineering, 2019, 6 (2) 137-145
ISSN NUMBER: 2148-4171
DOI: 10.17350/HJSE19030000139

Semi-IPN poly(AAm-co-MAPTAC)-Chitosan Hydrogels: Synthesis, Characterization and Investigation of Their Potential Use as Nitrate Fertilizer Carrier in Agriculture

Demet Aydinoglu
Department of Food Processing, Yalova University, 77500, Yalova, TURKEY

ABSTRACT

Poly(acrylamido-co-3-methacrylopropyl trimethyl ammonium chloride)-Chitosan semi-IPN hydrogels were prepared by free-radical polymerization of the monomer acrylamide (AAm) and the cationic comonomer 3- methacrylo propyl trimethyl ammonium chloride (MAPTAC) with N,N-methylene bisacrylamide (BAAm) as the crosslinker in presence of chitosan, which is also cationic natural polymer. The swelling properties were investigated by using gravimetric method, whereas morphological structure and mechanical performance of the hydrogels were identified by employing scanning electron microscopy (SEM) and uniaxial compression machine, respectively. Potassium nitrate was used as the model fertilizer and its loading and release experiments were carried out with conductimetric measurements. All the results indicated that both cationic MAPTAC units and chitosan were strongly influenced the gel properties from pore structures and swelling properties to nitrate loading and release % values due to the repulsion forces formed between the positive charges in MAPTAC and chitosan, as well as the interaction between these ionic groups and water molecules. The new semi-IPN hydrogels exhibited good slow nitrate release, better swelling and improved mechanical performances in especially some composition . Thus it can be concluded that the new semi-IPN hydrogels have a potential to use them as a nitrate fertilizer carrier. Especially the further investigations performed with A-1M-0.05C hydrogel in soil media revealed that the hydrogel at this combination can be evaluated as one of the promising materials which can be safely used as controlled fertilizer release system..

Keywords:
Hydrogel; Acrylamide; MAPTAC; Controlled fertilizer release.

Article History:
Received: 2019/02/24
Accepted: 2019/06/27
Online: 2019/06/30

Correspondence to: Demet Aydınoğlu, Yalova University, Department of Food Processing, Yalova, TURKEY
Tel: +90 (226) 815 5435
Fax: +90 (226) 815 5439
E-Mail: demet.aydinoglu@yalova.edu.tr

INTRODUCTION

Hydrogels, which are formed by chemical or physical crosslinking of hydrophilic polymers via covalent bonds or physical interactions (hydrogen bonds, ionic interactions etc.), were first introduced to the literature by Wichterle ve Lim in 1960. The researchers were succesful in developing poly(hydroxyethyl methacrylate) hydrogels with soft structure as an alternative to poly(methyl methacrylate), which had been used in fabrication of contact lens and was not much comfortable because of its hard structure [1]. After this study, the number of works on hydrogels has increased rapidly and the various hydrogels having both synthetic and natural structure such as poly(acrylamide), poly(acrylic acid), poly(N-isopropyl acrylamide), poly(vinyl alcohol), chitosan, gelatin and alginate etc., were prepared using different types of monomers, co-monomers and crosslinkers [2-9]. Hydrogels are attractive materials because of their soft structure, high water uptake capacities, (in some cases they absorb water thousands of times their own dry weights), biocompatible structures, easily biodegradation and easily production. Due to the mentioned advantages, hydrogels have being used in various fields such as medicine, pharmacy, food, environment, mechanical and civil engineering and they offer several solutions for different applica-

tions [10-12]. Although hydrogels have many beneficial properties, their use in some applications, especially in which mechanical stability are required, are restricted because of their soft and fragile structures and especially their easily degradation in wet state. In order to overcome these negative sides and to gather the beneficial properties of various chemical subtances in one material, several strategies have been proposed. The techniques of blending, copolymerization with hydrophobic monomers and preparation of semi and full interpenetrating networks (semi or full-IPN) were successful in obtaining the hydrogels having desired properties [13].

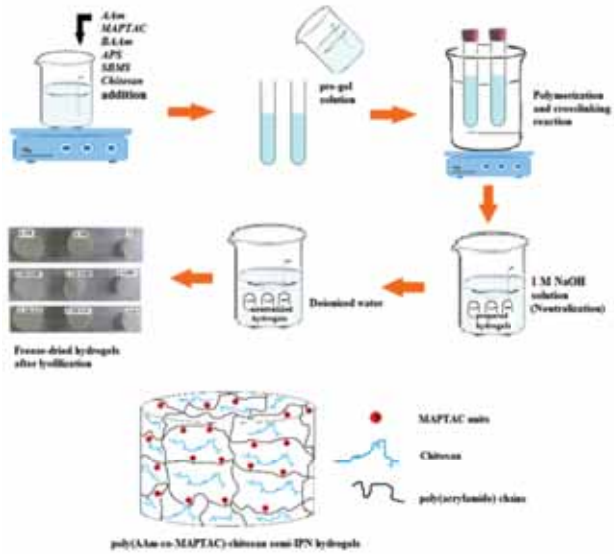

Figure 1. Synthesis schema of the poly(AAm-co-MAPTAC)-chitosan semi-IPN hydrogels

Semi-IPN hydrogels, which are one of the abovementioned techniques, are formed by combination of two different types of polymers, one of which is in network form and the other one is in a linear form [14]. The works on semi-IPN hydrogels have proved that this type of hydrogels increase mechanical strength of wet hydrogels and reduce degradation rates [15]. According to the literature, it is noticed that polysaccharides have been mainly used as linear polymer for production of semi-IPN in these studies [16]. Polysaccharides offer several solutions for particularly the fieds in which biocompatible and nontoxic materials are preferred, such as medicine, food etc. The natural structure of polysaccharides and the environmental sensitive swelling properties of the synthetic hydrogel network can be gathered with the abovementioned semi-IPN hydrogels. The reason that the most widely used polymers in preparation of semi-IPN hydrogels are polysaccharides can be explained with their abundance, low cost, reneweability and suitable for chemical modifications.

Chitosan, which is one of the most known polysaccharides, is a cationic natural polymer formed by bonding N-acetyl-D-glycosamine units with β-(1 → 4) glycosidic bonds and obtained by deacetylation of chitin, which is produced from insect shells [16]. Chitosan is one of the attractive materials due to both its natural structure and pH dependent swelling behavior owing to their high number of amine groups. In most of the works involving semi-IPN, in which chitosan was used as a linear polymer, it was searched that the release of anionic drug, protein and insulin release [17-20], and also removal of humic acid from waste water [21].

Although various semi-IPN hydrogels having chitosan as a linear polymer have been widely studied, it was no noticed a research on a semi-IPN structure formed by combination of cationic poly[acrylamide-co-(3-methacryolypropyl) trimethyl ammonium chloride] (poly(AAm-co-MAPTAC) network and chitosan polymer. Therefore, in present study, it was aimed at preparation of poly(AAm-co-MAPTAC)-Chitosan semi-IPN hydrogels and estimated that both the ammonium and amine groups in MAPTAC and chitosan, respectively would create synergy in several properties of the hydrogel. It can also be stated that the other prediction was that the amine groups in chitosan would be more active in big pores like in poly(AAm-co-MAPTAC) network than in nonionic ones. Moreover it was thougth that introducing chitosan polymer into the poly(AAm-co-MAPTAC) structure may help increment in the mechanical stability of the hydrogels without the need of increasing crosslinker content.

On the other hand it was investigated that the potential use of these novel hydrogels as a controlled release fertilizer material, which is the one of the most popular applications of the hydrogels, recently. As it is well known that hydrogels are used in agricultural applications as a fertilizer and pesticide carrier and enable these agrochemicals to release into soil gradually and thus they are named as controlled-release fertilizer (CRF). In conventional agricultural applications, fertilizers which are placed near to the roots of plants, undergo quickly dispersion and dissolvation with irragation before the plant has benefited sufficiently. This fact which cause to overdose fertilization leads to both the over consumption, thus high cost and damage to plant [22]. For this reason in especially last decade the number of the investigations on CRF has increased rapidly. In this context, various polymeric hydrogels such as polyacrylamide, poly(N-hydroxymethyl acrylamide-co-acrylic acid), chitosan, gelatin and gelatin-poly(acrylamide)-gelatin IPN hydrogels have been examined with many studies, which proved that controlled release of fertilizer was achived by using these polymeric hydrogels [23-27]. However there is still need of further studies on developing and designing new different formulations for CRF production, because some of the abovementioned studies are lack of some informations for example release rates in soil media and mechanical stability

measurements of CRF materials, which is also vital because it is required that the material must keep its structural integrity up to release of the fertilizer in the carrier finish. The abovementioned lacks motivated to study also the controlled release fertilizer of these hydrogels. In this work, nitrate was used as fertilizer, because it was estimated that the high number of cationic groups in the semi-IPN hydrogels would increase the nitrate loading and also decrease the release rate of the hydrogels.. Moreover, it was expected that these hydrogels would exhibit not only good loading and release behavior for nitrate fertilizer but also sufficient mechanical strength owing to their semi-IPN structure.

With the abovementioned aims, a series of hydrogels having acrylamide and 3-methacryolypropyl trimethyl ammonium chloride as a monomer and comonomer respectively and N,N-methylene bisacyrlamide as a cross-linker was synthesized in presence of chitosan and obtained semi-IPN poly(AAm-co-MAPTAC)-chitosan hydrogels with different MAPTAC and chitosan content. These hydrogels were characterized in term of swelling, morphology and mechanical stability via several characterization techniques. The hydrogels were subjected to nitrate loading and release experiments in both of the pure water and in soil. And finally biodegradability of the optimized hydrogel was searched.

MATERIALS AND METHODS

Materials

Acrylamide (AAm), 3-methacrylo propyl trimethyl ammonium chloride (MAPTAC) and N,N-methylene bisacrylamide (BAAm), which were used as main monomer, comonomer and crosslinker, respectively and also chitosan, which was used as linear polymer were all bought from Aldrich Chemicals (Milwaukee, WI,USA). Ammonium peroxydisulfate (APS) and sodium meta bisulfite (SMBS), which were employed as redox initiator pair, were purchased from Merck (Darmstad, Germany). Acetic acid and sodium hydroxide, used for preparation of the hydrogels and also potassium nitrate used for controlled fertilizer release experiments, were supplied by Aldrich Chemicals (Milwaukee, USA). The soil sample was bought from a local market. All the reagents were used as received and deionized water was used throught the experiments and measurements in the study.

Preparation of the poly(AAm-co-MAPTAC)-chitosan semi-IPN Hydrogels

Poly(AAm-co-MAPTAC)-chitosan semi-IPN hydrogels were synthesized by employing free radical polymerization in presence of chitosan, using BAAm as crosslinking agent. The synthetic route for the hydrogels was demostrated in Fig. 1. Briefly, AAm and BAAm were dissolved in 10 mL of aqueous acetic acid solution (1% wt.) in turn under magnetic stirring. Then, the comonomer MAPTAC and APS were added to the mixture and continue to mixing. Finally, the reaction was started after pouring chitosan and SMBS into the solution and transferred into air-tight glass tubes. The reaction was carried out in a water bath at 35 °C for 24 h. The resulting hydrogels were cut into the discs that have a approximate length of 1 cm. and immersed and left to neutralization into 1 M NaOH solution for an hour in order to prevent chitosan in the hydrogel from dissolution. After this neutralization, the hydrogels were placed into deionized water for purification and refreshed the water every other day. The fully swollen hydrogels were subjected to lyophilization and referred as A-XM-YC, where X and Y represent the molar ratio of MAPTAC and the weight of chitosan, respectively. The monomer feed according to hydrogel codes was given in Table.1.

Characterization

Swelling tests of the hydrogels were performed in deionized water at room temperature. The water uptake capacities of the hydrogels were determined by gravimetrically. For this, the dry hydrogel samples of which weights were known were immersed in deionized water and allowed to attain the maxiumum swelling degree by following the-

Table 1. Experimental conditions of the preparation of the hydrogels.

Hydrogel	*AAm($x10^{-2}$ moL)*	*MAPTAC ($x10^{-2}$ moL)*	*BAAm($x10^{-4}$ moL)*	*APS(mg)*	*SMBS(mg)*	*Chitosan(g)*
A	*1*	*0*	*1.67*	*5.7*	*1.9*	*0*
A-1M	*0.99*	*0.01*	*1.67*	*5.7*	*1.9*	*0*
A-2M	*0.98*	*0.02*	*1.67*	*5.7*	*1.9*	*0*
A-0.05C	*1*	*0*	*1.67*	*5.7*	*1.9*	*0.05*
A-1M-0.05C	*0.99*	*0.01*	*1.67*	*5.7*	*1.9*	*0.05*
A-2M-0.05C	*0.98*	*0.02*	*1.67*	*5.7*	*1.9*	*0.05*
A-0.1C	*1*	*0*	*1.67*	*5.7*	*1.9*	*0.1*
A-1M-0.1C	*0.99*	*0.01*	*1.67*	*5.7*	*1.9*	*0.1*
A-2M-0.1C	*0.98*	*0.02*	*1.67*	*5.7*	*1.9*	*0.1*

ir weights at pre-determined time intervals. During the swelling process the water was refreshed every other day. The percent swelling value was calculated by following equation:

$$S\% = [(m_s - m_d)/m_d] \times 100 \quad (1)$$

where S%, m_s and m_d show the equilibrium swelling percent, weights of swollen and dry hydrogels, respectively.

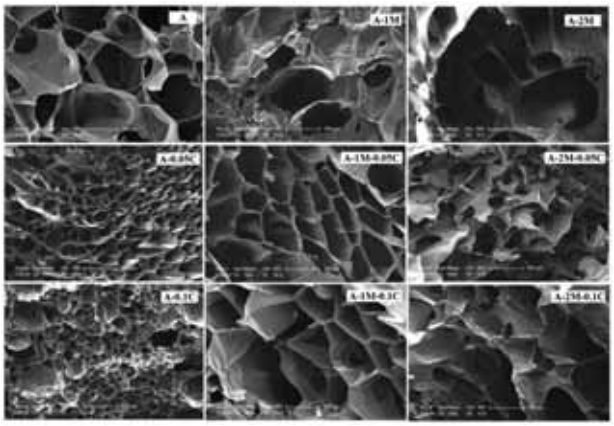

Figure 2. SEM images of the poly(AAm-co-MAPTAC)-chitosan semi-IPN hydrogels. The scale bars are 200 μm

The mechanical strengths of the hydrogels were identified by applying compressing test. The fully swollen samples having 1 cm of the length were subjected to uniaxial compression by using Zwick/Roell Z1.0 universal testing machine (Zwick Gmb&Co.KG,Ulm,Germany) equipped with a 50-N load cell at a compression rate of 3 mm/min. The compression was maintained upto 60% of the deformation rate and the compression force values versus the deformation percentages were monitored.

The pore structure of the freze-dried hydrogels was investigated with SEM technique by using an ESEMFEG/EDAX Philips XL-30 instrument (Philips, Eindhoven, The Netherlands).

Loading and release experiments

Nitrate fertilizer loading capacities were followed by conductimetric measurements, using C65/C66 model conductivity meter (Milwaukee WI,USA). The pre-weighed hydrogel samples were placed into 25 mL of aqueous KNO_3 solution (1% wt.) and allowed to KNO_3 penetration for 48 hour. The KNO_3 loaded hydrogels were then removed from the medium and KNO_3 concentration in the solution was determined from the conductimetric measurements. The loading % KNO_3 was calculated according to the following equation:

$$\text{Loading}\% = [(c_0 - c_d)/(c_0 \times m_d)] \times 100 \quad (2)$$

where c_0 and c_d denote the initial and the final KNO_3 concentrations, respectively, while m_d represents the weight of the dry hydrogel sample.

Release experiments were performed by placing the pre-weighed KNO_3 loaded hydrogels into 100 mL of deionized water. The release KNO_3 amounts were determined by measuring the conductivity of the solution at certain time intervals and calculating using the following equation:

$$\text{Release}\% = [(c_t \times 0.1)/(m_{KNO3} \times m_L)] \times 100 \quad (3)$$

where c_t, m_{KNO3} and m_L show the KNO_3 concentration at certain time intervals, the KNO_3 amount released by the hydrogel and the weight of the KNO_3 in the loaded gel, which determined from the loading experiments.

Release tests were repeated for soil medium with only the hydrogel exhibited good swelling, mechanic, loading and the lowest release rate performance. With this aim, the KNO_3 loaded chosen hydrogel (A-2M-0.05C) samples were weighed and placed into the 100 g of the soil in a beaker by burrying them in tea-bags made of nylon wire mesh. Then 30 mL of deionized water was added and the beaker was covered with a aluminium foil to protect the soil from evaporation and kept at room temperature for 35 days. One of the samples was withdrawn from the soil at every 24 hours and immersed into deionized water for 24 hours. After 24 hours KNO_3 concentrations were determined by conductimetric measurements and used to calculate the % KNO_3 release of the hydrogels in soil media by employing the Eq.3.

Biodegradation tests

The biodegradability test was performed by using the KNO_3 loaded dry A-1M-0.05C hydrogel samples of which weights were ranged between 0.08 and 0.12 g. In this test, dry hydrogels were burried into a soil by inserting in a teabag in order to prevent the hydrogels from as much as any dirt or etc. The container, which was filled with soil, was then covered with aluminium foil to protect the soil from evaporation and kept at room temperature. The samples were taken from the soil and weighed at pre-determined time intervals (7 days). The weight loss of the gels was determined by following the weight of the hydrogels, which was used in the equation below:

$$\%\ \text{weght loss} = [(m_i - m_f)/m_i] \times 100 \quad (4)$$

where m_i and m_f represent the initial and the final weights of the hydrogel samples.

Table 2. Equilibrium swelling percents and the compression strength value against to 60% deformation rate of the hydrogels.

Hydrogel	*Sw%(eq)*	*Compression strength (N)*
A	*2417*	*1.16*
A-0.05C	*2055*	*2.79*
A-0.1C	*1827*	*5.23*
A-1M	*5164*	*2.79*
A-1M-0.05C	*4443*	*3.34*
A-1M-0.1C	*5711*	*1.21*
A-2M	*7712*	*0.93*
A-2M-0.05C	*6680*	*2.90*
A-2M-0.1C	*11465*	*0.92*

Table 3. KNO_3 loading amounts of the hydrogels.

Hydrogel	*KNO3 loading %*
A	*10.66*
A-0.05C	*8.75*
A-0.1C	*6.22*
A-1M	*55.20*
A-1M-0.05C	*50.52*
A-1M-0.1C	*60.71*
A-2M	*63.81*
A-2M-0.05C	*59.40*
A-2M-0.1C	*65.22*

RESULTS AND DISCUSSION

Characterization

Morphological structure:

The SEM images illustrated in Fig. 2 show the inner surface structure of the hydrogels. According to the pictures, it was clearly observed that A has relatively homogenously distributed open pores with an approximate size of 300 micrometer, while A-0.05C and A-0.1C hydrogels obtained by using 0.05 and 0.1 g of chitosan, respectively, was found to have smaller pores than A. Moreover, it was seen that most of the pores in all the nonionic hydrogels were interconnected and homogenously distributed. It was significantly observed from the micrographs that the addition of chitosan into the hydrogel composition caused to decrement in the pore sizes most probably due to the fact that it filled some of the empty space of the pores.

On the other hand, in the case of the ionic hydrogels, the quitely increased pore volumes in both of the A-1M and A-2M are remarkable. In addition to these greater pores, also more foliaceous structure and heterogeneously distributed pores in these gels are noticeable, which may be related to that AAm and MAPTAC units were not well ordered in the hydrogel network. In particular, being have pores with nearly 500 micrometer in size, showed that the hydrogels with MAPTAC created bigger pores compared to the nonionic hydrogels, likely due to the repulsion forces between the quaternize amine groups in MAPTAC units. But, this extent decreased by a quarter with the inserting of 0.05 g chitosan in the hydrogel composition. This fact was ascribed to the similar way with the abovementioned for the A-0.05C and A-0.1C hydrogels. However, in spite of the case in the nonionic hydrogels, further increase in chitosan (0.1 g) resulted in greater pores of which sizes reached to approximately 500 micrometer again. This first decrement and then increment in the pore sizes with the chitosan addition can be suggested that the inserting of chitosan up to a certain amount (0.05 g) increased the bulk density of the gel, filling some of the voids and leading to relatively small pores (first effect), although there is an opposite effect (second effect) which was explained with the repulsion forces between the protonated amine groups in chitosan and the quaternize amine groups in MAPTAC units, contributing to have bigger pores. As seen from the micrographs that the first effect was dominant over the pore size in the case of presence of 0.05 g chitosan. However, when the chitosan content increased to 0.1 g, the number of protonated amine groups originated from chitosan has doubled and much more repulsion between these doubled amine groups and the quaternized amine groups in MAPTAC units occurs and thus the second effect become dominant.

Swelling properties of the hydrogels

The swelling percentages seen both in Fig. 3 and Table.2 showed that presence and increase of ionic comonomer (MAPTAC) enhanced the water absorption of the hydrogels. It resulted as (Sw(A)< Sw(A-1M) < Sw(A-2M)) as expected. The maximum swelling degree was achieved with A-2M hydrogel had a value of 7712% wt. On the other hand, including 0.05 g of chitosan into the composition was found to reduce their swelling capacities. This fact can be explained in the following way: Addition of chitosan into monomer feed resulted in lower swelling extents, decreasing the pore size by filling the some spaces of the pores for all the hydrogels, as seen in the their micrographs, although it has many ionic and hydrophilic groups. However,in spite of the abovementioned case, further increment in chitosan improved the water absorption of the ionic hydrogels, while the nonionic ones remained their water uptake decrement. For example, the swelling degree of A-1M-0.05C was found to be 4413%, whereas it was calculated to be 6680% at 0.1g chitosan content. Similarly, A-2M-0.05C was found to have a swelling value of 5711% , while A-2M-0.1C exhibited a swelling degree of 11465% .This first increase and then decrease pattern of the ionic hydrogels can be assessed with two opposite effects which created most probably by addition of chitosan and explained above for their morphological structure. One of these effects may be suggested that pore sizes declined with chitosan addition due to its filling some

spaces of the pores, leading to lower swelling degrees, the second one may be explained with the repulsion forces between the cationic groups in chitosan and MAPTAC, which accounts for having more extended structure of the networks, resulting in more water absorption. These swelling behavior of the ionic hydrogels can be also supported by their SEM images. According to the results, it is obvious that the hydrogels having 0.05 g chitosan exhibited lower swelling degrees due to the fact that the first effect is dominant, while those containing 0.1 g chitosan was found to have higher water absorption capacities as a consequence of the second effect, which become dominant in this composition because of the fact that cationic groups in chitosan has doubled with the 0.1 g of chitosan addition. In addition to having extended structure and greater pore size, the ionic species in the gel play an important role in the water absorption, creating ion-dipol and dipol-dipol interactions between the ionic groups and water molecules, which enable the more water molecules to enter into the network.

On the other hand the gradually decrement in water uptake capacities of the nonionic hydrogels (A, A-0.05C and A-0.1C) with increased chitosan is proved to the abovementioned suggestion, which was done with the repultion forces between the ionic groups, for the hydrogels with MAPTAC.

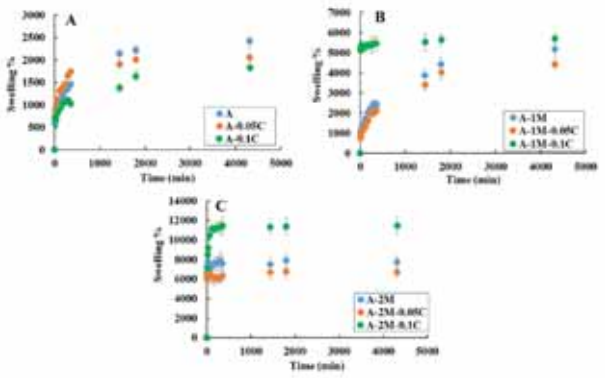

Figure 3. Swelling curves of the poly(AAm-co-MAPTAC)-chitosan semi-IPN hydrogels in deionized water (A): Acrylamide hydrogels ; neat and including 0.5 and 1 % wt. chitosan, (B): Acrylamide hydrogels having 1% mol ratio of MAPTAC; neat and 1 % wt. chitosan, (C): Acrylamide hydrogels having 2% mol ratio of MAPTAC; neat and 1 % wt. chitosan

Mechanical properties of the hydrogels:

The mechanical strengths of the swollen hydrogels were identified by utilizing an uniaxial compression tests. The results were presented as stress-strain curves in Fig.4 and the maximum compression force values against to 60% deformation were given in Table.2. The mechanical measurements showed that incorporation of chitosan into the nonionic poly(acrylamide) hydrogels increases the maximum compression force from 0.81 N up to 5.23 N, as expected. This improvement in the mechanical performance can be ascribed to formation of smaller pores with addition of chitosan, leading to higher resistance to deformation and also homogenously distribution of the stress in the hydrogel matrix. This enhanced mechanical stability was also observed for the ionic hydrogels having 0.05 g of chitosan, most probably due to the same reason with the nonionic ones. However at higher chitosan content, this gradually increment obtained from nonionic hydrogels was not observed for the ionic ones. For instance, the maximum force applied to A-1M-0.05C at 60% deformation rate was calculated to be 3.34 N, whereas that performed to A-1M-0.1C was found to decrease to 1.21 N. Like to the hydrogels containing 1% wt. MAPTAC, also the A-2M-0.05C and A-2M-0.1C hydrogels displayed the similar mechanical behavior in response to further chitosan addition. These variation in the gel strength can be attributed to the both of the morphological structures and swelling values of the ionic hydrogels. Since the mechanical tests were performed with the samples in wet form, the hydrogels having high absorption capacities exhibited poor mechanical stability.

On the other hand, it was interestingly found that the A-1M hydrogel displayed greater mechanical performance in comparison to A, in spite of the expectations. It is thougt that this increment was related to the difference in the sizes of the pendant groups of AAm and MAPTAC units. Having larger pendant group made A-1M hydrogels exhibited better mechanical performance with respect to A gels, due to the resistance of larger side groups to deformation. However, for A-2M hydrogel, the gel strength was found to be close to that of A, most probably due to its high swelling capacity which influence the mechanical stability alhough it has also the large side groups originated from MAPTAC. According to the results it can be inferred that the high swelling property of A-2M determines the mechanical performance of the gel compared to the large side group effect.

KNO_3 loading and release behavior of the hydrogels

The nitrate loading % values of the hydrogels immersed in 1% (wt.) KNO_3 solution for 48 h were obtained from the conductimetric measurements by using the calibration curve and given in Table.3. The results showed that ionic hydrogels absorbed more NO_3^- ions than nonionic ones most probably due to the both reason of their high number of cationic groups which act as a receptor for negative charges like nitrate and great swelling capacities which increase nitrate penetration. On the other hand, it is seen that the hydrogels having 0.1 g of chitosan displayed a slightly increased loading capacities. This fact can be ascribed to the extra cationic groups presented by increased amount of chitosan. The nitrate release % values of the hydrogels were illustrated in Fig.5. Among the hydrogels, the lowest release percents ranged between 31 and 35% were obtained for the nonionic hydrogels.

This fact can be attributed to the lower swelling capacities of A, A-0.05C and A-0.1C hydrogels, which govern release process of the entrapped ions. Additionally, the maximum release ratio was achieved by A-2M hydrogel with a release percent of 82%. On the other hand, the nitrate release ratios of all the ionic hydrogels were found to be close to eachother and varried between 71 and 82. However in the agricultural applications, it is desired the superabsorbents to have slow release rates in order to be efficient. When this factor is taken into account, A-1M-0.05 hydrogel seem to have optimized composition with its especially slower release rate, moderate good swelling capacity and also good mechanical stability which is also very important in these application, because of the fact that if the material has not adequate strength, it loss its physical integrity and some cracks occur on its surface leading to burst release.

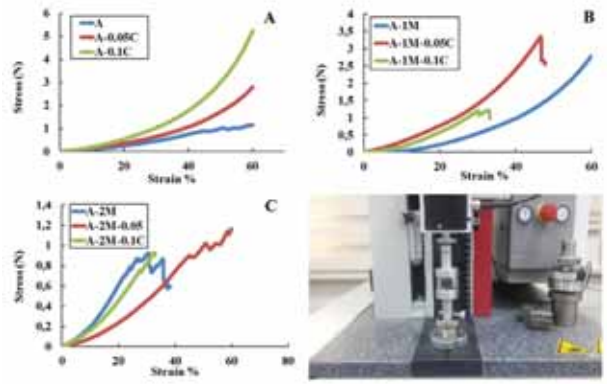

Figure 4. Stress-strain curves of the poly(AAm-co-MAPTAC)-chitosan semi-IPN hydrogels (A): Acrylamide hydrogels ; neat and including 0.5 and 1 % wt. chitosan, (B): Acrylamide hydrogels having 1% mol ratio of MAPTAC; neat and 1 % wt. chitosan, (C): Acrylamide hydrogels having 2% mol ratio of MAPTAC; neat and 1 % wt. chitosan

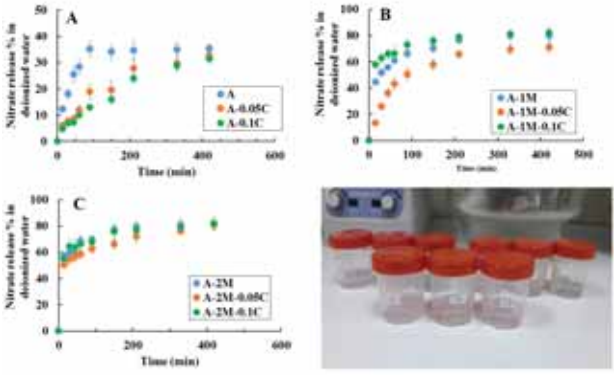

Figure 5. KNO3 release pattern of the hydrogels in deionized water. hydrogels (A): Acrylamide hydrogels ; neat and including 0.5 and 1 % wt. chitosan, (B): Acrylamide hydrogels having 1% mol ratio of MAPTAC; neat and 1 % wt. chitosan, (C): Acrylamide hydrogels having 2% mol ratio of MAPTAC; neat and 1 % wt. chitosan.

KNO_3 release behavior of the hydrogels in soil

Since the most efficient composition was determined to be A-1M-0.05C, the experiment in soil was conducted with the only these hydrogel samples. The release behavior in soil was depicted in Fig.6. According to the results it was revealed that at the beginnig of the process, the burst release was observed, after that the release rates become slower. The final release value of A-1M-0.05C in soil, attained by approximately 18th day, was found to be 67%, which is said to be close to that of in deionized water.

Biodegradability

Like to the release experiments carried out in soil media, the biodegradability test was performed with the only A-1M-0.05C hydrogel samples. The results obtained from the soil burial test were illustrated in Fig.7. According to the weight loss ratios, it was found that the hydrogel with 1% MAPTAC prepared by using 0.05 g of chitosan, exhibited relatively poor biodegradability. The maximum biodegradation ratio (12.3 %) was achieved after 35 days. In fact, this low biodegradability was estimated before the test due to the synthetic structure and relatively high crosslink density of the hydrogel, which increase the resistance to biodegradation. However although its degradation ratio was found to be low, it can be interpreted that the high pore size and also the natural biodegradable chitosan content of the hydrogel slightly increased to its biodegradability, when compared to corresponding conventional materials in the literature, which states that less than 10% of polyacrylamide hydrogels degrade after 28 days [28].

CONCLUSION

In present study, new poly(AAm-co-MAPTAC)-chitosan semi-IPN hydrogels were succesfully prepared to improve the properties of the poly(AAm-co-MAPTAC) hydrogels. The mophological analyses showed that chitosan addition caused to reduce the pore sizes of nonionic hydrogels. However, this case was found to be different for the hydrogels with MAPTAC. It was observed that the ionic hydrogels had smaller pores when 0.05 g of chitosan was incorporated into the composition, but with the further amount resulted in greater pore sizes, most probably due to the extended hydrogel structures arising from repulsion forces between the positive charges in chitosan and MAPTAC units. On the other hand, it was found that introducing chitosan at a 0.05 g dosage decreased to the swelling extents, while addition of 0.1 g of chitosan resulted in increment in the water uptake values except for the nonionic hydrogel. It was suggested that existence of a certain amount of chitosan, which seems to be 0.1 g, provided the ionic gels to have higher swelling values as a consequence of formation and become noticeable of

the repultion forces between the positive charged amine and quaternize ammmonium groups, which belong to chitosan and MAPTAC units, respectively and also it may be related to extra hydrogen bonds, ion-dipol and dipol-dipol interactions occured between the high number of ionic groups and water molecules which enhance the swelling capacities, by facilitating diffusion of water molecules into the hydrogels. These swelling results showed that chitosan addition beyond a certain amount improved the water absorption behavior of the ionic hydrogels. Additionally, these swelling results are also good agrement with their pore sizes and can be explained with the morphological structures.

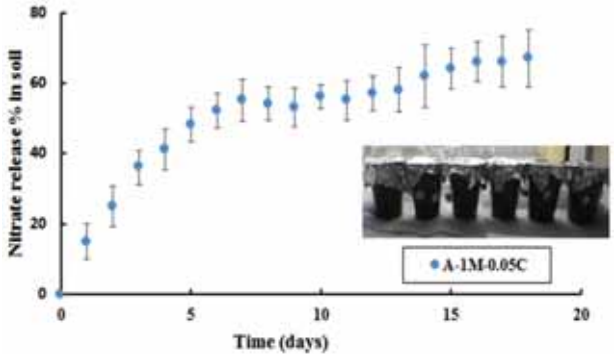

Figure 6. KNO3 release pattern of the hydrogels in soil.

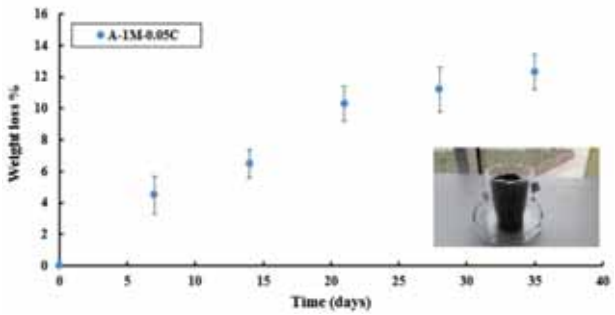

Figure 7. Weight loss % of the hydrogels versus time

The obtained mechanical results revealed that the gel strengths were strongly correlated with their swelling ratios, since as it is well known that high swelling capacities make the gels more fragile and easy breakable. However it should be noticed in some comparisons in the modul values of the hydrogels that the MAPTAC units can influence the mechanical performance by offering relatively larger pendant groups with respect to AAm units to the structure as well as the swelling ratio. Therefore the mechanical results showed that A-2M had higher compression strength than the nonionic hydrogel (A), although it had quite high swelling degree.

As to the fertilizer loading and release behavior, the positive charges in the hydrogels played an important role in both of the loading and release experiments. Negative charged nitrate ions were more absorbed by A-2M-0.1C, and also among the semi-IPN hydrogels, the maximum release amount and percentages were obtained with the same hydrogel composition, as expected from its high water uptake capacity, which drive the loading and release process of solute molecules by hydrogels. According to the results it was seen that the second place was taken by A-1M -0.1C. The further experiments, which were carried out in soil media and performed with the only the ionic hydrogel having 1% MAPTAC and 0.05 g of chitosan (A-1M-0.05C), regarding the potential efficiency of this hydrogel after the evaluation of all the results obtained from swelling, mechanical tests and also its slower release rates found from release experiments in water, showed that nitrate release continued upto almost 20 th day in soil media, by release 69% of pre-loaded nitrate , which can be considered as a slow fertilizer release. On the other hand biodegradability results demonstrated that the maximum biodegradation ratio (12.3 %) was achieved after 30 days for this hydrogel. Here although this low biodegradability seems to be negative side of this hydrogel for agricultural applications, one can evaluated that this disadvantageous can be reverse, when its efficieny in both of loading and release is taken into account, due to the fact that smaller quantity of the hydrogel would be sufficient as controlled fertilizer release material as compared to easily degraded ones.

It can be concluded that the new hydrogels in which semi-IPN structure obtained by combination of poly(AA-co-MAPTAC) and chitosan have a potential to use them as a nitrate fertilizer carrier. Especially the further investigations performed with A-1M-0.05C hydrogel in soil media revealed that the hydrogel at this combination can be evaluated as one of the promising materials which can be safely used as controlled fertilizer release system.

ACKNOWLEDGEMENTS

The financial support given by Yalova University Scientific Research Projects Coordination Department (Project no. 2018.AP.0010) is gratefully acknowledgement. The authors also thank Dr. Bilge Gedik Uluocak for helping in the SEM-based characterization technique.

References

1. Wichterle O, Lim D. Hydrophilic gels for biological use. Nature 185 (1960) 117– 118.
2. Tanaka T. Gels. Scientific American 244 (1981) 124–138.
3. Okay O. Macroporous copolymer networks. Progress in Polymer Science 25 (2000) 711–872.
4. Liu Y, Valeda JL, Huglin MB. Thermoreversible swelling behavior of hydrogels based on N–isopropylacrylamide with sodium acrylate and sodium methacrylamide. Polymer 40 (1999) 4299–4306.
5. Durmaz S, Okay O. Ohase separation during the formation

of poly(acrylamide) hydrogels. Polymer 41 (2000) 5729–5735.
6. Karadağ E, Saraydın D. Swelling of Superabsorbent Acrylamide/Sodium Acrylate Hydrogels Prepared Using Multifunctional Crosslinkers. Turkish Journal of Chemistry 26 (2002), 863 – 875.
7. Kawasaki H, Sasaki S, Maeda H. Synthesis of chitosan–based hydrogels as a novel drug release device for wound healing. Journal of Physical Chemistry B 101 (1997) 5089-5093.
8. Tamahkar E., Özkahraman B. Synthesis of chitosan–based hydrogels as a novel drug release device for wound healing. Hittite Journal of Science and Engineering 4 (2017) 137–144.
9. Tamahkar E., Özkahraman B. Potential evaluation of PVA based hydrogel for biomedical application. Hittite Journal of Science and Engineering 2 (2015) 165–171.
10. Mah E, Ghosh R.Thermo–responsive hydrogels for stimuli–responsive membranes. Processes 1 (2013) 238-262.
11. Yoshida R, Okano T. Stimuli–responsive hydrogels and their application to functional materials, in: Ottenbrite RM, Park K, Okano T (Eds.). Biomedical applications of hydrogels handbook. Springer, New York, pp 19-43, 2010.
12. Zhao Y, Kang J, Tan T. Salt–, pH– and temperature–responsive semi–interpenetrating polymer network hydrogel based on poly(aspartic acid) and poly(acrylic acid). Polymer 47 (2006) 7702-7710.
13. Reddy TT, Takahara A. Simultaneous and sequential micro–porous semi–interpenetrating polymer network hydrogel films for drug delivery and wound dressing applications. Polymer 50 (2009) 3537-3546.
14. Mumaddei FA, Haider S, Aijaz O, Haider A. Preparation of the chitosan/polyacrylonitrile semi–IPN hydrogel via glutaraldehyde vapors for the removal of Rhodamine B dye. Polymer Bulletin 74 (2017) 1535–1551.
15. Dash M, Ferri M, Chiellini F. Synthesis and characterization of semi–interpenetrating polymer network hydrogel based on chitosan and poly(methacryloylglycylglycine). Materials Chemistry and Physics 135 (2012) 1070-1076.
16. Zoratto N, Matricardi P. Semi IPN and IPN -based hydrogels, in: Oliveira JM, Pina S, Reis RL, Roman JS (Eds.). Advances in Experimental Medicine and Biology, Osteochondral Tissue Engineering, Challenges, Current Strategies and Technological Advances, Springer International Publishing Cham, Switzerland pp. 160–170, 2018.
17. Li G, Guo L, Chang X, Yang M. Thermo–sensitive chitosan based semi–IPN hydrogels for high loading and sustained release of anionic drugs. International Journal of Biological Macromolecules 50 (2012) 899–904.
18. Povea MB, Monal WA, Rodriguez JVC, Pat AM, Rivero NB, Covas CP Interpenetrated Chitosan–Poly(Acrylic Acid–Co–Acrylamide) Hydrogels. Synthesis, Characterization and Sustained Protein Release Studies. Materials Sciences and Applications 2 (2011) 509–520.
19. Wei QB, Luo YL, Fu F, Zhang YQ, Ma RX. Synthesis, Characterization, and Swelling Kinetics of pH–responsive and Temperature–Responsive Carboxymethyl Chitosan/Polyacrylamide Hydrogels. Journal of Applied Polymer Science 129 (2012) 806–814.
20. Farahani BV, Ghasemzaheh H, Shiravan A. Intelligent semi IPN chitosan–PEG–PAAm hydrogel for closed–loop insülin delivery and kinetic modeling .RSC Advances 6 (2016) 26590–26598.
21. Liu Z, Zhou S. Removal of humic acid from aqueous solution using polyacrylamide/chitosan semi–IPN hydrogel. Water Science and Technology 1 (2018)16–26.
22. Davidson DW, Verma MS, Gu FX. Controlled root targeted delivery of fertilizer using an ionically crosslinked carboxymethyl cellulose hydrogel matrix. SpringerPlus 2 (2013) 318–326.
23. Mahdavinia GR, Mousavi SB, Karimi F, Marandi GB, Garabaghi H, Shahabvand S. Synthesis of porous poly(acrylamide) hydrogels using calcium carbonate and its application for slow release of potassium nitrate. eXPRESS Polymer Letters 3 (2009) 279–285
24. Louzri F, Bennour S. Swelling behavior of poly(N–hydroxymethyl–acrylamide–co–acrylic acid) hydrogels and release of potassium nitrate as fertilizer. Journal of Polymer Engineering 38 (2017) 437–447.
25. Jamnongkan T, Kaewpirom S. Potassium release kinetics and water retentation of controlled–release fertilizers based on chitosan hydrogels. Journal of Polymers and the Environment 18 (2010) 413–421.
26. Pulat M, Sağlam NY. The preparation of controlled release fertilizer based on gelatin hydrogel Including Ammonium nitrate and investigation of its influence on vegetable growth. The Eurasia Proceeding of Science Engineering&Mathematics, 2 (2018) 17–24.
27. Pulat M, Uğurlu N. Preparation and characterization of biodegradable gelatin–PAAm based IPN hydrogels for controlled release of maleic acid to improve the solubility of phosphate fertilizers. Soft Materials 14 (2016) 217–227.
28. Scott LC , Washington State University. The myth of polyacrylamide hydrogels, https://s3.wp.wsu.edu/uploads/sites/403/2015/03/hydrogels.pdf.

Hittite Journal of Science and Engineering, 2019, 6 (2) 147-152
ISSN NUMBER: 2148-4171
DOI: 10.17350/HJSE19030000140

Review: An Optical Surface Probe by Reflectance Anisotropy Spectroscopy

Orhan Zeybek
Balıkesir University, Faculty of Science and Arts, Department of Physics,, Balıkesir, TURKEY

ABSTRACT

Reflectance anisotropy spectroscopy (RAS) is an optical technique to produce surface and interface information. RAS measures the difference in reflectance of light linearly polarised along two orthogonal axes in the surface at near normal incidence as a function of photon energy. The quantity obtained by RAS is the so-called reflectance anisotropy. Since only the surface is anisotropic, the measured reflectance anisotropy is connected only with the atomic composition of the surface, not of the bulk. This review presents theoretical as well as experimental procedure to explain RAS technique.

Article History:
Received: 2017/10/23
Accepted: 2019/06/27
Online: 2019/06/30

Correspondence to: Orhan Zeybek, Balıkesir University, Facult of Sciences and Arts, Department of Physics, Balıkesir, TURKEY
Tel: +90 (266) 612 1278/1305
Fax: +90 (266) 612 1215
E-Mail: ozeybek@balikesir.edu.tr

Keywords:
Reflectance anisotropy spectroscopy; Optical technique; Anisotropy; Polarized light.

INTRODUCTION

Optical techniques have played an important role in solid state physics for a considerable time. Ellipsometry has a history of over 100 years [1-3]. Ellipsometry has a surprisingly broad range of application in different scientific areas are ranging from electrochemistry to medicine [4]. Ellipsometry is the general name for the family of optical techniques, based on exploiting the polarisation transformation that occurs as a beam of polarized light is reflected from or transmitted through an optical component. The application of optical techniques to surface science is complicated in terms of optical response and surface sensitivity.

An impressive way to obtain surface sensitivity is offered by reflectance anisotropy spectroscopy (RAS), a young member of the old family of Ellipsometry techniques. The standard RAS was introduced in 1985 by Aspnes [5-6]. One of the surface science techniques is the RAS, a rapidly developing new technique which has already made itself a name in controlling semiconductor growth at monolayer level both under ultra-high vacuum (UHV) and non-UHV conditions [7-8].

The quantity obtained by RAS is the so-called reflectance anisotropy (RA). RA can be described as in Eq 1:

$$\Delta r / r_i = 2\left(r_x - r_y\right) / \left(r_x + r_y\right) \quad (1)$$

where r_i is the Fresnel complex-amplitude reflection coefficient for light polarised along the i^{th} axes. RAS takes advantage of the fact that most semiconductors for instance GaAs, Si and Ge possess an isotropic bulk (cube lattice) and anisotropic (reconstructed) surface [9]. Regarding the Fresnel equation, polarisation dependent differences in the reflection of a light beam are inevitable because of anisotropy somewhere in the sample [10]. Since only the surface is anisotropic, the measured reflectance anisotropy is connected only with the atomic composition of the surface, not of the bulk. For this class of semiconductors RAS can gain surface sensitivity.

When measuring the RA, the main problem is the small difference between r_x and r_y (~1% for semiconductors). This is due to the fact that exclusively the surface layers, which provide only an insignificant influence to the total reflectivity, cause the anisotropy in the reflection. Small drifts and fluctuations in the output of the lamp used would make measurements meaningless, unless a high averaging process is employed.

For (110) metal surfaces, RAS can be described as in Eq 2:

$$\frac{\Delta r}{r} = \frac{2\left(r_{[1\bar{1}0]} - r_{[001]}\right)}{r_{[1\bar{1}0]} + r_{[001]}} \quad (2)$$

In equation 1, the x = $[1\bar{1}0]$ and y = [0 0 1] directions are the two symmetry-directions of the surface.

EXPERIMENTAL APPARATUS IN RAS

The RAS equipment is shown schematically in figure 1. A 75 W Xenon (Xe) lamp is employed as a photon source. The energy range of typical RAS spectrometers is 1.5 - 5.0 eV, 830 - 225 nm, from visible to ultraviolet. Plane-polarized incident light is directed on the sample surface. The axes are focused on 45° to the plane of polarization of the incident beam. The RAS is planned to produce data on the complex Fresnel reflection amplitudes r_x and r_y related with two orthogonal symmetry surface directions $\vec{x}$ and $\vec{y}$ respectively. $\vec{x}$ and $\vec{y}$ are taken along [1$\bar{1}$0] and [001] directions respectively.

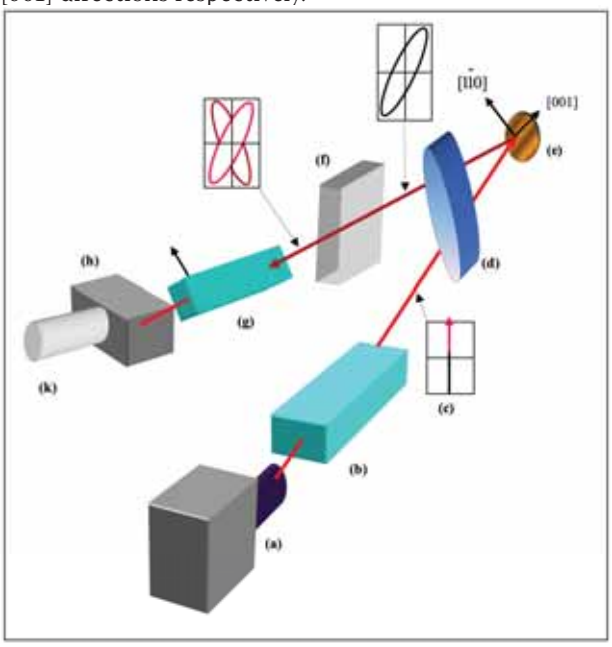

Figure 1. The RAS spectrometer: (a) Xe lamp (b) Polariser, (c) State of polarization, (d) Strain free RAS Window, (e) Sample in UHV environment, (f) photoelastic modulator, (g) Analyser, (h) Monochromator, (k) photomultiplier detector

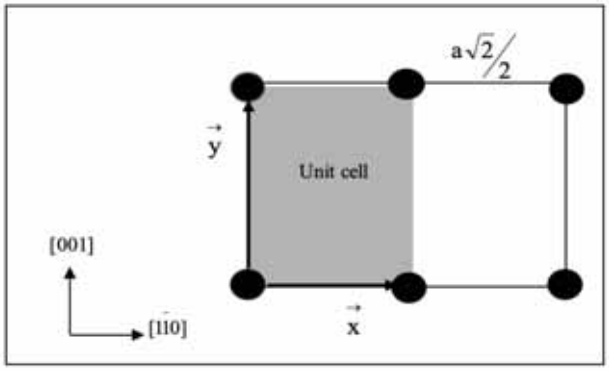

Figure 2. The geometry of the (110) surface in real space

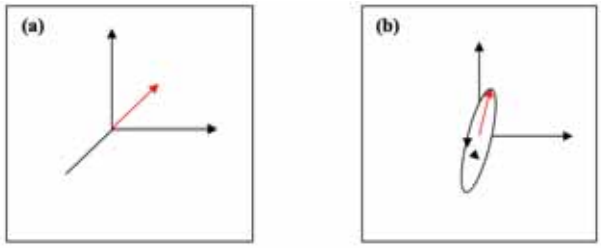

Figure 3. The polarisation of the (a) incident and the (b) emerging beam (for an arbitrary Δr/r) with respect to the principal axes of the sample.

In this review, for (110) metal surface can be taken into account. Figure 2 displays (110) metal surface and a unit cell of the real space lattice which is rectangular. The surface lattice vectors $\vec{x}$ and $\vec{y}$ are given by:

$$\vec{x} = \frac{a\sqrt{2}}{2}\hat{x} \quad (3)$$

$$\vec{y} = a\hat{y} \quad (4)$$

where $\hat{x}$ and $\hat{y}$ are unit vectors along $[1\bar{1}0]$ and [001] directions respectively.

Apparatus of RAS can be explained as follows:

Xenon-lamp:

The 75W high-pressure Xenon-lamp provides continuous and smooth spectrum with a sufficient output for light energies from 1.5 eV (830 nm) to 5.5 eV (225 nm). Due to the importance of a stable output, the lamp operates from a stabilised power supply. The light emerging from the lamp is linearly polarised before it strikes the sample at near normal incidence.

The polarisation-direction of the incident light beam is chosen so that we have equal amounts of polarised light along the 2 symmetry-directions as shown in Fig. 3(a). If the reflectivity for light polarised along these two directions were the same, the emerging light beam would obviously be linearly polarised as well. Since it is not, we get elliptically polarised light as shown in Fig. 3(b).

The tilt of the ellipse is related with the real part of the reflectance anisotropy i.e. Re (Δr/r), its breadth with the imaginary part of the reflectance anisotropy Im (Δr/r).

Photoelastic Modulator (PEM):

The subsequent arrangement of PEM and analyser generate an intensity-modulated signal from the light-beam, which contains the information about the reflectance anisotropy. The PEM modulates the phase of the component of the light beam linearly polarised parallel to its so-called modulation axis (frequency ω=50 kHz), while leaving the other component unaffected as presented in Fig. 4. As a

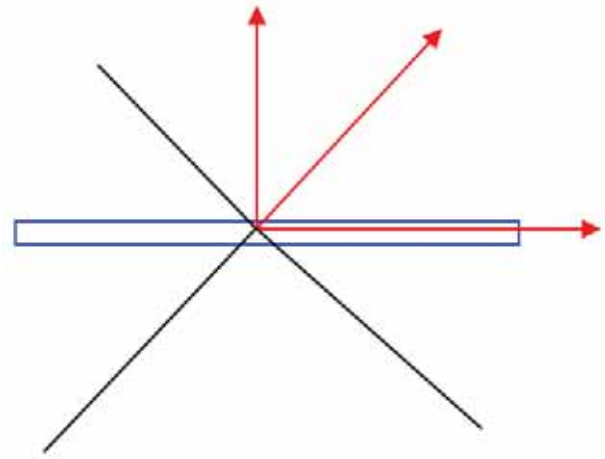

Figure 4. PEM modulates the phase of the component of the light beam

consequence of this modulation, the orientation and the form of the polarisation ellipse changes periodically [11-12]. The photomultiplier placed behind the analyser detects an intensity-modulated signal.

The Jones-analysis deals with the propagation of polarized light through polarization-modifying optical systems. Basically a light wave is represented by a vector and each optical component by a matrix. Modification of the state of the light wave by an optical component is obtained by multiplication of the vector of the wave with the matrix of the optical component.

It can be considered a monochromatic light beam with arbitrary polarization propagating along the z-axis of a coordination-fram (x,y,z). This can be described as [1]:

$$E(z,t) = E_x \cos(\omega t - 2\pi z / \lambda + \delta_x) e_x + E_y \cos(\omega t - 2\pi z / \lambda + \delta_y) e_y \quad (5)$$

With E_i representing the amplitude of the linear oscillations of the electric field components along the i-axes, and δ_i the respective phases of these oscilations. In considering the polarization of the wave and its modification by an optical device, we do not need the full expression given by the wave above. The Jones-vector of the light wave contains complete information about amplitudes and phases of the field components, and hence, about the polarization of the above. Temporal and spatial information of the wave are supressed. The Jones-vector for the wave above is [1]:

$$E = \begin{pmatrix} E_x \\ E_y \end{pmatrix} \text{ with } E_x = |E_x| exp(i\delta_x) \; ; \; E_y = |E_y| exp(i\delta_y) \quad (6)$$

The intensity of the light wave described by the Jones-vector is given by:

$$I = E^* E \text{ with } E^* = \begin{bmatrix} E_x^* & E_y^* \end{bmatrix} \quad (7)$$

The description of the polarization-modifying effect of an optical device on an incident beam is given by a (2 x 2) matrix. It cab be assumed E_i to be the Jones-vector of the incident light beam with reference to a coordination frame (x,y,z) and E_o the Jones-vector of the emerging light-beam with reference to a coordination frame (x',y',z'), with the directions of the z- and the z'-axes parallel to the wave vectors k and k' respectively (z=0 and z' =0 are arbitrary) [1]:

$$E_i = \begin{pmatrix} E_{ix} \\ E_{iy} \end{pmatrix} \quad E_o = \begin{pmatrix} E_{ox'} \\ E_{oy'} \end{pmatrix} \quad (8)$$

In the absence of non-linearity and other frequency-changing processes, the pair of oscillations $E_{0x`}$ and $E_{0y`}$ at the output of the optical system are related to the pair of oscillations E_{ix} and E_{iy} at the input of the optical system by the following equations [1]:

$$E_{ox`} = T_{11}E_{ix} + T_{12}E_{iy} \quad (9)$$

$$E_{oy`} = T_{21}E_{ix} + T_{22}E_{iy} \quad (10)$$

$$\begin{pmatrix} E_{ox'} \\ E_{oy'} \end{pmatrix} = \begin{pmatrix} E_{ix} \\ E_{iy} \end{pmatrix} \begin{pmatrix} T_{11} & T_{12} \\ T_{21} & T_{22} \end{pmatrix} = TE_I \quad (11)$$

This expresses the law of interaction between the incident wave and the optical component as a simple linear matrix-transformation of the Jones-vector representing the wave. T is called the Jones-matrix of the optical componet, it is in general complex. The Jones-matrix T depends on the chosen coordination frames (x,y,z) and (x`,y`,z`).

Polarizer (Rochon-prism):

The lamp emits unpolarized light. It cannot be described the unpolarized light with a Jones-vector. Thus we start the analysis with the linear polarised light beam emerging from the polarizer. The Jones vector is [1]:

$$E_{PO^{xy}} = \begin{pmatrix} 1/\sqrt{2} \\ A \\ 1/\sqrt{2} \end{pmatrix} \quad (12)$$

where A takes account of the intensity. The first letter in the subscript stands for the optical component, the second for input (I) or output (O). The superscript xy means with reference to this frame.

Window:

We consider an ideal window that has negligible influence on the light beam. In this case we do not have to consider the windows in Jones-analysis.

Sample:

The Jones matrix of the sample is [1]:

$$T_{S^{xy}} = \begin{pmatrix} r_x & 0 \\ r_y & r_i \end{pmatrix} \quad (13)$$

where r_i is the Fresnel complex-amplitude reflection coefficient for light polarised along the i-axis.

The PEM modulates the phase of one component of the light beam periodically. We claim this is the only influence on the light beam by an ideal PEM. The principal axes of the analyser coincide with the xy-frame. The properties of an ideal analyser are analogous to those of an ideal polarizer [1].

$$T_{A^{xy}} = \begin{pmatrix} 1 & 0 \\ 0 & 1 \end{pmatrix} \tag{14}$$

With the Jones matrix T_{RAS} of the whole arrangement it can be calculated the Jones' vector E_{AO} of the light beam arriving at the detector as:

$$E_{AO}{}^{xy} = T_{RAS}{}^{xy} E_{Pi}{}^{xy} \tag{15}$$

Regarding the matrix representing the analyser, we come to conclusion that:

$$T_{RAS}{}^{xy}{}_{(21)} = T_{RAS}{}^{xy}{}_{(22)} = 0 \tag{16}$$

Since the output of the analyser should be 0 for light polarised along the extinction axis we find that only: $T_{RAS}{}^{xy}{}_{(11)\,\text{is}}$ required to calculate the detected signal.

The reflectance anisotropy is described as [1]:

$$\Delta r / r = 2\left(r_x - r_y\right) / \left(r_x + r_y\right) \tag{17}$$

$$= 2\left(a^2 + b^2\right) - 2\left(c^2 + d^2\right) + \frac{4i(ad - bc)}{\left[\left(a^2 + b^2\right) + \left(c^2 + d^2\right) + 2(ac + bd)\right]} \tag{18}$$

and if we use for the denominator a~c; b~d (as the difference is at best about 1 percent)

$$\Delta r / r = 2\left(a^2 + b^2\right) - 2\left(c^2 + d^2\right) + 4i(ad - bc) / 4\left(a^2 + b^2\right) \tag{19}$$

which means:

$$Re\left(\Delta r / r\right) = \left[\left(a^2 + b^2\right) - \left(c^2 + d^2\right)\right] / 2\left(a^2 + b^2\right) \tag{20}$$

$$Im\left(\Delta r / r\right) = (ad - bc) / \left(a^2 + b^2\right) \tag{21}$$

Based on these two equations, Im (Δr/r) and Re (Δr/r) can be measured separately with the help of a Lock-In-amplifier.

THEORETICAL APPROACHES OF RAS

The propagation of the polarised light can be described through the optical apparatuses of the RAS by the Jones calculus [1]. The outcome of each optical factor upon the incident light is described by a (2 ´ 2) Jones matrix expressed in terms of fixed optical axes specific to the device of figure 1 and denoted $T^{xy}{}_i$ where i shows an optical device. The effect is termed by a differential retardation as below [1]:

$$e^{i\delta_W} = \left(e^{i\delta_{W\,f}}\right)\left(e^{i\delta_{Win}}\right) = \cos\delta_W + i\sin\delta_W \cong 1 + i\delta_W \tag{22}$$

The Jones matrixes and vectors have been summarized for each effective component in Table (1).

The pair of oscillations $E_{tx'}$ and $E_{ty'}$ at the output of the optical system are related to the pair of oscillations E_{ix} and E_{iy} at the input of the optical system in the absence of nonlinearity and other frequency-changing processes. Interaction between the incident wave and the optical component

Table 1. List of the Jones matrixes/vectors for each effective component

Device/Beam	*Jones Matrix*	*Jones Vector*	*Symbol/Remark*
Xe lamp	*N/A*	*N/A*	*Emits unpolarized light*
Incident light	*N/A*	$\begin{bmatrix} E_{ix} \\ E_{iy} \end{bmatrix}$	*E/Coordination frame (x,y)*
Transmission beam	*N/A*	$\begin{bmatrix} E_{tx'} \\ E_{ty'} \end{bmatrix}$	*E$_t$/Coordination frame (x',y')*
Linear polarised light	*N/A*	$K\begin{bmatrix} 1/\sqrt{2} \\ 1/\sqrt{2} \end{bmatrix}$	*$E_{Pt}{}^{xy}$/K as a constant of the detector*
Windows	$\begin{bmatrix} 1 & 0 \\ 0 & e^{i\delta_W} \end{bmatrix}$	*N/A*	*T_W/an ideal component*
Sample	$\begin{bmatrix} r_x & 0 \\ 0 & r_y \end{bmatrix}$	*N/A*	*$T_S{}^{xy}$/r_x and r_y are Fresnel complex amplitude reflection coefficient for light polarised along the $\vec{x}$ and $\vec{y}$ axes*
PEM	$\begin{bmatrix} 1 & 0 \\ 0 & e^{i\delta_M} \end{bmatrix}$	*N/A*	*$T_{PEM}{}^{tm}$/t and m standing for transmission and modulation axes respectively, δ is B sin (ω t), so B is the amplitude and ω is the frequency of the modulation*
Analyser	$\begin{bmatrix} 1 & 0 \\ 0 & 0 \end{bmatrix}$	*N/A*	*$T_A{}^{te}$/transmission axes of the analyser coincide with the xy-frame*
Polarizer	$\begin{bmatrix} 1 & 0 \\ 0 & 0 \end{bmatrix}$	*N/A*	*$T_P{}^{te}$/The properties of an ideal analyser are analogous to those of an ideal polarizer*

can be given by a simple linear matrix-transformation of the Jones-vector as [1]:

$$\begin{bmatrix} E_{tx'} \\ E_{ty'} \end{bmatrix} = \begin{bmatrix} S_{11} & S_{12} \\ S_{21} & S_{22} \end{bmatrix} \begin{bmatrix} E_{ix} \\ E_{iy} \end{bmatrix}, \quad E_{At}{}^{xy} = S_{RAS}{}^{xy} E_{Pi}{}^{xy} \tag{23}$$

where $S_{RAS}{}^{xy}$ is the Jones-matrix of the whole optical system. $S_{RAS}{}^{xy}$ can be written as:

$$S_{RAS}{}^{xy} = T_A{}^{te} R(\theta_M - \theta_A) T_M{}^{ts} R(-\theta_M) T_{Wf}{}^{xy} T_S{}^{xy} T_{Wi}{}^{xy} R(\theta_P) \tag{24}$$

The Jones vector $E_{At}{}^{xy}$ of the light arriving at the detector can be calculated by maintaining the Jones matrix $S_{RAS}{}^{xy}$ of the whole arrangement in figure 1 from the table 1. All matrices must operate in the correct order because they do not commute. Calculating $E_{At}{}^{xy}$ makes a final vector with one non-zero element, because the matrix representing the analyser $S_{RAS}{}^{xy}{}_{(21)} = S_{RAS}{}^{xy}{}_{(22)} = 0$. Since the output of the analyser should be zero for light polarised along the extinction axis, it was found that only $S_{RAS}{}^{xy}{}_{(11)}$ is required to calculate the detected signal. After matrix-multiplication the equation (23) gives:

$$E_{At}{}^{xy} = \left(1/2\sqrt{2}\right) K \begin{bmatrix} \left(r_x - r_y\right) + e^{i\delta}\left(r_x - r_y\right) \\ 0 \end{bmatrix} \tag{25}$$

Using Equation (22) and by substituting the azimuth angles in Equation (24), $E_{At}{}^{xy}$ is given by:

$$E_{At}{}^{xy} = \left(1/2\sqrt{2}\right)\left[\left(r_x - r_y\right) + \left(r_x - r_y\right)e^{i\delta_M} - i\delta_W r_y\left(1 - e^{i\delta_M}\right)\right] \tag{26}$$

The measured time-dependent light intensity, I, at the detector is given by:

$$I \infty E_{At} E_{At}{}^{*} \tag{27}$$

Following simple algebra, with $e^{i\delta} = \cos\delta + i\sin\delta$, $r_x = a - ib$ and $r_y = c - id$ where a, b, c and d are integer. Substituting these into Equation (27) results in an expression that can be separated into real and imaginary parts.

$$I \infty \left|E_{At}\right|^2 = \left\{\mathrm{Re}\left(E_{At}\right)\right\}^2 + \left\{\mathrm{Im}\left(E_{At}\right)\right\}^2 \tag{28}$$

After long calculations, Equation (27) becomes as below:

$$\begin{aligned} I \infty & 1/4\left[\left(a^2 + b^2\right) + \left(c^2 + d^2\right) + \left(c^2 + d^2\right)\delta_W{}^2\right] \\ & + 1/4\left[\left(a^2 + b^2\right) - \left(c^2 + d^2\right) - \left(c^2 + d^2\right)\delta_W{}^2\right]\cos\delta_M \\ & 1/2\left[\left(ab - cd\right) - \left(ac - bd\right)\delta_W\right]\sin\delta_M \end{aligned} \tag{28}$$

These expressions may be written in the form of:

$$I = I_{dc} + I_\omega \sin\delta_M + I_{2\omega}\cos\delta_M \tag{29}$$

The retardation δ_M induced by the PEM varies sinusoidally [12], following the expression

$$\delta_M = \alpha(\lambda)\sin(\omega t) \tag{30}$$

where a(l) and w are the amplitude of the modulation and the resonant angular frequency respectively. The frequency components of the signal are determined by the Fourier expansions of the terms $\cos\delta_M$ and $\sin\delta_M$ of Equation (29), introducing Bessel functions J of argument a (l) of order 'm' [11].

$$\begin{aligned} \cos\delta_M &= \cos\left(\alpha\sin(\omega t)\right) \\ &= J_0(\alpha) + 2\sum_{m=1}^{\infty} J_{2m}(\alpha)\cos(2m\omega t) \end{aligned} \tag{31}$$

$$\begin{aligned} \sin\delta_M &= \sin\left(\alpha\sin(\omega t)\right) \\ &= 2\sum_{m=0}^{\infty} J_{2m+1}(\alpha)\sin\left[(2m+1)\omega t\right] \end{aligned} \tag{32}$$

For the case of $J_0(\alpha) = 0$, I is achieved by adjusting the voltage applied to the PEM

$$I = I_{dc} + I_\omega 2J_1(\alpha)\sin\omega t + I_{2\omega} 2J_2(\alpha)\cos(2\omega t) + \cdots \tag{33}$$

By comparing equation (33) with equation (28) the intensity coefficients are defined. The normalized frequency terms then are established to be

$$I_{dc} \sim \left(\left|r_x\right|^2 + \left|r_y\right|^2\right)/2 \tag{34}$$

$$I_\omega / I_{dc} \sim \mathrm{Im}\left(\Delta r / r\right) - \delta_W \tag{35}$$

$$I_{2\omega} / I_{dc} \sim \mathrm{Re}\left(\Delta r / r\right) \tag{36}$$

Therefore, I_{dc} processes the reflectivity. The imaginary part of $\Delta r / r$ is dignified at frequency ω and the intensity is found to be sensitive to the first-order window, δ_W, strain.

CONCLUSION

The optical surface probe of RAS is a non-destructive technique for the study of metal-on-metal and semiconductor growth. RAS is an experimental optical method using visible light and is particularly attractive since it is not restricted to vacuum environments. RAS uses the basic components of ellipsometry. This review presents an overview of the RAS technique.

ACKNOWLEDGEMENTS

The author acknowledges Balikesir University for the support. The author also sincerely thanks to Dr. S.D. Barrett and A. M. Davarpanah at University of Liverpool Surface Science Research Centre, for their technical assistance.

REFERENCES

1. Azzam RMA, Bashara NM. Ellipsometry and Polarised light. North- Holland Physics publishing, Amsterdam, (1987).
2. McIntyre JDE, Aspnes DE. Differential reflection spectroscopy of very thin surface films. Surf Sci 24 (1971) 417.
3. Aspnes DE, Studna AA. High Precision Scanning Ellipsometer. Appl Opt 14 (1975) 220.
4. Shvets VA, Spesivtsev EV, Rykhlitskii SV, Mikhailov NN. Ellipsometry as a high-precision technique for subnanometer-resolved monitoring of thin-film structures. Nanotechnologies in Russia 4(3) (2009) 201.
5. Aspnes DE. Abovebandgap optical anisotropies in cubic semiconductors: A visible–near ultraviolet probe of surfaces. J Vac Sci Technol B 3 (1985) 1498.
6. Aspnes DE, Studna AA. Anisotropies in the Above Band-Gap Optical Spectra of Cubic Semiconductors. Phys Rev Lett 54 (1985) 1956.
7. Aspnes DE, Colas E, Studna AA, Bhat R, Koza MA, Keramidas VG. Kinetic Limits of Monolayer Growth on (001) GaAs by Organometallic Chemical-vapor Deposition. Phys Rev Lett 61 (1988) 2782.
8. Aspnes DE, Harbison JP, Studna AA, Florez LT. Application of reflectance difference spectroscopy to molecular-beam epitaxy growth of GaAs and AlAs. J Vac Sci Technol A 6 (1988) 1327.
9. Aspnes DE, Harbison JP, Studna AA, Florez LT. Optical reflectance and electron diffraction studies of molecular-beam-epitaxy growth transients on GaAs(001). Phys Rev Lett 59 (1987) 1687.
10. Bremer J, Hansen JK, Hunderi O. Electronic anisotropy in the $\Delta_5\Delta_1$ edge region of Cu(110). Appl Surf Sci 142 (1999). 286.
11. Wang CK, Chao YF. Measurement of optical activity using a photoelastic modulator system. Jpn J App Phys 38 (1999) 941.
12. Kemp JC, Henson GD, Steiner CT, Beardsley IS, Powell ER. The optical polarization of the Sun measured at a sensitivity of parts in ten million. Nature 326 (1987) 270.

Hittite Journal of Science and Engineering, 2019, 6 (2) 153-156
ISSN NUMBER: 2148-4171
DOI: 10.17350/HJSE19030000141

Reduction Behavior of Moxifloxacin Hydrocholaride and Its Analysis in Spiked Human Urine and Dosage Form by Voltammetry

Burcu Tepeli[1], Selehattin Yilmaz[1] Sultan Yagmur[2]
[1]University of Canakkale Onsekiz Mart, Faculty of Science and Arts, Department of Chemistry, Canakkale, Turkey
[2]University of Canakkale Onsekiz Mart, Lapseki Vocational School, Department of Chemistry and Chemical Processing Technology Programs, Program of Laboratory Technology, Lapseki, Canakkale, Turkey

ABSTRACT

A voltammetric method was developed to analyze moxifloxacin hydrochloride (MoxHCl) in pharmaceutical preparations and spiked human urine. The experimental measurements were completed using different buffer systems (pH 0.50- 12.05) on Glassy Carbon Electrode (GCE) with differential pulse voltammetry (DPV) and Cyclic Voltammetry (CV) methods. The effect of pH on the peak current and potential were determined. Britton-Robinson (BR) buffer (pH 7.00) was used for analysis. The peak was established to be diffusion-controlled based on the nature of electrode. Calibration plots were prepared for the concentration range from 3×10^{-4} M to 1.1×10^{-3} M with DPV. Limits of detection (LOD) and quantification (LOQ) were calculated as 5.1×10^{-5} M and 2.30×10^{-4} M, respectively. The validation of the applied methods was completed. Electroreduction mechanism was proposed.

Article History:
Received: 2018/07/27
Accepted: 2019/06/28
Online: 2019/06/30

Correspondence to: Selehattin Yilmaz, University of Canakkale Onsekiz Mart, Faculty of Science and Arts, Department of Chemistry, Canakkale, TURKEY
E-Mail: seletyilmaz@hotmail.com
Phone: +90(286) 218 00 18

Keywords:
Moxifloxacin hydrochloride; Reduction; Pharmaceutical Preparations; Human urine; Voltammetry.

INTRODUCTION

Moxifloxacin HCl (Fig. 1) is a kind of broad-spectrum antimicrobial fluoroquinolone [1]. It is used in the treatment of bacterial sinusitis [2,3].

MoxHCl was analyzed with high-performance liquid chromatography. [4-6] In the literature, several electroanalytical techniques based on oxidative behavior of MoxHCl are also reported. Studies with modified electrodes [1,7], glassy carbon electrode [8,9] and carbon paste electrode[10] were reported. There are studies in the literature about the reduction behaviour of moxifloxacin and the determination by electrochemical reduction method [11-13]. In this study, electroreduction of MoxHCl was investigated with CV and DPV on a GCE, also the effects of supporting electrolyte, pH and scan rate on the electroreduction of this substance were investigated. It was shown that the method could be applied in pharmaceutical preparations and human urine.

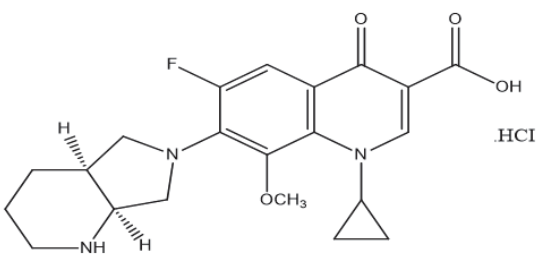

Figure 1. Chemical formula of MoxifloxacinHCl.

EXPERIMENTAL

Apparatus

In this work, current and potential values were measured with 757-VA Trace-Analyzer (Metrohm).Three electrodes were used; a working electrode (GCE), counter (platinum-wire) and reference electrode (silver/silver chloride in 3 M potassium chloride). The working electrode was cleaned using alumina and rinsed with ethanol and deionized water. Voltammograms were taken after argon gas was passed through a buffer and the analysis solution. A 744 pH-meter (Metrohm, Herisau, Switzerland) was used for pH measurements.

Reagents and Materials

MoxHCl was obtained from Bayer, Istanbul, Turkey. Stock solutions of 1.00×10^{-1} M of MoxHCl were created with deionized water. Diluted solutions were prepared from this stock solution. 0.5 M H_2SO_4, 0.067 M phosphate, 0.2 M acetate and 0.04 M BR buffers were used as supporting electrolytes. Deionized-water was obtained from Sartorius Arium model deionized water Systems. Chemicals used were high purity. The calibration curve was formed from 3.0×10^{-4} M to 1.1×10^{-3} M using the DPV technique.

Analysis of Spiked Pharmaceutical Samples

Ten Avelox tablets were prepared containing $1x10^{-1}$ M MoxHCl in deionized water. This solution was centrifuged for about 15 minutes at 5000 rpm. After that, the diluted supernatant was taken and measured. The content of the active drug was determined with the calibration curve.

Analysis in Urine Spiked Samples

A sample taken freshly from a villager was adjusted 2:8 using deionized-water. Then 8.0 mL of 0.065 M phosphate buffer (pH 6.50) was inserted into the cell and measured for blank. After that, 500 µL of urine sample was inserted and urine and blank were measured. To get a 4×10^{-4} M, 40µL (2 mL Urine + 7 mL deionized Water + 1.0 mL of 1.0 M MoxHCl) was placed into the cell and measured. 30 µL of 1.0×10^{-1} M MoxHCl was used for measurement. The calibration curve was obtained from these measurements.

RESULTS AND DISCUSSION

Electrochemical Reduction Properties of MoxHCl

The best analytical signal was obtained at pH 6.50 in 0.065 M phosphate solution and this was selected for drug analysis (Fig. 2).

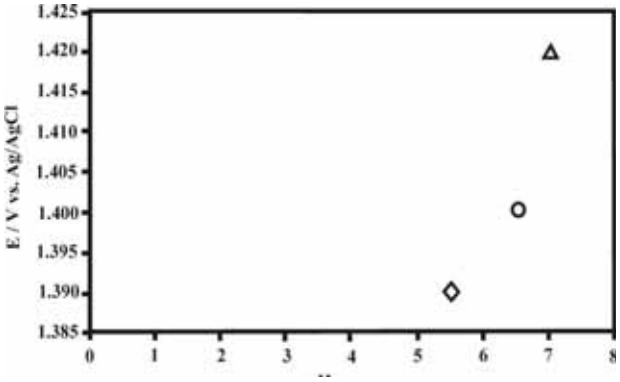

Figure 2. Change of pH at the DPV peak potential in 5×10^{-5} M MoxHCl (◊) acetate, (0.02 M), (o) phosphate (0.067 M) and (Δ) BR (0.04 M) buffers.

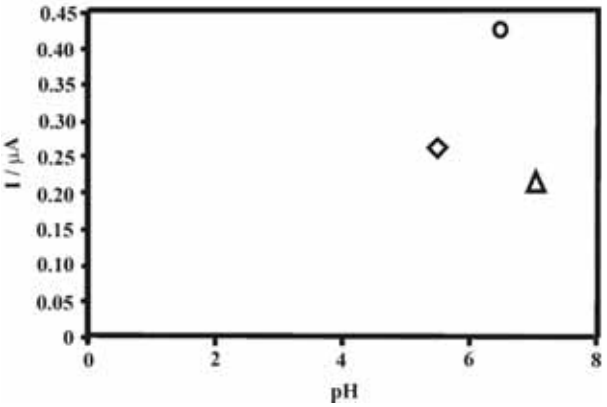

Figure 3. Change of the DPV peak current in 5×10^{-5}M MoxHCl in (◊) acetate, (0.02 M), (o) phosphate (0.067 M) and (Δ) BR (0.04 M) buffers.

The increase in pH linearly shifted the peak potential to more negative values. This indicates participation of proton transfer at the electrode reaction (Fig. 3).

The effects of scan rate from 50 to1000 mVs^{-1} on the potential and current of peak MoxHCl were investigated. The CV of MoxHCl at pH 6.50 in 0.065 M phosphate buffer is given in Fig. 4.

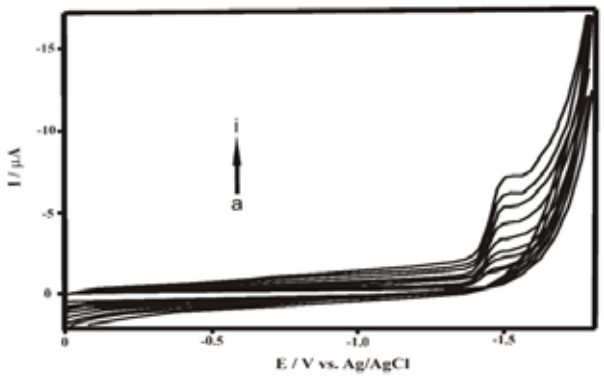

Figure 4. Cyclic voltammograms of 1×10^{-4} M MoxHCl in 0.067 M phosphate buffer (pH 6.50) on the GCE. Scan rate, ν, mVs^{-1}, a) blank, b) 50, c) 100, d) 150, e) 250, f) 400, g) 600, h) 750, and ı) 1000.

The R value of peak current and square root of the scan rate is 0.999 ($I_p/\mu A=0.0471\nu^{1/2}$-0.2105). Slope (0.06797) of the curve of log I versus log ν showed that the reduction mechanism is diffusion-controlled [14-16].

The cyclic voltammogram of MoxHCl exhibited one cathodic peak and potential value changed to more negative values with the rising scan rate, indicating that the reaction is irreversible [16].

Validation of the Applied Voltammetric Technique

The concentration was established in the range from 3×10^{-4} M to 1.1×10^{-3} M with DPV (Fig. 5).The equation of

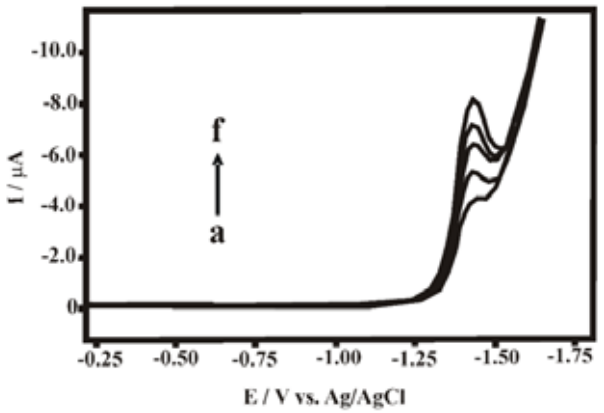

Figure 5. Calibration voltammograms for different concentrations of MoxHCl in 0.067 M phosphate buffer (pH 6.50) on the GCE with DPV a) blank b) 3.0×10^{-4} c) 5.0×10^{-4} d) 7.0×10^{-4} e) 9.0×10^{-4} and f) 1.10×10^{-3} M MoxHCl.

the calibration curve was $I_p/\mu A=2830\ C(M)+0.446$ with, R (Correlation Coefficient, 0.99); (Repeated experiment: 4). The validation parameters of applied method are given in Table 1 and Table 2.

Table 1. Parameters of analytical MoxHCl determined in phosphate buffer (pH 6.50) using the DPV technique.

Parameters	*Results*
Measured potential,V	*-1.4*
Linear concentration range, M	*3×10^{-4}- 1.1×10^{-3}*
Slope, µAM	*2830*
SD of slope	*4.15*
Intercept, nA	*0.446*
SD of intercept	*5.87*
Correlation coefficient, R	*0.99*
LOD, M	*5.51×10^{-5}*
LOQ, M	*2.30×10^{-4}*
Reproducibility of peak current, RSD %	*1.078 for 9×10^{-4} M*
Reproducibility of peak potential, RSD %	*0.505 for 9×10^{-4} M*

Analysis of MoxHCl in Pharmaceutical Preparations with Voltammetry Techniques

MoxHCl was determined in Avelox form and results are given in Table 2.

Analysis of Spiked Human Urine

The analysis of MoxHCl in a urine sample was completed

Table 2. Results for assay of MoxHCl in pharmaceutical preparation.

Parameters	*Results*
MoxHCl, mg	*436.5*
Amount found, mg	*442.05*
Relative Standard deviation, RSD%	*2.38*
Bias %	*1.27*
MoxHCl spiked, mg	*1.3*
Found, mg	*1.24*
Average recovery, %	*95*
Relative standard deviation of recovery, RSD %	*2.46*
Bias %	*5*

(Fig. 6). The values of these analyses are given in Table 3.

Table 3. Quantitative determination of MoxHCl in spiked human urine samples with recovery results.

Parameters	*Results*
MoxHCl, M	*4×10^{-4}*
MoxHCl found, M	*3.91×10^{-4}*
Number of measurements, N	*10*
Average recovery, %	*97.75*
RSD %	*0.90*
Bias %	*2.25*

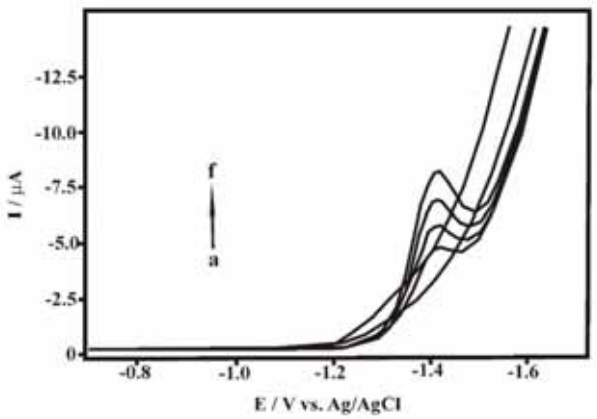

Figure 6. DP voltammograms of MoxHCl in spiked human urine a) Blank, 0.067 M phosphate buffer (pH6.50) b) a + 600 µL urine (1:9); c) 4.0×10^{-4} MoxHCl with urine d) 2.0×10^{-4} e) 4.0×10^{-4} and f) 6.0×10^{-4}M MoxHCl.

Electroreduction Mechanism of MoxHCl

Electroreduction mechanisms of MoxHCl were proposed as below:

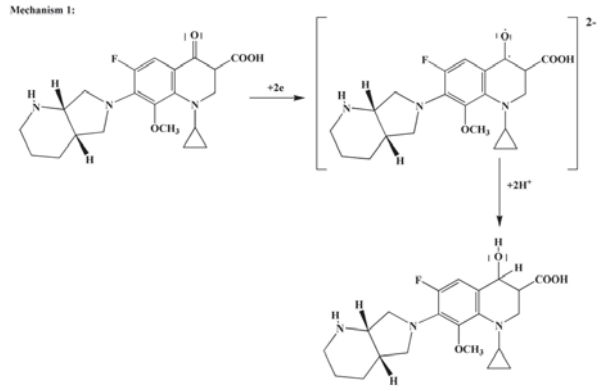

Figure 7. Proposed electroreduction mechanism of MoxHCl.

CONCLUSION

In summary, MoxHCl was determined in phosphate buffer (pH 6.50) in pharmaceutical preparations using DPV. The advantage of the voltammetric technique is that it can be applied fast, at low cost and directly to the analysis form of the drug without interference.

ACKNOWLEDGMENT

This study was part of a Master Thesis (Burcu TEPELİ) accepted for Applied Sciences, University of Çanakkale Onsekiz Mart. The authors thank Bayer (Istanbul, Turkey) for MoxHCl and its Avelox formulation.

References

1. Zhou Q, Long L, Liu L, Zhai H, Zhu M. Electrochemical determination of moxifloxacin hydrochloride based on molecularly imprinted polymer modified carbon paste electrode. Int. J. Electrochem. Sci. 10 (2015) 5069-5076.
2. Khan W, Sullivan KL, McCann JW, Gonsalves CF, Sato T. Moxifloxacin Prophylaxis for Chemoembolization or Embolization in Patients With Previous Biliary Interventions: A Pilot Study, AJR. Am J Roentgenol 197 (2011) 343-345.
3. Gyssens I.C, Dryden M, Kujath P, Nathwani D, Schaper N, Hampel B. J. Antimicrob Chemother 66 (2011) 2632-2642.
4. Xu YH, Li D, Liu XY, Li YZ, Lu J. Journal of Chromatography B 878 (2010) 3437-3341.
5. Hemanth A, Kumar K, Sudha V, Srinivasan R, Ramachandran G. Simple and rapid liquid chromatography method for determination of moxifloxacin in saliva. Journal of Chromatography B 879 (2011) 3663-3667.
6. Ulu S.T. Journal of Pharm. And Biomed. A. 43 (2007) 320-323.
7. Upadhyay SS, Kalambate PK, Srivastava AK. Enantioselective analysis of Moxifloxacin hydrochloride enantiomers with graphene-β-Cyclodextrin-nanocomposite modified carbon paste electrode using adsorptive stripping differential pulse voltammetry. Electrochimica Act. 248 (2017) 258-269.
8. Radi AE,Wahdan T, Anwar Z, Mostafa H. Electrochemical and spectroscopic studies on the Interaction of Gatifloxacin, Moxifloxacin and sparfloxacin with DNA and their analytical applications. Electroanalysis 22 (2010) 2665-2671.
9. Erk N. Voltammetric Behaviour And Determination Of Moxifloxacin In Pharmaceutical Products And Human Plasma. Anal Bioanal.Chem. 378 (2004) 1351-1356.
10. Long N, Zhu M, Yan Z. Anodic Adsorptive Voltammetric Determination of Moxifloxacin Hydrochloride. Physical Testing and Chemical Analysis (Part B: Chemical Analysis. R914;O657.14, 2012.
11. Trindade MAG, Da Silva GM, Ferreira VS. Interaction study of moxifloxacin with Cu(II) ion using square-wave voltammetry and its application in the determination in tablets. Microchemical Journal 81(2005) 209-216.
12. Abdel Ghani NT, El-Ries MA, El-Shall MA. Validated polarographic methods for the determination of certain antibacterial drugs. Analytical Sciences, 23 (2007) 1053-1058.
13. İnam R, Mercan H , Yılmaz E, Uslu B. Differential Pulse Polarographic Determination of Co(II) Using Moxifloxacine. Analytical Letters 40 (2007) 529-546.
14. Skrzypek S, Ciesielski W, Sokolowski A,Yılmaz S, Kazmiercak D. Square wave adsorptive stripping voltammetric determination of famotidine in urine. Talanta 66 (2005) 1146-1151.
15. Çıtak M,Yılmaz S, Dilgin Y,Türker G,Yağmur S, Erdugan H. Osteryoung Square Wave Voltammetric Determination of Phenazopyridine Hydrochloride in Human Urine and Tablet Dosage Forms Based on Electrochemical Reduction at Carbon Paste Electrode. Curr. Pharm. Anal. 3 (2007)141-145.
16. Yağmur S,Yılmaz S, Sadıkoğlu M, Saglıkoğlu G, Yıldız M, Yengin Ç, Kılınç E. Electrooxidation of Phenazopyridine Hydrochloride and its Voltammetric and HPLC Determination in Human Urine and Tablet Dosage Form. Int. J. Electrochem. Sci. 8 (2013) 6818-6828.